SURFACE POTENTIAL SENSING ATOMIC FORCE MICROSCOPY TO PROBE THE ROLE OF OXYGEN EVOLUTION CATALYSTS WHEN PAIRED WITH METAL-OXIDE SEMICONDUCTORS

by

MICHAEL R. NELLIST

A DISSERTATION

Presented to the Department of Chemistry and Biochemistry
and the Graduate School of the University of Oregon
in partial fulfillment of the requirements
for the degree of
Doctor of Philosophy

September 2018

DISSERTATION APPROVAL PAGE

Student: Michael R. Nellist

Title: Surface Potential Sensing Atomic Force Microscopy to Probe the Role of Oxygen Evolution Catalysts when Paired with Metal-Oxide Semiconductors

This dissertation has been accepted and approved in partial fulfillment of the requirements for the Doctor of Philosophy degree in the Department of Chemistry and Biochemistry by:

Dr. Mark C. Lonergan	Chairperson
Dr. Shannon W. Boettcher	Advisor
Dr. George V. Nazin	Core Member
Dr. Benjamín J. Alemań	Institutional Representative

and

Janet Woodruff-Borden	Vice Provost and Dean of the Graduate School

Original approval signatures are on file with the University of Oregon Graduate School.

Degree awarded September 2018

DISSERTATION ABSTRACT

Michael R. Nellist

Doctor of Philosophy

Department of Chemistry and Biochemistry

September 2018

Title: Surface Potential Sensing Atomic Force Microscopy to Probe the Role of Oxygen Evolution Catalysts when Paired with Metal-Oxide Semiconductors

While prices of solar energy are becoming cost competitive with traditional fossil fuel resources, large scale deployment of solar energy has been limited by the inability to store excess electrical energy efficiently. One promising route towards both the capture and storage of solar energy is through photoelectrochemical water splitting, a process by which a semiconducting material can collect energy from the sun and use it to directly split water (H_2O) into hydrogen fuel and oxygen. Unfortunately, photoelectrochemical water splitting devices are limited by the low efficiencies and high overpotentials of the oxygen evolution reaction (OER). To improve kinetics of OER, different electrocatalyst are often coated on the semiconductor. However, the role of the catalyst and the mechanism of charge transfer at the semiconductor|catalyst interface is not clear. It is important to understand this interface if we are to rationally design high performance water splitting cells.

The research presented in this dissertation takes on two aims: 1) obtaining a fundamental knowledge of the charge transfer processes that take place at the semiconductor catalyst interface of photoanodes and 2) developing new experimental approaches that can be applied towards achieving the first aim. Specifically, this dissertation begins with a prospectus that outlines the state of the field, and the what was known about the semiconductor|electrocatalyst interface at the outset of the presented work (Chapter II). Next, the testing and application of new nanoelectrode AFM probes to study an array of electrochemical phenomena will be discussed (Chapter III). These probes will then be applied towards the study of hematite (Fe_2O_3) semiconductors coated with cobalt phosphate (oxy)hydroxide (CoPi) electrocatalyst (Chapter IV) and bismuth

vanadate ($BiVO_4$) semiconductors coated with CoPi electrocatalyst (Chapter 5).

This dissertation includes previously published and unpublished co-authored material.

CURRICULUM VITAE

NAME OF AUTHOR: Michael R. Nellist

GRADUATE AND UNDERGRADUATE SCHOOLS ATTENDED:

University of Oregon, Eugene
State University of New York College at Geneseo, Geneseo

DEGREES AWARDED:

Doctor of Philosophy, Chemistry, 2018, University of Oregon
Master of Science, Chemistry, 2015, University of Oregon
Bachelor of Science, Chemistry, State University of New York College at Geneseo

AREAS OF SPECIAL INTEREST:

Solar Energy Materials

PROFESSIONAL EXPERIENCE:

Graduate Employee – Advanced General Chemistry, University of Oregon, Fall 2014-Spring 2015

Graduate Employee – Atomic Force Microscopy Instrument Manager, Fall 2015 Fall 2017

GRANTS, AWARDS, AND HONORS:

Sir Fraser Stoddart Scholarship, Renewable Energy Scholarship Foundation, 2018

Phi Beta Kappa, SUNY Geneseo, 2014

Presidential Scholar, SUNY Geneseo, 2013

Bruce Ristow Fellowship, SUNY Geneseo, 2012

Gamma Sigma Epsilon, SUNY Geneseo, 2012

Eagle Scout, Boy Scouts of America, 2006

PUBLICATIONS:

Enman, L.; Stevens, M. B.; Dahan, M. H.; Nellist, M. R.; Troker, M. C.; Boettcher, S. W. Operando X-Ray Absorption Spectroscopy Shows Fe Oxidation is Concurrent with Oxygen Evolution in Cobalt-Iron (Oxy)hydroxide electrocatalysts. *Angew. Chem.* Submitted.

Laskowski, F. A. L.; Qiu, J.; Nellist, M. R.; Oener, S. Z.; Gordon, A. M.; Boettcher, S., Transient Photocurrents on Catalyst-Modified n-Si Photoelectrodes: Insight from Dual-Working Electrode Photoelectrochemistry. *Sustainable Energy & Fuels* **2018**, DOI: 10.1039/C8SE00187A.

Dette, C.; Hurst, M.; Deng, J.; Nellist, M.; Boettcher, S. Structural Evolution of Metal (Oxy)hydroxide Nanosheets During the Oxygen Evolution Reaction. *ACS Appl. Mater. Interfaces*. **2018**, DOI: 10.1021/acsami.8b02796

Qiu, J.; Hajibabaei, H.; Nellist, M. R.; Laskowski, F. A. L.; Oener, S. Z.; Hamann, T. W.; Boettcher, S. W. Catalyst Deposition on Photoanodes: The Roles of Intrinsic Catalytic Activity, Catalyst Electrical Conductivity, and Semiconductor Morphology. *ACS Energy Lett.* **2018**, *3*, 961-969.

Nellist, M. R.; Laskowski, F. A. L.; Qiu, J.; Hajibabaei, H.; Sivula, K.; Hamann, T. W.; Boettcher, S. W. Potential-Sensing Electrochemical Atomic Force Microscopy for In Operando Analysis of Water-splitting Catalysis and Interfaces. *Nat. Energy*, **2018**, *3*, 46-52.

Deng, J.; Nellist, M.R.; Stevens, M.; Dette, C.; Wang, Y.; Boettcher, S. Morphology Dynamics of Single-Layered $Ni(OH)_2$/NiOOH Nanosheets and Subsequent Fe Incorporation Studied by In-situ Electrochemical Atomic Force Microscopy. *Nano Lett*. **2017**, *17*, 6922-6926.

Woods, K. N.; Waddington, E. C.; Crump, C. A.; Bryan, E. A.; Gleckler, T. S.; Nellist, M. R.; Duell, B. A.; Nguyen, D. P.; Boettcher, S. W.; Page, C. J. Tunable High-κ $Zr_xAl_{1-x}O_y$ Thin Film Dielectrics from Aqueous Precursor Solutions. *RSC Adv.* **2017**, *7*, 39147–39152.

Qiu, J.; Hajibabaei, H.; Nellist, M. R.; Laskowski, F. A. L.; Hamann, T. W.; Boettcher, S. W. Direct In Situ Measurement of Charge Transfer Processes During Photoelectrochemical Water Oxidation on Catalyzed Hematite. *ACS Cent. Sci.* **2017**, *3*, 1015–1025.

Mills, T. J.; Laskowski, F. A. L.; Dette, C.; Nellist, M. R.; Lin, F.; Boettcher, S. W. The Role of Surface States in Electrocatalyst-Modified Semiconductor Photoelectrodes: Theory and Simulations. *arXiv:1707.03112,* **2017**.

Laskowski, F. A. L.; Nellist, M. R.; Venkatkarthick, R.; Boettcher, S. W. Junction Behavior of N-Si Photoanodes Protected by Thin Ni Elucidated from Dual Working Electrode Photoelectrochemistry. *Energy Environ. Sci.* **2017**, *10*, 570–579.

Nellist, M. R.; Chen, Y.; Mark, A.; Gödrich, S.; Stelling, C.; Jiang, J.; Poddar, R.; Li, C.; Kumar, R.; Papastavrou, G.; Retsch, M.; Brunschwig, B. S.; Huang, Z.; Xiang, C.; Boettcher, S. W. Atomic Force Microscopy with Nanoelectrode Tips for High Resolution

Electrochemical, Nanoadhesion and Nanoelectrical Imaging. *Nanotechnology* **2017**, *28*, 95711.

Huang, Z.; De Wolf, P.; Poddar, R.; Li, C.; Mark, A.; Nellist, M. R.; Chen, Y.; Jiang, J.; Papastavrou, G.; Boettcher, S. W.; Xiang, C.; Brunschwig, B. S. PeakForce Scanning Electrochemical Microscopy with Nanoelectrode Probes. *Microscopy Today* **2016**, *24*, 18-25.

Nellist, M. R.; Laskowski, F. A. L.; Lin, F.; Mills, T. J.; Boettcher, S. W. Semiconductor - Electrocatalyst Interfaces: Theory, Experiment, and Applications in Photoelectrochemical Water Splitting. *Acc. Chem. Res.* **2016**, *49, 733-740.*

Hite, O. K.; Nellist, M.; Ditto, J.; Falmbigl, M.; Johnson, D. C. Transport Properties of VSe_2 Monolayers Separated by Bilayers of BiSe. *J. Mater. Res.* **2015**, *31*, 886-892.

Geiger, D. K.; Nellist, M. R. 5-Chloro-2-(Thiophen-2-Yl)-1-(Thiophen-2-Ylmethyl)-1H-benzimidazole–6-Chloro-2-(Thiophen-2-Yl)-1-(Thiophen-2-Ylmethyl)-1H-Benzimidazole (0.94/0.06). *Acta Crystallogr. Sect. E.* **2013**, *69*, o1539–o1540.

Geiger, D. K.; Nellist, M. R. 6-Chloro-2-(Thiophen-2-Yl)-1-(Thiophen-2-Ylmethyl)-1 H -Benzimidazole. *Acta Crystallogr. Sect. E.* **2013**, *69*, o807.

ACKNOWLEDGMENTS

I would like to start by recognizing the funding agencies that have supported my work, primarily the Department of Energy Basic Energy Sciences (DE-SC0014279), the NSF Major Research Instrumentation Program (DMR-1532225) and the University of Oregon. I would also like to thank everyone who has supported, encourage and mentored me over the years. While it is not possible to comprehensively list everyone that has impacted my journey, I would like to specifically mention a few here.

First, I would like to thank my advisor, Prof. Shannon Boettcher. Your deep scientific thinking and unrelenting drive to improve science has undoubtedly guided me as a graduate student and will continue to guide me as a scientist and citizen.

Next, I would like express gratitude towards all members of the Boettcher lab past and present. I have been so privileged to not only work side by side with such a large group of intelligent and motivated individuals, but to also be such good friends tehse same people outside of lab. Specifically, I thank Dr. Fuding Lin, Dr. Andrew Ritenour, Dr. Atom Smith, Dr. T.J. Mills, Dr. Sangeun Chun, Dr. Adam Batchellor, Dr. Jason Boucher, Dr. Matthew Kast, Dr. Michaela Stevens, Dr. Annie Greenaway, Dr. Christian Dette, Dr. Dongyu Xu, Dr. Lisa Enman, Elizabeth Cochran, Christopher Funch, Dr. Sebastian Oener, Raina Krivina and Jessica Fehrs. I would also like to give special thanks to Forrest Laskowski and Dr. Jingjing Qiu, who I have worked most closely with. Additionally, I would like to thank Jiang Deng and Ting Zhang, who I had the privilege of working with in the Boettcher lab as well.

I would also like to thank everyone who I have collaborated with throughout my time at University of Oregon. This includes, but is not limited to, Dr. Teddy Huang, Prof. Thomas Hamann, Hamed Hajibabaei, Prof. Kevin Sivula, Dr. Francesca Toma and Dr. Kyle Hite.

I would also like to express my sincere appreciation the faculty and staff of the SUNY Geneseo department of chemistry. Specifically, I recognize Prof. David Geiger for the extensive mentorship and advisement he provided, which started during my freshman year orientation. Thank you.

Also, I thank my doctoral committee, Prof. Mark Lonergan, Prof. George Nazin and Prof. Benjamín J. Alemań. Your insightful questions have pushed me to think deeper about my own work.

Lastly, I would like to thank my parents, Randall and Bonnie Nellist, as well as my siblings: Julie, Kyle, Katie and Melissa. This work would not be possible without a lifetime of their support. And my partner, Carolyn Levinn. We have been a team, not only academically but in life, for nearly eight years. Thank you for being there for me.

To those who have taught me, encouraged me and believed in me- thank you.

TABLE OF CONTENTS

Chapter Page

Chapter Page

Chapter Page

LIST OF FIGURES

Figure Page

Figure Page

Figure Page

LIST OF TABLES

Table Page

CHAPTER I
TOWARDS A CLARIFIED VIEW OF THE SEMICONDUCTOR|CATALYST INTERFACE FOR SOLAR WATER SPLITTING PHOTOANODES

Section “Development of Dual Working Electrode Photoelectrochemistry” contains co-authored work reproduced with permission from *Acc. Chem. Res.* **2016**, *49*, 733-740. Copyright 2016 American Chemical Society. This work was written by myself and Laskowski. F. A. L. with help from Boettcher, S. W. I edited this work, with assistance from Laskowski. F. A. L.; Lin, F. and Boettcher, S. W.

Section “Demonstrating Multimodal Imaging using Nanoelectrode Probes” contains co-authored work reproduced with permission from *Nanotechnology* **2017**, *28*, 095711. Copyright 2017 IOP Publishing Ltd. This work was written by myself and Huang, Z. Chen, Y.; Mark, A.; Gödrich, S.; Stelling, C.; Jiang, J.; Poddar, R.; Li, C.; Kumar, R.; Papastavrou, G. and Retsch, M. provided experimental assistance. Brunschwig, B. S.; Xiang, C. and Boettcher, S. W provided editorial assistance.

Section “Nanoscale Surface Potential Measurements of Water Oxidation Catalysts” contains co-authored work reproduced with permission from *Nat. Energy* **2018**, *3*,46−52. Copyright 2017 Macmillan Publishers Limited. This work was written primarily by me. Hajibabaei, H.; Sivula, K. and Hamann, T. W. provided experimental assistance. Laskowski, F. A. L.; Qiu, J. and Boettcher S. W. provided editorial assistance.

Section “Role of a CoPi Electrocatalyst on Bismuth Vanadate” contains co-authored work submitted to *ACS Energy Letters* (July 9, 2018). Reproduced with permission from *ACS Energy Letters*, submitted for publication. Unpublished work Copyright 2018 American Chemical Society. This work was written primarily by me. Qiu, J.; Laskowski, F. A. L. and Toma, F. M. provided experimental assistance. Boettcher S. W. provided editorial assistance.

Overview of the Progress and Limitation for Solar Water Splitting

The sun illuminates earth with 120,000 TW of power, making it the only viable renewable resource to meet the projected global energy demand of 28 TW by 2050.[1] While the cost of photovoltaics continues to fall, deployment is limited by the lack of inexpensive storage methods, which are essential due to daily and seasonal solar variability. Photoelectrochemical (PEC) cells offer a solution by directly converting sunlight and water into energy-dense H_2 fuel. PEC devices integrate a light absorbing semiconductor (sem) and electrocatalyst (cat) to catalyze the hydrogen/oxygen evolution reactions (HER/OER) at the photocathode and photoanode, respectively. Of these two half reactions, the OER requires higher kinetic overpotentials, even when catalyzed,[2,3] which limits the efficiency of the device.

In order to improve the performance of the OER at the photoanode, it is critical that we understand what processes are taking place at the sem|cat interface. This can be challenging,[4] as different groups have attributed the activity enhancement from the electrocatalyst when added to the semiconductor to better charge separation,[5] increased band bending within the semiconductor,[6,7] the reduction of interfacial recombination,[8,9] or simply more facile OER kinetics.[10,11] Unfortunately, the techniques used to study these systems fail to isolate the energetics of the catalyst alone, preventing a clear understanding of the catalyst's role.

To directly probe the energetics of the catalyst during operation, new experimental methods were required. As a result, Lin and Boettcher developed the dual working electrode (DWE) electrochemical technique, which provided new insights into the role of the OER catalyst and the importance of the sem|cat interface.[3] We will discuss the DWE technique and experimental results obtained extensively, in chapter two. This will include a discussion of the advantages and disadvantages of the technique. In chapter three, we demonstrate the testing of nanoelectrode atomic force microscopy probes to explore their electrochemical capabilities. We will then apply these probes, in chapter four, to bring the DWE to the nanoscale. This will allow us to study more complicated systems, like hematite. Finally, in chapter five we will extend our nanoscale DWE to explore catalyst coated $BiVO_4$ electrodes.

Development of Dual Working Electrode Photoelectrochemistry

Light-absorbing semiconductor electrodes coated with electrocatalysts are key components of photoelectrochemical energy conversion and storage systems. Efforts to optimize these systems have been slowed by an inadequate understanding of the semiconductor-electrocatalyst (sem|cat) interface. The sem|cat interface is important because it separates and collects photoexcited charge carriers from the semiconductor. The photovoltage generated by the interface drives "uphill" photochemical reactions, such as water splitting to form hydrogen fuel. Here we describe efforts to understand the microscopic processes and materials parameters governing interfacial electron transfer between light-absorbing semiconductors, electrocatalysts, and solution (Figure 1.1).

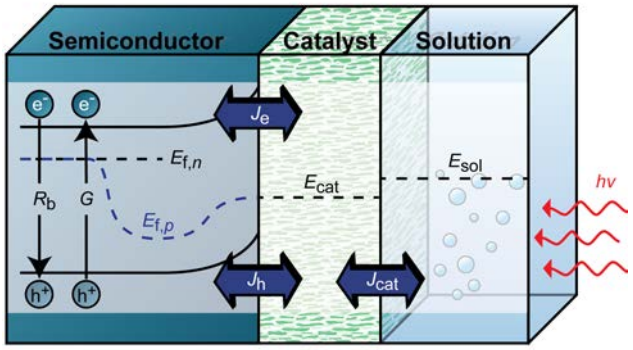

Figure 1.1. Depiction of the interfaces and band bending of a photoanode for water oxidation. Electron current (J_e) and hole currents (J_h) represent the transfer of charges between the sem|cat interface, whereas J_{cat} is chares within the catalyst that directly oxidize water.

We highlight the properties of transition-metal oxyhydroxide electrocatalysts, such as Ni(Fe)OOH, because they are the fastest oxygen-evolution catalysts known in alkaline media and are (typically) permeable to electrolyte. We describe the physics that govern the charge-transfer kinetics for different interface types, and show how numerical simulations can explain the response of composite systems. Emphasis is placed on "limiting" behavior. Electrocatalysts that are permeable to electrolyte form "adaptive" junctions where the interface energetics change during operation as charge accumulates in the catalyst, but is screened locally by electrolyte ions. Electrocatalysts that are dense, and thus impermeable to electrolyte, form buried junctions where the interface physics are unchanged during operation.

Experiments to directly measure the interface behavior and test the theory/simulations are challenging because conventional photoelectrochemical techniques do not measure the electrocatalyst potential during operation. We developed dual-working-electrode (DWE) photoelectrochemistry to address this limitation. A second electrode is attached to the catalyst layer to sense or control current/voltage independent from that of the semiconductor back ohmic contact. Consistent with simulations, electrolyte-permeable, redox-active catalysts such as Ni(Fe)OOH form "adaptive" junctions where the effective barrier height for electron exchange depends on the potential of the catalyst. This contrasts with sem|cat interfaces with dense electrolyte-impermeable catalysts, such as nanocrystalline IrO_x, that behave like solid-state buried (Schottky-like) junctions.

These results elucidate a design principle for catalyzed photoelectrodes. The buried heterojunctions formed by dense catalysts are often limited by Fermi-level pinning and low photovoltages. Catalysts deposited by "soft" methods, such as electrodeposition, form adaptive junctions that tend to provide larger photovoltages and efficiencies. We also preview efforts to improve theory/simulations to account for the presence of surface states and discuss the prospect of carrier-selective catalyst contacts.

Chapter II contains co-authored work published in volume 49 of *Accounts of Chemical Research* in 2016 (*Acc. Chem. Res.* **2016**, *49*, 733-740). This work was written by myself and Laskowski. F. A. L. with help from Boettcher, S. W. Computer modeling was performed by Mills, T.J. This work was edited by Laskowski, F. A. L. and myself, with assistance from Lin, F. and Boettcher, S.W.

Demonstrating Multimodal Imaging using Nanoelectrode Probes

Multimodal nano-imaging in electrochemical environments is important across many areas of science and technology. Here, scanning electrochemical microscopy (SECM) using an atomic force microscope (AFM) platform with a nanoelectrode probe is reported. In combination with PeakForce tapping AFM mode, the simultaneous characterization of surface topography, quantitative nanomechanics, nanoelectronic properties, and electrochemical activity is demonstrated. The nanoelectrode probe is coated with dielectric materials and has an exposed conical Pt tip apex of ~200 nm in

height and of ~25 nm in end-tip radius. These characteristic dimensions permit sub-100 nm spatial resolution for electrochemical imaging. With this nanoelectrode probe we have extended AFM-based nanoelectrical measurements to liquid environments. Experimental data and numerical simulations are used to understand the response of the nanoelectrode probe. With PeakForce SECM, we successfully characterized a surface defect on a highly-oriented pyrolytic graphite (HOPG) electrode showing correlated topographical, electrochemical and nanomechanical information at the highest AFM-SECM resolution. The SECM nanoelectrode also enabled the measurement of heterogeneous electrical conductivity of electrode surfaces in liquid. These studies extend the basic understanding of heterogeneity on graphite/graphene surfaces for electrochemical applications.

Chapter III contains co-authored work published in volume 28 of *Nanotechnology* in 2017 (*Nanotechnology* **2017**, *28*, 095711). This work was written by myself and Huang, Z. Chen, Y.; Mark, A.; Gödrich, S.; Stelling, C.; Jiang, J.; Poddar, R.; Li, C.; Kumar, R.; Papastavrou, G. and Retsch, M. provided experimental assistance. Brunschwig, B. S.; Xiang, C. and Boettcher, S. W provided editorial assistance.

Nanoscale Surface Potential Sensing of Water Oxidation Catalysts

Heterogeneous electrochemical phenomena, such as (photo)electrochemical water splitting to generate hydrogen using semiconductors and/or electrocatalysts, are driven by the accumulated charge carriers and thus the interfacial electrochemical potential gradients that promote charge transfer. However, measurements of the "surface" electrochemical potential during operation are not generally possible using conventional electrochemical techniques, which measure/control the potential of a conducting electrode substrate. Here we show that a nanoscale conducting tip of an atomic-force-microscope cantilever can sense the surface electrochemical potential of electrocatalysts *in operando*. To demonstrate utility, we measure the potential- and thickness-dependent electronic properties of cobalt (oxy)hydroxide phosphate (CoPi). We then show that CoPi, when deposited on illuminated hematite (α-Fe_2O_3) photoelectrodes, acts both as a hole collector and oxygen evolution catalyst. We demonstrate the versatility of the technique by comparing surface potentials of CoPi-decorated planar and mesoporous

hematite and discuss viability for broader application in the study of electrochemical phenomena.

Chapter IV contains co-authored work published in volume 3 of Nature Energy in 2017 (*Nat. Energy* **2018**, *3*,46−52). This work was written primarily by me. Hajibabaei, H.; Sivula, K. and Hamann, T. W. provided experimental assistance. Laskowski, F. A. L.; Qiu, J. and Boettcher S. W. provided editorial assistance.

Role of a CoPi Electrocatalyst on Bismuth Vanadate

Oxide/(oxy)hydroxide overlayers such as cobalt (oxy)hydroxide phosphate (CoPi) enhance the performance of $BiVO_4$ water-spitting photoanodes, but the mechanism of this enhancement remains unclear. We show that if the $BiVO_4$ layer is thin and incompletely covers an underlying conductive glass, the performance dramatically decreases as CoPi loading is increased. This is consistent with direct contact between the CoPi and conducting glass that leads to “shunt” recombination of photogenerated holes accumulated in the CoPi. For thicker $BiVO_4$ layers that completely cover the conducting glass, these shunt pathways are blocked. We then use a nanoelectrode atomic force microscopy probe to measure, in operando, the electrochemical potential of CoPi on thick $BiVO_4$ films under illumination (Figure 1.2). We find CoPi is charged to a potential necessary to drive water oxidation at a rate consistent with the measured photocurrent. CoPi acts as a hole collector and is the principal driver of water oxidation on $BiVO_4$.

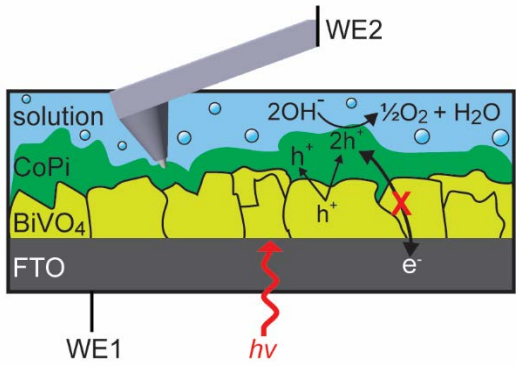

Figure 1.2. Experimental setup used for the sensing the potential of CoPi on $BiVO_4$, under illumination and applied bias.

Chapter V contains co-authored unpublished work that has been submitted to *ACS Energy Letters*. This work was written primarily by me. Qiu, J.; Laskowski, F. A. L. and Toma, F. M. provided experimental assistance. Boettcher S. W. provided editorial assistance.

CHAPTER II

SEMICONDUCTOR-ELECTROCATALYST INTERFACES: THEORY, EXPERIMENT, AND APPLICATIONS IN PHOTOELECTROCHEMICAL WATER SPLITTING

This chapter contains co-authored work published in volume 49 of *Accounts of Chemical Research* in 2016 (*Acc. Chem. Res.* **2016**, *49*, 733-740). This work was written by myself and Laskowski. F. A. L. with help from Boettcher, S. W. Computer modeling was performed by Mills, T.J. This work was edited by Laskowski, F. A. L. and myself, with assistance from Lin, F. and Boettcher, S.W.

Introduction

High-efficiency photoelectrochemical water-splitting systems require integrating electrocatalysts (cat) onto light-absorbing semiconductors (sem). Despite the central role that the sem|cat interface plays in collecting one carrier over the other and generating photovoltage, the energetics and charge transfer processes at catalyzed semiconductor interfaces are poorly understood. A simple picture is that the semiconductor absorbs light and separates charge while the catalyst increases the rate of the hydrogen- or oxygen-evolution reaction (HER or OER, respectively). Experiments by different groups, however, show that after deposition of OER catalysts onto *n*-type semiconductors, the photoelectrode characteristics (e.g. the photovoltage, photocurrent, and fill-factor) change in a way often inconsistent with this view.[1,2] Parallel hypotheses have attributed this behavior to changes in surface recombination,[3,4] band bending,[5] interface-charge trapping,[6] optical effects,[7] or kinetics.[8-11] Several factors make unravelling these different effects difficult. First, electrocatalysts are not well-defined electronic materials (e.g. a metal or semiconductor), but are often porous, hydrated, and redox-active solids. How does one describe such non-traditional electronic interfaces? Second, most of the semiconductor systems that have been studied are polycrystalline and/or nanostructured,

which makes interpreting elementary processes difficult. Third, there is a lack of experimental tools to directly measure the interfacial processes.

In this *Account* we discuss our use of simulation and new photoelectrochemical experiments to clarify the microscopic details of electron transfer in catalyzed water-oxidizing photoelectrodes. We connect the microscopic processes to the observable current-voltage responses, and discuss possible design principles for high-performance systems.

Figure 2.1 shows basic processes in a catalyzed photoelectrode. The semiconductor, catalyst, and solution are all characterized by electrochemical potentials (Fermi levels) which equilibrate in the dark ($E_{f,n}$, E_{cat}, and E_{sol}, respectively). Under illumination the concentration of minority holes increases and thus the hole quasi-Fermi level $E_{f,p}$ drops down from the electron level $E_{f,n}$ to create a photovoltage V_{ph} at the sem|cat interface. During steady-state photodriven oxygen evolution, E_{cat} is driven lower on the electron energy scale (more positive on the electrochemical scale) than E_{sol} (the thermodynamic oxygen potential), such that there is a net positive current from catalyst to solution. The degree to which $E_{f,p}$ separates from $E_{f,n}$ at the semiconductor surface is governed by the relative forward and reverse rates of electron and hole transport at the sem|cat interface in addition to the rates of bulk recombination (R_b) and generation (G). The hole current density is given by $J_p = \mu_p p \nabla E_{f,p}$ where μ_p is the hole mobility and $\nabla E_{f,p}$ is the hole quasi-Fermi-level gradient.

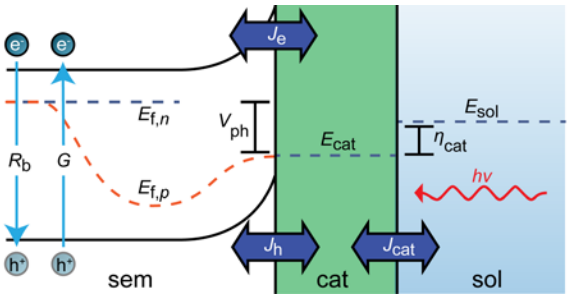

Figure 2.1. Steady-state currents and Fermi levels at an illuminated electrocatalyst-modified *n*-type semiconductor in solution. The symbols are defined in the text.

Traditional photoelectrochemical measurements use an ohmic contact to the back of the semiconductor (i.e. the left side of the diagram in Figure 2.1) to sweep the semiconductor potential E_{sem} (which is also the majority-carrier Fermi level $E_{f,n}$ in the bulk), and measure the resulting current in both the light and dark. It is difficult from such measurements to determine how the individual charge-transfer, catalysis, and recombination steps affect the *J-V* response. First, it is not possible to determine which portion of the total applied potential (i.e. $qV_{app} = E_{sem} - E_{sol}$) drops at the sem|cat interface versus at the cat|sol interface because one cannot determine E_{cat}. Further, the current measured is the sum of the net electron and hole currents and it is not possible to distinguish whether the holes or electrons flow into the catalyst or directly into the solution.

A number of techniques have been used to augment traditional photoelectrochemical measurement. Transient absorption spectroscopies[12] provide insight into the various recombination processes,[5,6] though data interpretation is complicated by the pulsed-laser excitation – photoelectrodes operate at steady state under low light intensity. Methods based on impedance are powerful,[13] but rely on fitting equivalent circuits, which are complicated for multicomponent systems. Here we describe alternative methods that provide direct information about the interface, as well as theory and simulation to corroborate the measurements.

Materials: Semiconductors and Electrocatalysts

Among device geometries proposed for a solar-water-splitting system, one compelling option employs two semiconductors in series, with different bandgaps, to absorb different portions of the solar spectrum.[14] One semiconductor, operating as a photoanode, drives water oxidation to form O_2(g), while the other, operating as a photocathode, drives water reduction to form H_2(g). Electrocatalysts decorate both semiconductors to increase the kinetics of the fuel-forming reactions. While the sem|cat interface is important in both, we focus here on the photoanode.

Semiconductors. Oxides, such as Fe_2O_3, $BiVO_4$, and WO_3, have been studied extensively as water-oxidizing photoanodes, in part because they can be simply made and, being already oxidized, are reasonably stable under the appropriate-pH OER

conditions.[15] The oxides are typically polycrystalline and the sem|cat interface thus likely non-uniform. Recently, there has been a revived interest in using thin oxide films to stabilize *n*-Si and *n*-GaAs photoanodes which have superior electronic properties (mobility, carrier lifetime) but corrode under anodic conditions.[16] Fabrication of high-quality *pn* junctions, that provide for large photovoltages, is straightforward on Si/GaAs. For oxide photoelectrodes there are limited methods to fabricate solid-state *pn* junctions; tuning the properties of the sem|cat interface is therefore particularly important.

Electrocatalysts. To understand the interface, it is critical to understand the electrocatalyst's electronic and electrochemical properties. In the simplest case the catalyst is a dense solid with high electrical conductivity (e.g. a metal or degenerate semiconductor). The sem|cat interface is thus expected to form a Schottky-type heterojunction. For example, nanocrystalline IrO_2 films exhibit metallic conductivity while nanocrystalline Co_3O_4 films are *p*-type semiconductors.[17]

Many catalysts, however, are not dense crystalline solids.[18] Under alkaline conditions the fastest known water oxidation catalysts are Ni-Fe oxyhydroxides ($Ni_{1-x}Fe_xO_yH_z$ with $x \sim 0.25$).[19,20] These oxyhydroxide catalysts appear thermodynamically stable; Ni-oxide-based catalysts reconfigure to the oxyhydroxide structure under OER conditions.[19] They are highly disordered but locally consist of Ni(Fe)OOH nanosheets.[21,22] Each Ni in the film is electrochemically active and can be cycled between the 2^+ and $3^+/4^+$ oxidation states.[23] This requires both electrical and ionic conductivity throughout the "solid" catalyst. We term this catalyst type "electrolyte-permeable" (Figure 2.2a). Electrolyte-permeable catalysts display interesting electronic properties. $Ni(Fe)(OH)_2$ in the resting state is an electronic insulator. Once oxidized to Ni(Fe)OOH it becomes conductive. Other common catalysts also show "bulk" redox behavior and "volume activity" consistent with electrolyte-permeability. These include Co(Fe)OOH (which also shows conductivity-switching),[24,25] "CoPi" and "NiBi" in near-neutral solutions,[26,27] and electrodeposited hydrous oxides of IrO_xH_y and RuO_xH_y.[28,29] Thermally prepared IrO_2 oxides don't display volume electrochemistry; they are dense and electrolyte-impermeable.

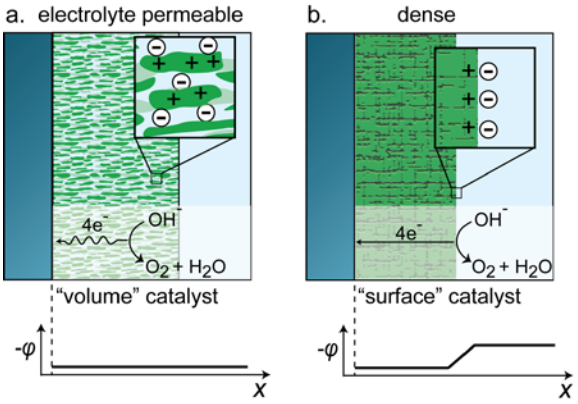

Figure 2.2. Comparison of electrolyte-permeable and non-permeable catalyst layers. (a) Electrolyte-permeable catalysts screen electronic charge on the catalyst with mobile solution ions (inset), resulting in no electrostatic potential drop across the catalyst. (b) Dense films are impermeable to electrolyte; any charge on the catalyst is balanced by a classical double layer.

Classification of Interface Types

The physical structure of the catalyst (dense solid or electrolyte permeable) dramatically affects the nature of the sem|cat interface and how it behaves in the dark and under illumination. The qualitative basis for this hypothesis is simple. Dense catalysts, such as Pt, crystalline NiO, or crystalline IrO_2, must accommodate injected charge near the electrolyte/catalyst boundary to achieve charge neutrality (Figure 2.2b). This results in change in the electrostatic potential drop across a classical Helmholtz layer (ΔV_H). As catalytic activity decreases, $\Delta V_{H,cat}$ across the cat|sol interface required to drive the reaction at a given photocurrentcurrent density increases. We refer to sem|cat interfaces with electrolyte-impermeable and electronically conductive catalysts as "buried" junctions, consistent with photoelectrochemical terminology.[30,31]

If the catalyst is electrolyte-permeable and redox active, holes that accumulate in the catalyst drive oxidative redox chemistry (one example is $Ni(OH)_2 + OH^- \rightarrow NiOOH + H_2O + e^-$). Because the electronic charge is compensated by the coupled ion motion within the electrolyte-permeated catalyst, *no electrostatic potential drop is expected within the catalyst layer or across the cat|sol interface* (Figure 2.2a). This also assumes good catalyst electronic conductivity, as we demonstrated experimentally for NiOOH/CoOOH based systems.[18] Instead the "work function" of the catalyst changes in

situ (Figure 2.3b). This type of interface is practically important because, as discussed above, the most-active Ni(Fe)OOH and Co(Fe)OOH OER catalysts in neutral-to-basic media are electrolyte permeable. Such catalysts have been used in the best-performing oxide photoanodes for water oxidation, e.g. hydrous IrO_x catalyzed Fe_2O_3 and FeOOH/NiOOH catalyzed $BiVO_4$.[11,32] We have termed these sem|cat interfaces "adaptive", following work on photoactive mixed ionic/electronic conducting polymer interfaces.[33]

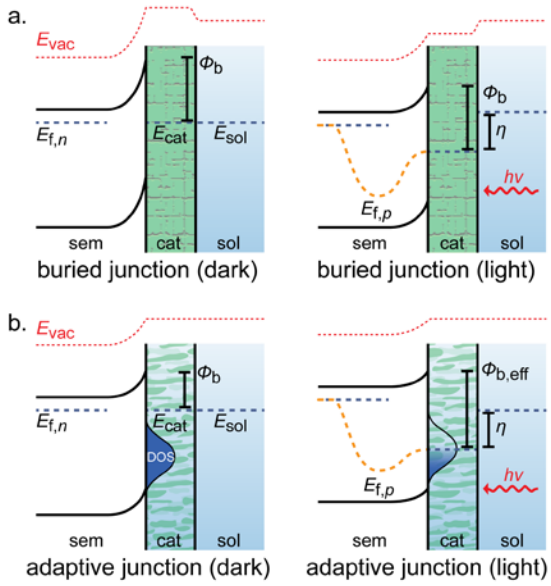

Figure 2.3. Band diagrams for sem|cat interfaces. (a) Dense and (b) electrolyte-permeable catalysts at (left) dark equilibrium and (right) under illumination at a fixed current density. E_{vac} is the vacuum energy level; other symbols are defined in the text. The barrier height ϕ_b is the separation between the semiconductor conduction band edge and the catalyst Fermi level. For the buried junction, ϕ_b remains constant between dark and light conditions. For the adaptive junction, the effective barrier height, $\phi_{b,eff}$ increases under illumination at a fixed current density as a result of catalyst oxidation. The hole quasi-Fermi level is shown to decay back to the bulk Fermi level at the back contact over a shortened distance for clarity.

Whether a sem|cat interface is expected to be of the "buried" or adaptive type is determined by whether or not electrolyte can physically permeate between the catalyst and semiconductor layers and thus completely screen catalyst charge. A physically realizable adaptive junction interface could thus also be one where crystalline OER catalysts with an electrolyte-permeable shell are deposited on a semiconductor surface.

Dispersed nanoparticle catalysts that form *mixed* buried and electrolyte junctions and that are spatially inhomogeneous are another interface class that will not be discussed here.[14]

Semiconductor-Catalyst Interfacial Charge Transfer

Theory and simulation help in predicting the behavior of catalyzed photoelectrodes and determining whether experimental data are consistent with proposed microscopic mechanisms. Although the theory of sem|sol interfaces is well developed,[34] there has been limited work to account for surface-attached electrocatalysts. Previously, equivalent electrical circuits were used to model sem|cat|sol systems.[35-37] This approach implicitly assumes that the electrocatalytic process at the cat|sol interface is independent of the photovoltage generation and charge separation process at the sem|cat interface. This assumption is valid when the catalyst layer is dense and electrically conductive (i.e. a buried junction, Figure 2.3a), or when the catalyst is coated on a solid-state photovoltaic cell.[38] Equivalent-circuit models cannot model photoelectrodes with electrolyte-permeable catalysts where, as the catalyst drives OER, the catalyst and the interface both change (Figure 2.3b).

We developed a model for sem|cat|sol systems that accounts for the kinetics of charge transfer between the semiconductor, catalyst, and solution for both buried and adaptive junctions.[39] We numerically simulate generation, recombination, drift, and diffusion in the semiconductor. We derive the boundary conditions for the semiconductor/catalyst current (J_{jxn}) based on the simulated equilibrium ($\overline{n}_{\mathrm{s}}, \overline{p}_{\mathrm{s}}$), and non-equilibrium ($n_{\mathrm{s}}, p_{\mathrm{s}}$) surface electron and hole concentrations.

We tested the model with buried junctions where the results from simpler equivalent circuits are expected to be valid. We use

$$J_{\mathrm{jxn,buried}} = k_{\mathrm{p}}\left(p_{\mathrm{s}} - \overline{p}_{\mathrm{s}}\right) - k_{\mathrm{n}}\left(n_{\mathrm{s}} - \overline{n}_{\mathrm{s}}\right) \quad (1)$$

where k_{p} and k_{n} are the forward rate constants for hole and electron transfer, respectively, between the semiconductor and the dense catalyst. The first term, $k_{\mathrm{p}}\left(p_{\mathrm{s}} - \overline{p}_{\mathrm{s}}\right)$, represents forward and backward hole currents, respectively, and the second term, forward and backward electron currents. Here, $J_{\mathrm{jxn,buried}}$ does not depend on the catalyst

potential because charge accumulates and causes a potential drop at the cat|sol interface, without affecting the buried interface. This expression simplifies to the ideal photodiode equation if a constant photogenerated hole flux $J_{\mathrm{ph}} = k_{\mathrm{p}}\left(p_{\mathrm{s}} - \overline{p}_{\mathrm{s}}\right)$ is assumed (thereby ignoring backwards hole current) and the electrons are in quasi-equilibrium such that $k_{\mathrm{n}}(n_{\mathrm{s}} - \overline{n}_{\mathrm{s}}) = J_0(e^{-qV/kT} - 1)$. Notice that, for an *n*-type semiconductor, the majority-carrier reverse current (electrons moving from catalyst to semiconductor) is the equilibrium exchange current, $J_{0,n} = k_{\mathrm{n}}\overline{n}_{\mathrm{s}}$, which is set by the equilibrium barrier height at the sem|cat interface.

For electrolyte-permeable catalysts (adaptive junctions) the situation is different, since the redox state of the electrocatalyst film is variable. This effectively changes the "work-function" of the catalyst during operation. The sem|cat interface current $J_{\mathrm{jxn,adapt}}$ now depends on the electrochemical potential of the catalyst layer V_{cat} as

$$J_{\mathrm{jxn,adapt}} = k_{\mathrm{p}}\left(p_{\mathrm{s}} - \overline{p}_{\mathrm{s}}e^{qV_{\mathrm{cat}}/kT}\right) - k_{\mathrm{n}}\left(n_{\mathrm{s}} - \overline{n}_{\mathrm{s}}e^{-qV_{\mathrm{cat}}/kT}\right). \quad (2)$$

Note that the forward currents ($k_{\mathrm{n}}n_{\mathrm{s}}$ and $k_{\mathrm{p}}p_{\mathrm{s}}$) are the same as the buried junction case. This relies on the assumption that changing the charge state of the electrocatalyst film does not substantially alter the electronic states in the catalyst that are at energies near the semiconductor valence and conduction band edges. It also ignores the role of surface states in mediating charge transfer, which we discuss below.[40] The reverse currents, however, are influenced by the change in the catalyst potential (V_{cat}), through the addition of the $e^{-qV_{\mathrm{cat}}/kT}$ term. This term accounts for the fact that the Fermi level in the catalyst layer moves independent of the semiconductor band positions, thus modeling the "effective" barrier height(s) for charge transfer into the semiconductor from the catalyst.

The catalyst further reacts with the solution, which we model using a Butler-Volmer expression that represents the typical experimental response,[19]

$$J_{\mathrm{cat}} = J_{\mathrm{o,cat}}\left(e^{qV_{\mathrm{cat}}/2kT} - e^{-qV_{\mathrm{cat}}/2kT}\right), \quad (3)$$

where $J_{\mathrm{o,cat}}$ is the exchange current density for the OER reaction on the catalyst. Equations (1) - (3) thus govern the carrier fluxes between the semiconductor, catalyst, and solution in the two cases discussed. We also simulated molecular catalyst systems.[39]

The most significant simulation result is the observation that for the electrolyte-permeable catalyst, the *J-V* curves are nearly insensitive to the catalyst activity $J_{o,cat}$ (when E_v is much more positive than E_{sol}), in contrast to the buried junction case (Figure 2.4). This behavior is explained by the steady-state band diagrams shown in Figure 2.4b. For the electrolyte-permeable case, the catalyst Fermi level moves down (more anodic) under operation to compensate for slow OER kinetics. This leads to a larger "effective" barrier height $\phi_{b,eff}$ and thus a larger sem|cat photovoltage.

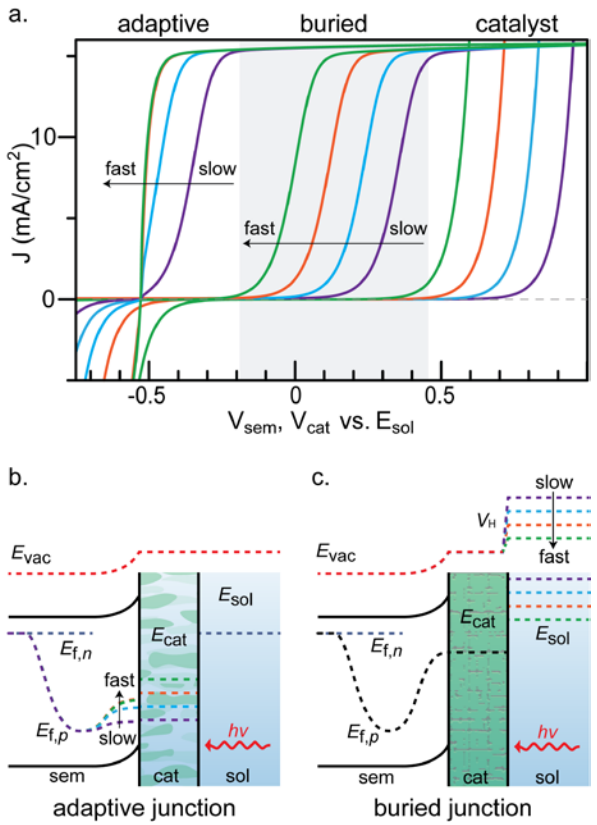

Figure 2.4. Simulations of sem|cat junctions**.** (a) Comparison of simulated illuminated *J-V* curves for a range of $J_{o,cat}$ (i.e. catalyst activities) for the buried and adaptive models.[39] Catalyst-only dark curves are shown also. Qualitative band diagrams under illumination for the (b) "adaptive" sem|cat interface at short circuit (V_{sem} = 0 vs. V_{sol}) and (c) the "buried" sem|cat interface at the applied potentials of 0.2 V (green, fast catalyst) to 0.5 V (purple, slow catalyst) needed to maintain a the same current in each case. E_{cat}, $E_{f,p}$, and E_{sol} are sketched as colored curves that correspond to those in (a) for the catalyst layers with different exchange currents (i.e. slow versus fast), but the same resting state Fermi level (E_{cat} = E_{sol}). Quantitative simulations can be found in reference 40.

In the case of the dense catalyst, increased activity requires the accumulation of charge at the cat|sol interface "consuming" a portion of the photovoltage in the semiconductor. These simulation results provide a platform from which to interpret experimental data discussed below. For mesoscopic or highly nanostructured semiconductor photoelectrodes, the form of the expressions governing the surface carrier concentrations would be different, but the fundamental differences between electrolyte screening in dense and permeated catalysts systems is the same.

In Situ Electrical Measurements of sem|cat Interfaces

To address the experimental limitations of conventional photoelectrochemistry and to collect data that can be directly compared to theory, we developed a "dual-working-electrode" photoelectrochemical (DWE PEC) measurement platform (Figure 2.5).[41]

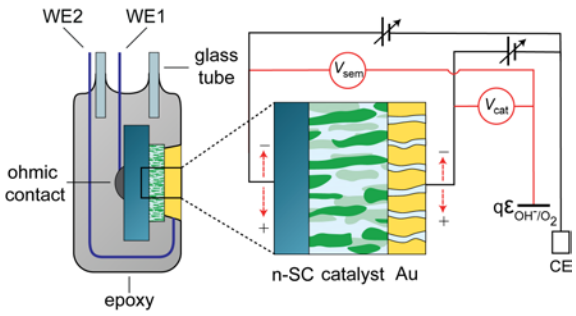

Figure 2.5. Dual-working-electrode photoelectrochemistry. Semiconductor and electrocatalyst potentials are independently measured/varied relative to the reversible oxygen potential, ε_{O_2/OH^-} (which is equivalent to E_{sol} in the model). WE1 makes an ohmic contact to the semiconductor and WE2 is attached to a thin, electrolyte-porous gold layer deposited onto the catalyst.

We tested the platform by characterizing catalyst-coated single-crystal *n*-TiO_2, which is useful for fundamental studies. TiO_2 is commercially available as single crystals with well-defined surfaces, has reproducible photoelectrochemical response and is essentially insoluble at all pH.

We spin-cast or electrodeposit catalyst films on the TiO_2 surface and make ohmic contact to the back. The catalyst is coated with a thin Au (~10 nm) layer using vacuum evaporation. We ensure no shorting between Au and TiO_2 using electrical measurements. The Au forms a porous conductive film on the catalyst surface that is electrolyte permeable and optically transmissive. We confirm the layer is permeable by measuring the reversible electrochemistry and OER activity of the catalyst layer using the top Au film as the working electrode.

The Au makes electrical contact to the catalyst film and thus can be used to measure or control the catalyst potential *in situ* and monitor the current passed through the catalyst. The DWE PEC experiment is implemented using a bipotentiostat, which allows simultaneous control of the two-working electrode (WE) potentials. We define WE1 as the back contact to the TiO_2 and WE2 as the Au-catalyst surface contact. Despite direct solution contact, the Au is assumed to be in quasi-equilibrium with the catalyst layer because the kinetics for oxygen evolution and reduction on Au are slow.

We focused our initial study on two catalyst materials – nanocrystalline IrO_x and $Ni(Fe)O_xH_y$ films that were predicted to form buried and adaptive junctions, respectively.[41] We first monitored the flow of holes and electrons in the light and dark, respectively, by collecting the carriers that flow into the catalyst with WE2. The data shows that the holes generated in TiO_2 flow first into the catalyst, prior to driving OER. This result was important because for the related Co-Pi/Fe_2O_3 system, it was suggested that the holes bypass the catalyst and directly react with the electrolyte.[42]

We measured the sem|cat junction V_{oc} by varying E_{cat} and measuring E_{sem} at steady state under illumination. The difference between E_{cat} and E_{sem} is the sem|cat $V_{oc,}$ which cannot be measured using conventional photoelectrochemistry. The data (Figure 2.6) show that the junction V_{oc} is independent of E_{cat} for $TiO_2|IrO_x$ and a linear function of E_{cat} for $TiO_2|Ni(OH)_2$, as predicted from simulations for a buried and adaptive junction, respectively. Other DWE measurements were also consistent with the adaptive and buried junction concepts.[41]

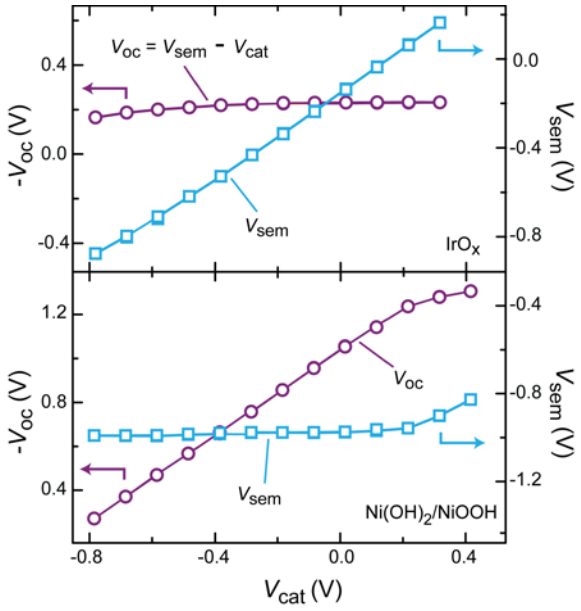

Figure 2.6. Experimental sem|cat open-circuit photovoltages. (top) IrO_x-coated and (bottom) $Ni(OH)_2$/NiOOH-coated TiO_2. For buried junctions, the sem|cat V_{oc} is independent of the catalyst potential V_{cat}.

Catalyst Activity and Electrolyte Permeability

The DWE technique is limited by the need for devices with an integrated second working electrode. Fabricating such structures and ensuring that the Au layer does not short to the underlying semiconductor layer can be technically challenging. To test a wide range of electrocatalysts on single-crystal TiO_2, and further test the predictions of theory, we also used conventional current-voltage and impedance analysis.[17]

We found that for electrolyte-permeable catalysts electrodeposited on TiO_2 (hydrous IrO_x, CoO_xH_y, FeO_xH_y, and NiO_xH_y) the photovoltage output and fill factor for the combined system was *independent* of the catalyst identity (Figure 2.7, top). When the catalysts were spun cast in a dense, nanocrystalline form, the junction performance varied dramatically for the different catalysts and was worse than with the electrolyte-permeable catalysts. Electrochemical impedance-spectroscopy analysis of the electrodes showed that the electrolyte-permeable catalysts did not effect the semiconductor band positions, while the dense catalyst layers caused large changes to the impedance data. These observations are consistent with our simulations[39] that predict for semiconductors with deep valence

bands, like TiO_2, the device performance should be independent of the electrocatalyst activity if it is electrolyte permeable.

For photoelectrodes with smaller bandgaps, and thus less-positive valence-band positions, the activity of the electrocatalyst is important. This is because E_{cat}, even in the adaptive-junction limit, cannot move more positive than the valence-band edge. Analyzing the interface properties as a function of catalyst activity for small band gap semiconductors such as $BiVO_4$ or *n*-Si, will thus be important for future work.

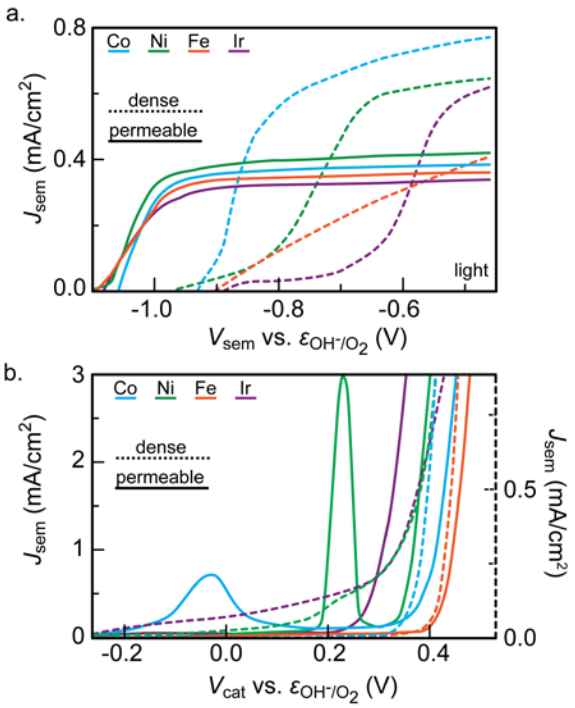

Figure 2.7. Experimental *J-V* curves for dense and electrolyte-permeable catalysts. (a) Dense oxide catalysts (dashed) on TiO_2 show varied response due to different junctions, while permeable electrodeposited catalysts on TiO_2 (solid) show similar responses. (b) The response of the same series of catalysts deposited on conductive electrodes.

The Role of Surface States

Surface states cause a variety of photoelectrode behavior including increasing surface recombination,[6] storing charge,[43] and pinning the Fermi-level.[8,44] While the basic effects of surface states on the steady-state and dynamical response of photoelectrodes have been derived, [45-48] there is no predictive model to describe the effect of surface

states in the presence of a catalyst overlayer. The concept of a "surface state" (ss) itself is poorly defined in the case of a boundary between two phases where an interphase region may exist, as pointed out by Peter.[48] The surface interphase may trap electronic charge, but also may or may not allow for partial permeation of electrolyte (consider the possibility of an α-Fe_2O_3 crystal with a hydrated FeOOH surface layer). Existing models do not account for the possible effects of electrolyte screening on ss charge. They also make various simplifying assumptions (e.g. the Gärtner approximation, neglecting backwards transfer from surface states to semiconductor, or assuming surfaces states only communicate with either the semiconductor or the solution).[49]

We developed a model describing the semiconductor physics (generation, recombination, drift, diffusion) combined with the kinetics of carrier exchange between coupled surface-state, catalyst, and solution subsystems. We account for cases where charge in the surface states is screened by electrolyte and where it is not. While the simulations will be published elsewhere, we highlight key insight in this *Account*.

The effects of surfaces states are most pronounced when the catalyst layer is electrolyte permeable and the charge in the surface state cannot be screened by the electrolyte (e.g. because the state is directly on the dense semiconductor, solution ions cannot permeate around it). We assume that the surface states are in quasi-equilibrium with the catalyst (i.e. that they have the same Fermi level) because the electron-exchange rates between the metal cations of the catalyst and surface states are faster than those of water oxidation. As the filling of the surface state changes there is thus a change in the Helmholtz potential ($\Delta V_{H,ss}$) at the semiconductor surface.

Simulations show that adding catalyst to a semiconductor surface can change the surface-state charge by reducing the potential needed to drive holes into solution. This can lead to an *apparent* "passivation" of the states. The effect, however, is not chemical passivation. Figure 2.8a and 2.8c show how, for a poor catalyst, E_{cat} must move far positive of E_{sol} in order to drive the catalytic reaction at the light-limited photocurrent rate. Because the surface state and catalyst are in quasi-equilibrium, they "charge" together. The surface states thus charge more for a slow catalyst than for a fast one. These results may help explain the photoelectrochemical response of Co

oxyhydroxide/phosphate (CoPi) catalysts on *n*-Fe_2O_3, which is known to have a high surface-state density.[5,6,10,12,13,42,50] We suggest CoPi increases the rate of water oxidation, moving the steady-state surface potential more negative, reducing the surface-state charging (and hence $\Delta V_{H,ss}$), and thus shifting the photocurrent onset potential cathodic. Some evidence for such an effect of CoPi on *n*-Fe_2O_3 has been observed.[50]

In the limit of low surface-state density, the surface states do not hold enough charge to significantly change $\Delta V_{H,ss}$ and the interface behaves as an adaptive junction where catalyst activity doesn't substantially affect photoelectrode response (Figure 2.8c and d).

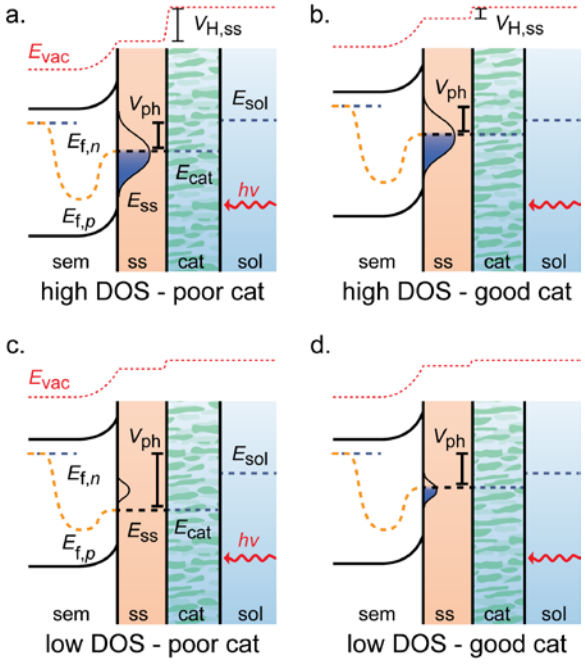

Figure 2.8. Effect of surface states on permeable catalysts. In the limit of a large surface-state density (a and b), permeable catalysts behave like buried junctions and changes in catalyst activity cause changes in $V_{H,ss}$. In the low-surface-state-density limit (c and d), changes in surface-state filling don't affect $V_{H,ss}$ and the system behaves like the adaptive junction.

Outlook: Designing Improved Interfaces

The PEC and simulation results discussed here demonstrate the role of electrolyte-permeability and catalyst charging on interface properties and photoelectrode

response. The “adaptive-junction” concept explains why the best-performing oxide photoanodes use catalysts deposited using “soft” conditions (e.g. electrodeposition) where the catalyst remains disordered and electrolyte-permeated.[32] These findings are expected to apply to photoelectrodes with smaller band-gaps (e.g. Fe_2O_3, $BiVO_4$, or Si) although the adaptive interface may not be able to entirely compensate catalyst overpotential as on TiO_2.

There are additional strategies/principles for the design of improved sem|cat|sol interfaces. One approach is to create optimized buried junctions with conductive and chemically stable surfaces onto which the highest-activity catalysts, such as Ni(Fe)OOH, can be deposited. This approach works well for Si and GaAs, because processes are established to fabricate solid-state junctions that generate photovoltages approaching the theoretical bulk-recombination limits.[51] For many materials, such as oxides, methods to manufacture solid-state junctions are not well developed.

Fundamentally, the rate of forward electron transfer (i.e. recombination current) must be minimized to maximize photoanode performance (see Eqn. 2). One way to reduce electron transfer is to move the band-edge positions to maximize band bending and minimize the surface concentration of electrons n_s.[52] The second is to selectively reduce the rate constant for electron transfer into the catalyst over that for holes, i.e. make the catalyst a *carrier-selective* contact.[53] By tuning composition one might create a catalyst with few electronic states available at the appropriate energy to accept electrons from the conduction band, and many states available to accept holes (Figure 2.9).

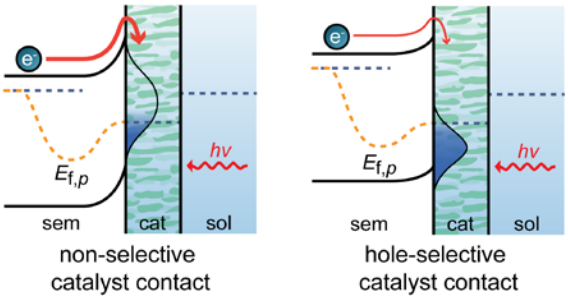

Figure 2.9. Effect of catalyst on interface carrier selectivity.

Conclusion and Bridge

This chapter has provided context regarding the importance of the sem|cat junction. As mentioned in this section, these findings are expected to extend to photoelectrodes with smaller band-gaps, including Fe_2O_3 and $BiVO_4$. However, these materials presented challenges when attempting to apply the DWE PEC technique due to their inhomogeneous catalyst coverage, highly structured morphology and limitations of catalyst loading. By advancing the DWE PEC method to the nanoscale, these restrictions can be avoided. In Chapter III, we will discuss testing of the electrochemical capabilities of new nanoelectrode probes for atomic force microscopy. We then apply these probes to nanoscale DWE PEC measurements in Chapters IV and V.

CHAPTER III

ATOMIC FORCE MICROSCOPY WITH NANOELECTRODE TIPS FOR HIGH RESOLUTION ELECTROCHEMICAL, NANOADHESION, AND NANOELECTRICAL IMAGING

Chapter III contains co-authored work published in volume 28 of *Nanotechnology* in 2017 (*Nanotechnology* **2017**, *28*, 095711). This work was written by myself and Huang, Z. Chen, Y.; Mark, A.; Gödrich, S.; Stelling, C.; Jiang, J.; Poddar, R.; Li, C.; Kumar, R.; Papastavrou, G. and Retsch, M. provided experimental assistance. Brunschwig, B. S.; Xiang, C. and Boettcher, S. W provided editorial assistance.

Introduction

Understanding the liquid-liquid, solid-liquid or liquid-gas interface is important for the study of interfacial charge transfer, corrosion and biological processes.[1-4] However, macroscale measurements of these interfaces often neglect the spatial variations that may exist on the micro- or nano-scales. The need to better understand these spatial variations led to the development of scanning electrochemical microscopy (SECM) by Bard *et al.* in 1989.[5] SECM generally uses an ultramicroelectrode (UME) scanning a horizontal plane above the sample to spatially resolve local electrochemical properties.[2,3] However, the electrochemical response of the UME probe to the sample surface underneath depends both on the probe-sample distance and the electrochemical activity of the surface. Keeping the probe at a constant-height leads to the convolution of topography with the collected electrochemical information, preventing a direct correlation of electrochemical activity with the surface landscape, unless the topographic variation is negligible compared to the tip radius or the tip-sample distance. Another limitation of traditional SECM lies in the implementation of UMEs that have characteristic dimensions of from 5 to 25 μm. As the spatial resolution is in part determined by the UME dimensions, it is challenging for a conventional SECM to achieve sub-μm resolution. Since the invention of SECM, approaches have been introduced to both decouple topographic influence on the electrochemical response and to

achieve higher spatial electrochemical resolution. These include the use of nanoelectrodes[6,7] and the implementation of advanced imaging modes, such as shear-force mode,[8] alternating current SECM,[9] and SECM combined with scanning-ion-conductance microscopy (SICM-SECM)[10] or atomic-force microscopy (AFM-SECM)[11]. Among these approaches, AFM-SECM has emerged as a particularly promising approach.[1,12,13]

Combined AFM-SECM enables the nanoelectrode to serve as the AFM probe, while also utilizing regular AFM imaging and precise control of the probe position. An early attempt of AFM-SECM was by Zhu *et al.* in studying pitting corrosion of stainless steel using a sealed Pt-Ir probe in constant-height mode controlled by an AFM feedback loop.[14] The scan height was as low as 100 nm allowing sub-μm features to be resolved. Macpherson and Unwin first demonstrated simultaneous topography/activity imaging using an AFM-SECM in contact mode for studying dissolution of potassium ferrocyanide and diffusion through track-etched membranes.[15] However, this approach is limited to robust and nonconductive substrates, as the probe is in intimate contact with the surface during scanning. Sharp AFM probes with recessed ring electrodes were developed by Kranz *et al.*[12,16-20] These recessed ring electrodes allow for high-resolution topographic imaging while also collecting electrochemical activity at a constant electrode-sample height set by the tip pyramid dimensions. This prevents the electrode from contacting the sample and reduces the influence of topographic variation to electrochemical response. This type of probe has been successfully employed for a variety of applications.[21] Recent examples include the implementation of AFM-SECM combined with PeakForce tapping to simultaneously map nanomechanical properties and image the tapping-cycle-averaged electrochemical activity.[12,22] However, electrochemical resolution and sensitivity is limited by the large ring electrode diameter (typically ~ 500 nm) and the electrode-sample distance (typically > 500 nm). We note that, recently, imaging of Au nanostars of < 100 nm on a soft substrate was demonstrated with AFM-tip integrated nanodisc electrodes of radius < 50 nm with a recessed height ~200 nm by Knittel and Kranz et al.[22]

The application of interleaved scan mode, a dual-pass probe scanning pattern, enables the precise control of electrode-sample distance at sub-nanometer resolution for electrochemical imaging with enhanced resolution. First described by Macpherson and

Unwin,[23] interleaved scan mode uses the first trace of the AFM cantilever to record sample topography and other AFM information, then lifts the tip from the surface and rescans in SECM mode while maintaining a user-defined tip-surface distance. Insulated conductive probes with an exposed apex are employed for this measurement. Fabrication techniques include electrochemical etching of Pt or Au wires,[24,25] micro-electro-mechanical systems (MEMS),[19,26-30] and abrasion.[31] While many of these approaches are described as "batch fabrication process," the development of robust, reliable, and reproducible probes has been limited. This technical barrier has prevented widespread implementation of this AFM-SECM approach and only few applications of practical significance have been reported.[1]

Recently, we briefly reported an AFM-SECM nanoelectrode probe with an exposed conical tip apex of ~200 nm in height and of ~25 nm in end tip radius.[32] Using these probes, paired with the recently widely-adopted PeakForce tapping AFM mode,[33] and interleaved scan mode, we demonstrated preliminary examples of the simultaneous collection of topography, mechanics, surface conductivity and electrochemical activity. This PeakForce SECM mode enables sub-100 nm spatial resolution for electrochemical imaging with sub-50 nm resolving power for other AFM properties. The spatial resolution demonstrated in electrochemical mapping is among the best of previous AFM-SECM studies. Different from approaches using recessed ring electrode probes,[12,22] the nanoelectrode with a conical conductive tip allows direct contact of the active electrode with the sample surface. This capability enabled the collection of high-resolution electrical conductivity maps in liquid, and local current-voltage characteristics provide insight about the effects of liquid on the junction behavior at metal/semiconductor interfaces.[32]

In this work, we describe the detailed development and characterization of these pre-mounted nanoelectrode probes, including their chemical compatibility and long-term chemical and physical stability. To the best of our knowledge, these are the most extensive studies on developed AFM-SECM nanoelectrode probes that have been reported. Numerical simulation is used to understand the electrochemical response and compare approach curves from both experiment and simulation. We show the utility of sample-generation / tip-collection electrochemical studies on an Au nanomesh electrode

to map electrochemical reactivity. Further, nanoelectrical measurements in liquid are demonstrated, in particularly we highlight electrical measurements under an organic solvent in a controlled-atmosphere glove box that are relevant to battery studies. These new capabilities are employed here to characterize a highly oriented pyrolytic graphite (HOPG) electrode, which exhibited heterogeneous electrical properties due to anisotropic sample conductivity in liquid and surface defects with enhanced local electrochemical activity and mechanical heterogeneity. The results substantially extend the understanding heterogeneity at the graphite/graphene surface for electrochemical applications. In sum, this work demonstrates a powerful multimodal nano-imaging platform that should be of utility across electrochemical science and technology.

Materials

Chemicals. Hexaammineruthenium(III) chloride ($[Ru(NH_3)_6]Cl_3$, 98%, Aldrich / ABCR) was used as a reversible redox couple. Potassium chloride (BioXtra, ≥99.0%, Aldrich) and potassium nitrate (PURATREM, 99,999%, ABCR) were used as supporting electrolytes.

Samples. Highly oriented pyrolytic graphite (HOPG, 12 mm × 12 mm, 2 mm thick, ZYB grade) was from Bruker AFM Probes (Camarillo, CA, USA). The PeakForce SECM standard test sample design consists of mesh pattern with 1 µm wide Pt strands separated by Si_3N_4 islands. The thickness of Si_3N_4 islands is ~ 40 nm. To fabricate the patterned structure, a thin Pt layer was first deposited on the sample substrate followed by a thin Si_3N_4 film. The Si_3N_4 layer was then selectively patterned using contact lithography and HF etching to obtain the desired pattern.Au nanomesh electrodes were fabricated as described by Stelling *et al.*[34] and monolayers of polystyrene particles were prepared according to the procedure reported by Retsch *et al.*[35] On cationically functionalized glass slides a 3 wt % dispersion of the particles (diameter = 1.0 ± 0.04 µm, Microparticles GmbH, Berlin, Germany) in MilliQ water were spin cast. Upon slow immersion of the particle-coated substrates into a 0.1 mM SDS solution in MilliQ water, freely floating particle monolayers were formed at the air/liquid interface. The monolayers were transferred to glass substrates and dried in air.

The dry monolayer was etched for 20 min in a MiniFlecto plasma reactor (Plasma Technology GmbH, Herrenberg, Germany) with 75 % Ar and 25 % O_2 at 80 W and a pressure of 0.14 mbar in order to obtain non-close packed particle arrays. Cr (3 nm) and Au (50 nm) were deposited using a Balzers BA360 thermal evaporation chamber. The layer thickness was monitored via a SQM 160 microbalance (Sigma Instruments, Schaefer Technologie GmbH, Langen Germany). Subsequently, the particles were mechanically stripped off using Scotch® tape (3M) giving the nanomesh electrode. The electrodes were cleaned by ultrasonication in 2 % aqueous Hellmanex (Hellma GmbH, Mühlheim, Germany) solution for 10 min, rinsed with MilliQ water and sonicated in ethanol for 10 min.

Methods

Probe fabrication. The nanoelectrode probes were batch-fabricated through microelectromechanical systems (MEMS) processing techniques follow a Bruker proprietary protocol. Figure 3.1a shows the front side of the unmounted nanoelectrode probe with the square patch for adding electrical contact and the conductive line on the probe. This nanoelectrode probe was encapsulated behind glass and sealed with proprietary chemically resistive epoxy after electrical connection (Figure 3.1b).

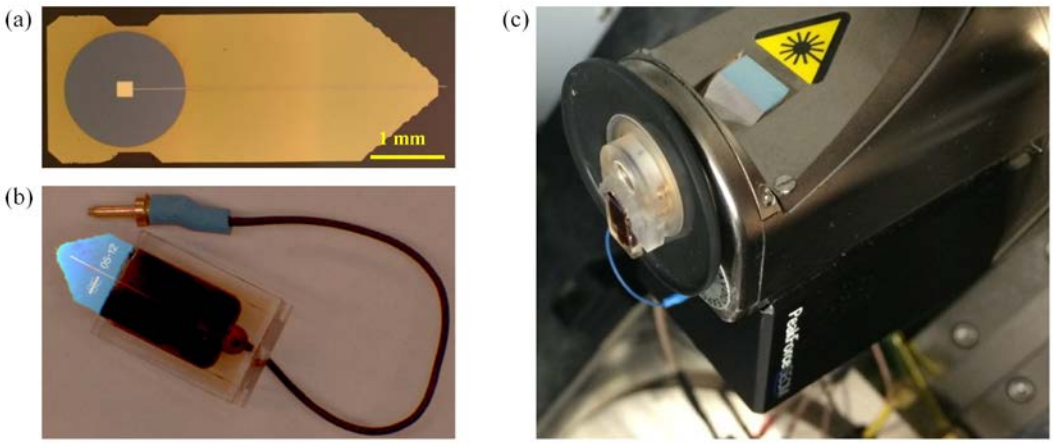

Figure 3.1. (a) Optical image of the unmounted probe; (b) Mounted probe; (c) PeakForce SECM key components (probe, probe holder, protective boot, and strain-released module) attached to the AFM scanner.

Chemical compatibility. Materials (glass and epoxy) for assembling the probe were tested for chemical compatibility. A piece of the material sample was weighed and the mass was recorded. Then, it was transferred to a jar and fully immersed in the solvent/solution of interest for 124 hours. After immersion, the sample was removed from the solvent/solution, cleaned, dried and re-weighed. The masses before and after the immersion were compared.

Electrochemical performance. Prior to the PeakForce SECM measurement, all probes were tested by performing three cyclic voltammograms (CVs, 20 mV/s, 0 to -0.5 V vs Ag/AgCl) in 5 mM $[Ru(NH_3)_6]Cl_3$ with 0.1 M KNO_3 using a Pt counter electrode and a Ag/AgCl reference electrode (CHI111, CH Instrument). A bi-potentiostat (CHI760D, CH Instrument, Texas, USA) was used.

Simulation. The transport of charged species in the solution electrolyte was modelled using the Nernst-Planck equation (Eq. 1)

$$J_i = -D_i \nabla c_i - u_{m,i} c_i \nabla \phi + \bar{v} c_i \tag{1}$$

where J_i is the flux of species i, c_i is the concentration of species i, $\bar{v}c_i$ is the convection term (which was negligible in this work because of the close spacing between the tip and sample), $\nabla\phi$ is the electrolyte potential gradient within the solution, D_i is the diffusion coefficient of the species i in the specified domain. $u_{m,i}$ is the mobility and defined in the Nernst-Einstein relation

$$u_{m,i} = \frac{z_i F D_i}{RT} \tag{2}$$

with z_i charge number of the species i, R as the gas constant, F Faraday's constant and T is the temperature.

The redox reactions involved fast outer-sphere electron-transfer reactions, hence, the model assumed no kinetic limitation on the redox reaction at the electrode surface. The rate constants for the redox reactions at the electrode surfaces were selected so that the electrode response was Nernstian. The only overpotential at the electrode/electrolyte interface in the system was the concentration overpotential, which is defined as the following:

$$\eta = 2.303\frac{RT}{F}\left(Log_{10}[\frac{c_R}{c_{R0}}] - Log_{10}[\frac{c_O}{c_{O0}}]\right) \quad (3)$$

where c_R and c_O are the respective reduced and oxidized species concentrations at the interface, c_{R0} and c_{O0} are the corresponding equilibrium (i.e. bulk) concentrations of the indicated species, *F* is Faraday's constant, *R* is the gas constant, and *T* is the absolute temperature. The overpotential at the electrode/electrolyte interface was also defined as:

$$\eta = \phi_s - \phi_l - \phi_0 \quad (4)$$

where ϕ_s and ϕ_l are the electric and electrolyte potential at the electrode-electrolyte interface, respectively, and ϕ_0 is the equilibrium potential. The equilibrium potential was set to be zero for simplicity. Additional voltage losses in the system including the ohmic resistive loss and electrodialysis loss in the electrolyte were captured in electrolyte potential term, ϕ_l. Conservation of charge and continuity of current density were stipulated at the electrode/catalyst interface.

Figure 3.2 illustrates the boundary conditions in the simulation. Constant potentials were applied at the tip (blue) and the sample (green) electrodes. Insulation conditions (black) were applied at the top of the simulation region and at the insulation ring in the sample electrode. The species concentrations at the vertical side of the simulation domain (red) were fixed as initial concentrations.

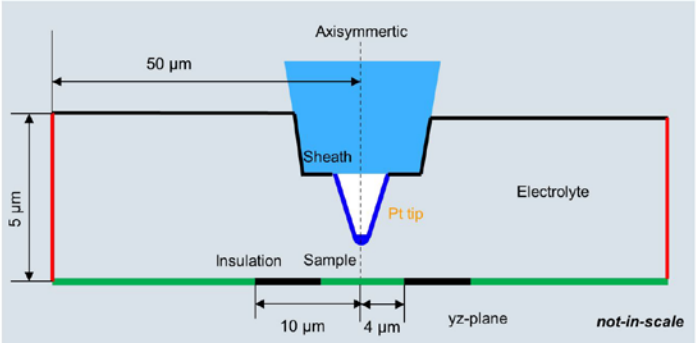

Symmetry	Axisymmetric
Nearly cylinder domain with the radius	50 µm
Pt tip	Cone
Pt tip apex	Hemisphere
Pt tip height	215 nm
End tip radius	25 nm
Base tip cone radius	175 nm
Sheath radius	390 nm
Inner/Outer radius of the insulation ring	4 µm / 10 µm
Tip reaction	$[Ru(NH_3)_6]^{3+} + e \rightarrow [Ru(NH_3)_6]^{2+}$
Sample reaction	$[Ru(NH_3)_6]^{2+} - e \rightarrow [Ru(NH_3)_6]^{3+}$

Figure 3.2. SECM experimental setup. A potential difference was applied between the tip (dark blue) and the sample (green) electrodes. The relationship between the tip/sample current density and their corresponding overpotential are fitted into exponential forms to capture fast reactions (details in the text).

A finite-element solver, COMSOL Multiphysics, was applied to solve the coupled governing equations and the corresponding boundary conditions for steady-state operation. Quadratic element discretization and standard solvers were chosen. A relative tolerance of the corresponding variable of 10^{-3} was used as convergence criteria.[36]

PeakForce scanning electrochemical microscopy. PeakForce SECM was operated on a Dimension FastScan/ICON AFM (Bruker, USA), which combines PeakForce tapping (PFT) imaging mode with the AFM-SECM approach. We have previously described the setup used.[32] The pre-mounted nanoelectrode probe was loaded onto a SECM probe holder and a Kalrez® electrometric boot was placed in the grooved cutout on the bottom of the holder to help seal the cell, minimizing evaporation and preventing liquids from contacting the AFM scanner (Figure 3.1). This assembly of probe, holder, and boot was mounted to the scanner and the cable of the nanoelectrode probe was connected to a strain-released module. This module has built-in electronics with resistance selectors (0, 1 and 10 MΩ) to limit the maximum current flow. It is also useful to avoid direct electrical connection to the probe, which generally causes mechanical noise in the AFM images. In this work, a 10 MΩ current-limiting resistor was selected. All the electrical leads of the electrodes were routed to a spring block connection hub. To minimize the 60 Hz noise from the power line, all cables were co-axially shielded and all electrical grounds were common to the bipotentiostat (CHI760D, CH Instrument, Texas, USA) that was used for controlling the electrochemical conditions. A Bruker EC-AFM cell[37] was used for PeakForce SECM imaging. In this cell, a Pt wire loop along the internal perimeter of the cell was used as a counter electrode and a AgCl-coated Ag wire was used as a pseudo-reference electrode (AgQRE). In the characterization of the nanomesh electrode, a true Ag/AgCl reference electrode was used. A 5 or 10 mM aq. $[Ru(NH_3)_6]Cl_3$ was used for redox reactions. Supporting electrolytes were either 0.1 M KCl or 0.1 M KNO_3. During PeakForce SECM imaging, the bipotentiostat performed amperometric measurements at 1 nA/V current-to-voltage (i/E) conversion sensitivity and the filter setting for this i/E converter is 32 Hz. The reduction of $[Ru(NH_3)_6]^{3+}$ was performed at -0.5 V vs. AgQRE or -0.4 V vs. Ag/AgCl while the oxidation of the generated $[Ru(NH_3)_6]^{2+}$ was at 0 V vs. AgQRE or -0.1 V vs Ag/AgCl. The reduction

reaction was carried out either by the tip or the sample, while the tip current is of interest and analyzed.

For imaging, PFT has been widely adopted as an advanced, while simple-to-implement, AFM imaging mode in many applications.[33,38-45] During PeakForce imaging, the AFM probe is sinusoidally modulated at a low frequency that is off-resonance from the cantilever oscillation. In this work, 2 kHz with tapping amplitudes of 100 or 150 nm were used. The feedback set point is the maximum tip-sample contact force during every tapping cycle. Therefore, PFT performs triggered force curves during imaging. Through the analysis of these curves in real-time, quantitative nanomechanical properties can be extracted. Detailed description and other advantages of PFT can be found in the literature.[33]

PeakForce SECM imaging scans the nanoelectrode probe with the interleaved patterns as shown in Figure 3.3a and 3.3b. The probe movement follows a raster scanning pattern with a fast and a slow scan direction. The tip continuously moves in the slow scan following the upward or downward direction. In this mode, after the trace and retrace of each main scan line (in which topography is typically measured), a second trace and retrace is inserted to obtain non-topographical information. During the lift scan, the probe follows the stored topographic profile captured from the main scan while at a user-defined lift height. In the main scan of PeakForce SECM, PFT captures AFM information, such as topography, mechanics and electrical conductivity, while electrochemical activities are characterized in the lift scan. In this work, only the retrace scans of all channels were captured. The drift is <0.01 nm/s and is not a concern for the lift-scan measurements reported here.

It is noted that the AFM electrochemical cell used in this work is not fully sealed or airtight. As the AFM-SECM experiment normally took more than 30 min, we did not degas the electrolyte solution to remove O_2 before use. The dissolved oxygen may contribute ~5-10% current signals as discussed in Appendix A.

Due to the filter setting of the i/E converter (32 Hz), the amperometric measurement averaged ~30 ms of the data stream for each data point, and thus, the bipotentiostat captured the tip current averaged over ~60 PFT cycles. The tip also intermittently contacted with the surface for ~80 or ~70 μs on every tapping cycle for tapping

amplitude of 100 or 150 nm, respectively. This enables the measurement of the contact current. However, it is tapping-cycle-averaged due to the slow data acquisition of the bipotentiostat. The tip current was then routed to the AFM controller and processed into a map.

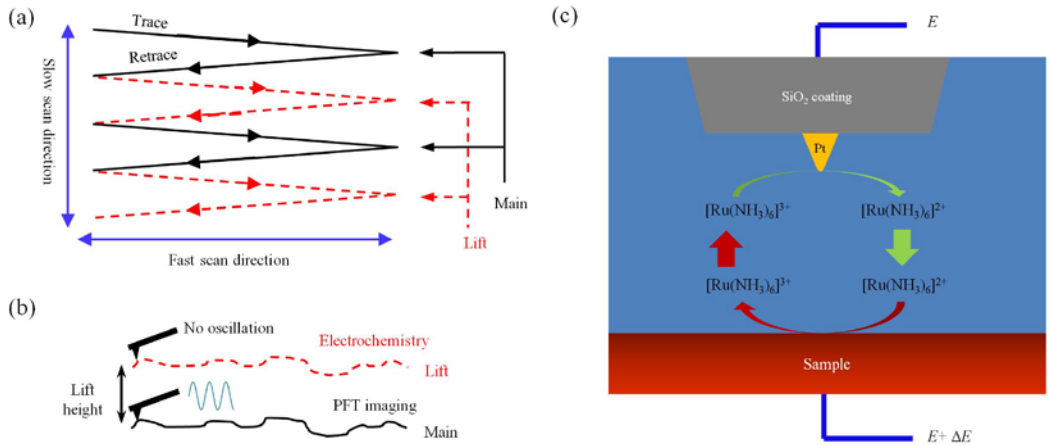

Figure 3.3. (a) Pattern of the probe movement in the interleaved scan mode. (b) Illustration of the interleaved scan mode. In the main scan, AFM performs PFT imaging. In the lift scan, the tip stops the PFT sinusoidal oscillation but follows the surface topography at a defined lift height for electrochemical imaging. (c) SECM feedback mode.

PeakForce Tunneling AFM (PF-TUNA) in liquid. The nanoelectrode probe is connected to the PF-TUNA module attached to the scanner. The mesh electrode sample was placed in the electrochemistry cell and biased while the tip remained grounded. Conductivity measurements were collected in a dimethyl carbonate solvent inside an Ar-filled glovebox with < 1 ppm O_2 and H_2O content. PF-TUNA was also demonstrated for a HOPG sample in air. The HOPG was conductively connected to the chuck of the AFM stage and a drop of deionized water was added to the sample surface and the sample was biased via the stage.

The algorithm of the Nanoscope software captured currents at the maximum contact force (peak current), averaged over the contact duration (contact current), and averaged over the whole tapping cycle (TUNA current).[44] We also conducted local current-voltage (*I*-*V*) spectroscopic measurement using the point-and-shoot function of the software. This

function enabled us to pinpoint spots of interest on the captured AFM images for measuring the *I-V* characteristics.[32]

Results

Probe fabrication. Figure 3.4a shows a side view of the rectangular cantilever, whose typical dimension is 225 μm × 25 μm × 3.2 μm. Typical spring constants and resonant frequencies were 1.5 N/m and 69 kHz, respectively. The tip height is typically 12 μm. The top view of the cantilever in Figure 3.4b shows a conductive path of 11 μm width. Figure 3.4c shows the exposed Pt coated conical tip apex with typically 25 nm radius and 250 nm tip height. The thickness of the Pt coating layer is 50 nm. Other than this tip apex, the probe is fully isolated with SiO_2 and other dielectric sub-layers. The base of the exposed conical Pt-coated electrode has a typical radius of 125 nm and the sheath near this base is 350 nm in radius. This results in a ratio of the radius of the insulating sheath to the electrode radius, R_G, of typically 2.8 at the base.

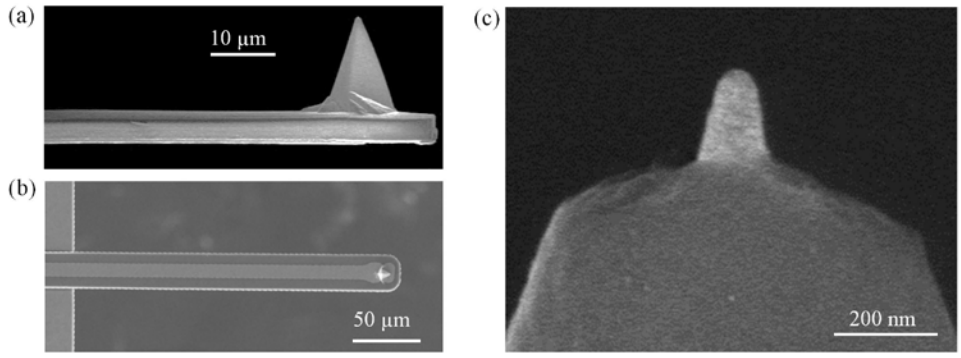

Figure 3.4. SEM images of the nanoelectrode probe. (a) Side view of the cantilever. (b) Top view of the cantilever showing the 11 μm-width Pt conductive path. (c) The exposed Pt coated tip apex with ~50 nm end-tip diameter and ~200 nm tip height. Other than the tip apex, the probe is fully isolated with SiO_2 and other dielectric sub-layers.

Components (glass and epoxy) used for mounting the nanoelectrode probes have been tested for chemical compatibility in a variety of liquid environments, including aq. 0.1 M NaOH, KOH, HCl, H_2SO_4, HNO_3 and H_2O_2, and organic solvents of diethyl carbonate, dimethyl carbonate, ethyl acetate, ethyl methyl carbonate, 1-methyle 1-2-pyrroliodone, toluene acetonitrile, methanol, ethanol, and acetone. The tests show less than 1.0 % change in mass over 124 h of immersion. Immersion in a solution of 1 M $LiPF_6$ in the

mixture of ethylene carbonate : dimethyl carbonate (1:1 in volume) shows a mass increase of 1.0 %. Control experiments performed by measuring the same piece of the materials without any treatment shows a mass measurement accuracy of ± 0.4 %.

Simulation. COMSOL simulation was performed on a probe with typical dimensions and an idealized symmetric geometry. The end tip was treated as a hemisphere while the sheath at the base of a perfect tip cone was assumed to be flat (Figure 3.2). The three-dimensional concentration profile of $[Ru(NH_3)_6]^{3+}$ (10 mM in the bulk with 0.1 M KCl supporting electrolyte) near the tip on both insulative and conductive substrates at different tip-sample distances were simulated at different applied potentials until a limiting current density was reached. For simulations with a conductive substrate, a typical SECM feedback mode is used as illustrated in Figure 3.3c; the tip was biased at a potential suitable to drive the reduction reaction, while the substrate was biased to drive oxidation and redox-couple regeneration. When the probe was far away (1 mm) from an insulating substrate (Figure 3.5a), a limiting current of 718 pA was calculated. At the limiting current condition, the concentration profile for the $[Ru(NH_3)_6]^{3+}$ as a function of the distance from the electrode surface is shown in Figure 3.5b. A rapid rise in the $[Ru(NH_3)_6]^{3+}$ concentration from 0 to 6.4 mM within 100 nm of the tip distance was observed. The simulated concentration profile was fit to an analytical expression derived for a planar ultramicroelectrode (UME) under the approximation of semi-infinite spherical diffusion,[46]

$$C_d = C_0\left(1-\frac{r_0}{d+r_0}\right) \tag{5}$$

C_d is the surface concentration at tip-sample distance d following the central axis; C_0 is the bulk concentration, which is 10 mM; and r_0 is the apparent radius. The fitting yielded an r_0 of 57 nm which was 2.3 times of the end-tip radius.

Figure 3.5c shows the concentration profile when the tip was 10 nm away from an insulating surface. The resulting tip current decreased from 718 to 434 pA as the distance to the surface was reduced from 1 mm at 10 nm. While on a conducting substrate biased so the system is in positive feedback mode (as shown in Figure 3.5d), the tip current increased from 748 to 1193 pA as the distance decreased from 1 μm to 10 nm, in 9.9 mM

$[Ru(NH_3)_6]^{3+}$ / 0.1 mM $[Ru(NH_3)_6]^{2+}$ and 0.1 M KCl. The 0.1 mM $[Ru(NH_3)_6]^{2+}$ was included to improve the convergence of the simulation.

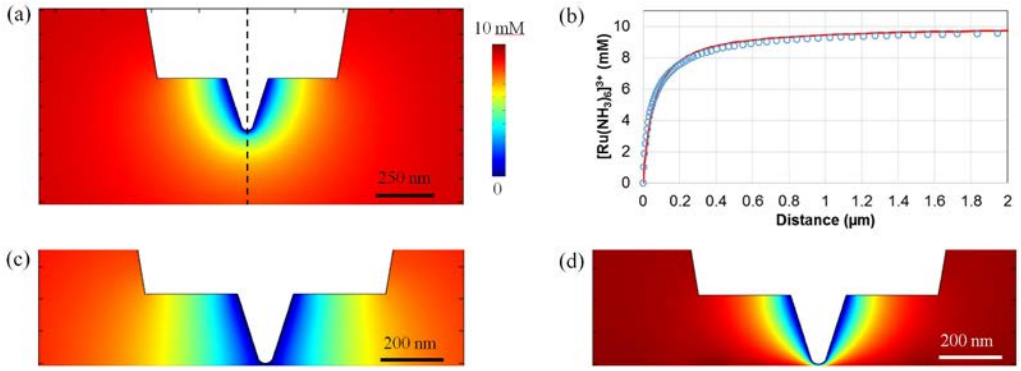

Figure 3.5. COMSOL simulation of the $[Ru(NH_3)_6]^{3+}$ concentration profile near the nanoelectrode probe. (a) The probe is 1 mm away from an insulating substrate. (b) Concentration profile from the electrode surface following the center axis as indicated in (a). Symbols are the simulated results. Red solid line is a fit to Equation 5 in the text. (c) and (d) The probe is 10 nm away from an insulating substrate and an conducting substrate, respectively. Conditions: 10 mM $[Ru(NH_3)_6]^{3+}$ in the bulk; 0.1 M KCl supporting electrolyte.

Electrochemical performance. Figure 3.6a shows representative results of a SECM nanoelectrode probe from continuous electrochemical tests in 5 mM $[Ru(NH_3)_6]^{3+}$ and 0.1 M KNO_3. The first measurement was a 3 h amperometric experiment at -0.36 V vs Ag/AgCl. The diffusion-limited tip current (~430 pA) for the first 20 min (inset of Figure 3.6a) showed no decrease of tip current with time. Diffusion-limited currents among over 100 different probes are 375 ± 225 pA, corresponding to probes with different exposed active tip heights (of 250 ± 100 nm). The probe was cleaned and dried after the amperometric measurement and tested in a freshly-prepared solution; one CV scan (20 mV/s) is shown in Figure 3.6a as the sigmoidal blue dotted line. At potentials from 0 to -0.05 V, the reduction of $[Ru(NH_3)_6]^{3+}$ is negligible and the background capacitive current is ~ 5 pA. The reduction current starts increasing at ~ -0.1 V and reaches the plateau of ~420 pA at ~-0.2 V vs. Ag/AgCl. After this one CV scan, the probe was cleaned and dried for the third test of 100 CV cycles. The black-solid plot shows the 40^{th} cycle in this test. The probe, after cleaning and drying as before, was further tested in a freshly-prepared solution by collecting another CV scan as shown by the red dashed line. The

similarity of the three CV curves collected indicates insignificant performance degradation of the tip.

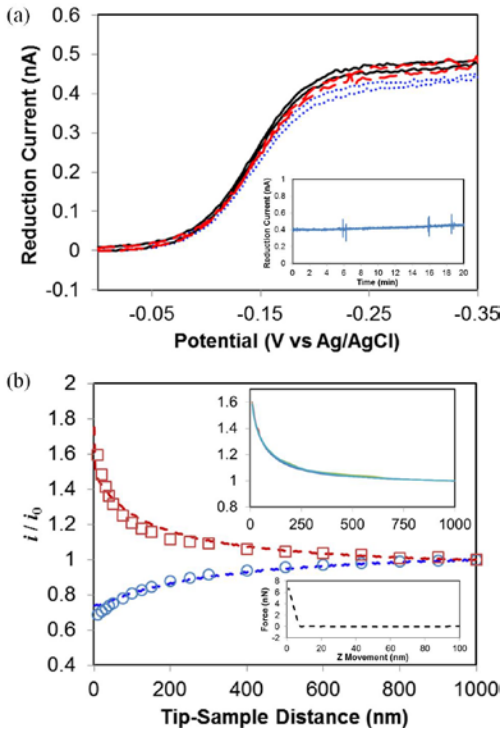

Figure 3.6. (a) Representative results from continuous electrochemical tests in 5 mM $[Ru(NH_3)_6]^{3+}$ and 0.1 M KNO_3. For cyclic voltammetry (CV), the scan rate was 20 mV/s. The first measurement was a 3 h amperometry test (-0.36 V vs Ag/AgCl). The inset shows the tip current of the first 20 min. The probe was cleaned and dried for the second test of one CV scan (blue dotted line). The third test after the probe was cleaned and dried included 100 CV cycles. The black-solid plot was the 40th cycle of this test. The probe was cleaned and dried again for the last test of one CV scan (red dashed line). (b) Approach curves of nanoelectrode probe on a Pt (red dashed) and a Si_3N_4 (blue dashed) surface. The tip and the substrate were biased at 0 and -0.5 V vs AgQRE, respectively. The solution was 10 mM $[Ru(NH_3)_6]^{3+}$ with 0.1 M KCl supporting electrolyte. Symbol plots are COMSOL simulation results. Conditions for open circles are 10 mM $[Ru(NH_3)_6]^{3+}$ with 0.1 M KCl on an insulating surface. For open squares, they are 9.9 mM $[Ru(NH_3)_6]^{3+}$ / 0.1 mM $[Ru(NH_3)_6]^{2+}$ and 0.1 M KCl on a conductive surface. The top inset shows simulation results based on $[Ru(NH_3)_6]^{3+}$/$[Ru(NH_3)_6]^{2+}$ combinations of 9.9/0.1, 9.9/0.5, 9/1, 7/3 and 5 mM / 5 mM. The bottom inset shows the force ramping for capturing the approach curves.

Approach curves (dashed lines) shown in Figure 3.6b recorded the tip current as it approaches the sample surface, which were captured through moving the nanoelectrode in the Z direction until it reached a defined force (7 nN in this work). The current on the plots are normalized to i_0, defined as the current measured for a tip-sample distance of 1

μm. The tip and sample were biased at -0.5 V and 0 V vs. AgQRE, respectively, in 10 mM $[Ru(NH_3)_6]^{3+}$ and 0.1 M KCl. On a Pt surface (red dashed), the tip current was enhanced by ~40% when it was close to the surface. At < 7 nm, the tip was in contact with the surface and an abrupt increase in current was observed. While for an insulating nitride surface (blue dashed line), the faradaic current decreased by ~25% as the tip approached the sample surface. When the tip was in contact with the surface at < 7 nm, the faradaic current did not change. The bottom inset on Figure 3.6b shows the force ramping for the approach curve and illustrates the 7 nN contact force and that the tip was in contact with the surface at ~7 nm. The tip current changed most quickly when the tip was within ≤ 100 nm of the surface. These results are consistent with COMSOL simulation as shown by the symbols in Figure 3.6b. Simulation conditions for negative feedback (open circles) were 10 mM $[Ru(NH_3)_6]^{3+}$ with 0.1 M KCl on an insulating surface. For positive feedback (open squares), they were 9.9 mM $[Ru(NH_3)_6]^{3+}$ / 0.1 mM $[Ru(NH_3)_6]^{2+}$ and 0.1 M KCl on a conductive surface. The presence of 0.1 mM $[Ru(NH_3)_6]^{2+}$ assisted the convergence of the simulation. To check the effects of the of $[Ru(NH_3)_6]^{2+}$ on the simulation, we performed simulations with $[Ru(NH_3)_6]^{3+}$/$[Ru(NH_3)_6]^{2+}$ combinations of 9.9/0.1, 9.9/0.5, 9/1, 7/3, and 5/5 mM/mM. The results are shown on the top inset of Figure 3.6b. These results normalized at 1 μm have standard deviations < 1% at each tip-sample distance point. Therefore, all these curves visibly overlap and the addition of small amounts of $[Ru(NH_3)_6]^{2+}$ in the simulation data does not affect the predicted response.

PeakForce SECM imaging. A sample with a mesh pattern of 1 μm wide Pt strands separated by 2 μm × 2 μm square Si_3N_4 islands, as shown in Figure 3.7a, was tested using PeakForce SECM in 10 mM $[Ru(NH_3)_6]^{3+}$ and 0.1 M KCl. The scan was completed in the interleaved scan mode (Figure 3.3a and 3.3b) so that morphology and electrical/mechanical properties where measured in the first (main) line scan while SECM response was measured in the second (lift). The tip voltage was -0.5 V vs AgQRE for reducing $[Ru(NH_3)_6]^{3+}$. The sample potential was 0 V vs AgQRE for oxidation of the tip-generated $[Ru(NH_3)_6]^{2+}$ that diffused to the sample surface. The positive feedback of this $[Ru(NH_3)_6]^{3+}$ regeneration from the sample surface leads to the enhancement of tip current.

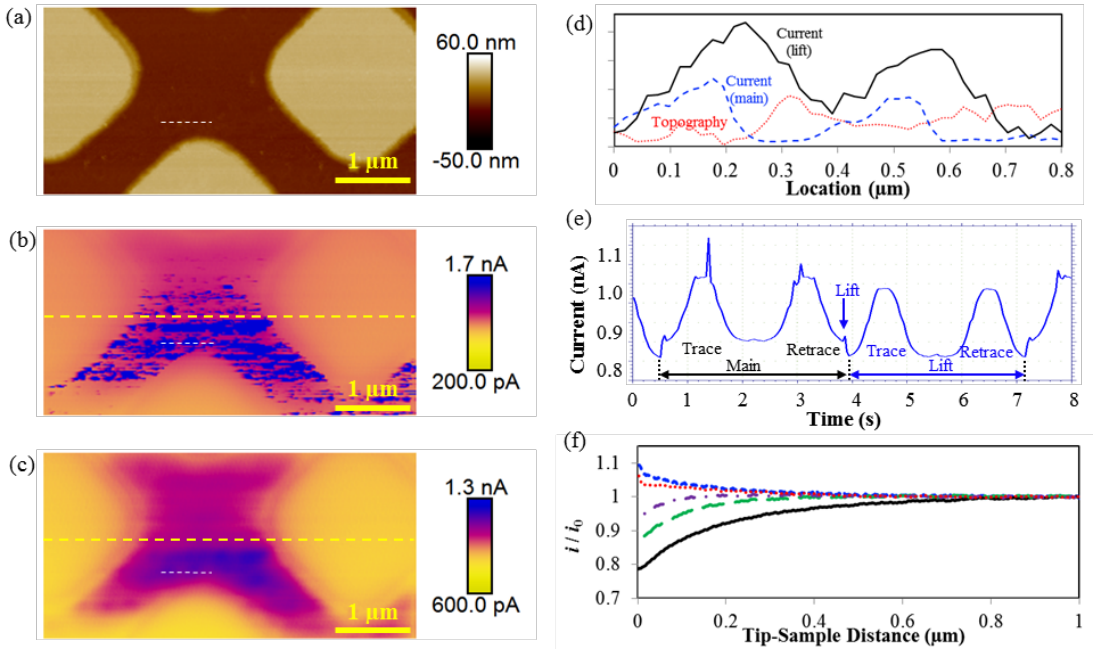

Figure 3.7. PeakForce SECM images of a mesh pattern with 1 µm wide Pt strands separated by 2 µm × 2 µm square Si_3N_4 islands. (a) Surface topography. (b) Tip current during the main PeakForce tapping scan. (c) Tip current captured from the lift scan at a lift height of 100 nm. (d) Line-scan analysis of topography (red dotted line, variation of 3.4 nm), tip current from main scan (blue dashed line, variation of 5.5 nA), and tip current from lift scan (solid black, variation of 28 pA) at scan lines indicated by the white dashed line on (a)-(c). (e) Screen shot of real time tip current captured by potentiostat software during line scans indicated by the yellow dashed lines on (b) and (c). (f) Approach curves captured from locations of different activities are compared. All these plots are normalized to the current at a lift height of 1 µm. The black solid curve was captured on the nitride square. Others were captured on the Pt regions of various electrical conductivity. Solution: 10 mM $[Ru(NH_3)_6]^{3+}$ and 0.1 M KCl. Tip and sample potentials: -0.5 and 0 V vs. AgQRE, respectively.

In the main scan, regular PeakForce imaging was performed. Figure 3.7a is the topographic map showing the strand pattern with a depth of 40 nm. When fabricating this sample, the incomplete etching of the Si_3N_4 resulted in limited exposed areas of the Pt substrate in the Pt strand areas. Figure 3.7b shows the tip electrical current captured during the main scan of the PeakForce SECM imaging due to direct contact conduction between the metal tip and the substrate. The current on the nitride surface was ~0.85 nA. On the Pt region the current was highly variable, ranging from ~ 1 to 10 nA (i.e. hitting the limiting current for the range selected). These high currents resulted from direct

contact between the metal-tip and Pt-sample that occurs in regions where the nitride is completely etched.

For electrochemical scanning, the tip was lifted at 100 nm while following the surface topography that was captured in the main line scan (Figure 3.3a and 3.3b). Figure 3.7c shows the non-contact tip faradic current captured during the lift scan, which clearly differentiates the Pt surface from the nitride regions. When the tip scanned over the nitride squares, the current is ~ 0.8 nA. While over the Pt strands, the tip current increased by ~ 50 to ~350 pA. The electrochemical tip current enhancement was inhomogeneous over the Pt region. Large electrochemical currents are correlated with the locations of tip conduction current captured in the main scan. Comparing Figure 3.7c with 7b, spots that have higher density of electrical current spikes were also more active in electrochemistry. Spots of highest faradaic currents are located near the center of the image as shown by the blue areas that exhibit fine features with100 ~ 200 nm spatial extent.

In Figure 3.7d we compare the line profiles at the same locations indicated by the white dashed lines on Figure 3.7a-7c. The surface profile (red dotted) shows featureless variation with a range of 3.4 nm and a standard deviation of 0.7 nm. The tip current from the main scan (blue dashed) showed two peaks at locations of ~0.2 μm and ~0.5 μm. The HWHMs (half widths at half maximum) of these two peaks are ~75 nm. These are consistent with the two spots of high currents that the white dashed line crosses. The variation of the tip current for this line profile is from 1.2 to 5.5 nA. The high current results from the tip-sample contact during PFT imaging. The two areas of different conductive (and thus electrochemically active) properties were also resolved by the non-contact tip faradaic current from the lift scan (black solid), which shows two peaks at ~0.25 and ~0.6 μm, respectively.

Figure 3.7e shows a screen shot of the real-time tip current acquisition by the bipotentiostat. This current-time plot includes current signals from the retrace scan line indicated by the yellow dashed line in Figure 3.7b and 3.7c. Figure 3.7e shows tip currents from tip lifting, main and lift scans, and trace and retrace scans. First, symmetrical current profiles are observed between trace and retrace scanning. Second, the tapping-cycle-averaged tip current from the main scan (tapping amplitude, 150 nm)

was ~40 pA higher than the corresponding one in the lift scan when the oscillation was disabled and the tip is 100 nm away from the surface. Third, current spikes are shown on the section from the main scan due to direct electrical conduction.

Approach curves captured from locations of different electrochemical activities are compared in Figure 3.7f. These plots are normalized to the current at a tip lift height of 1 µm. The black curve was captured on the nitride square, which shows a 22% reduction of tip current at the nitride surface compared to at a lift height of 1 µm. Other approach curves captured on the Pt region show a variety of approach curve behaviors depending on the conductivity of the Pt region.

Figure 3.8 shows a second example of PeakForce SECM imaging in 5 mM $[Ru(NH_3)_6]^{3+}$ and 0.1 KNO_3. Nanosphere lithography was used to prepare an Au thin film electrode on SiO_2 patterned with 0.75 µm diameter holes spaced 1 µm on center. The smallest dimension of the resulting Au grid on the electrode surface was thus ~250 nm. The depth of these holes was 80 nm (Figure 3.8a). The thermal evaporation process led to "in-hole" fine features from shadow effects during metal deposition. Therefore, the flat bottom, which is the exposed SiO_2 substrate, was an elliptical area of about 500 nm × 400 nm. The Au nanomesh electrode was biased at -0.4 V vs Ag/AgCl to generate $[Ru(NH_3)_6]^{2+}$ while the probe was biased at -0.1 V vs Ag/AgCl to regenerate $[Ru(NH_3)_6]^{3+}$. Figure 3.8b depicts the tip current captured during the lift scan at a lift height of 75 nm, which shows increased current over the Au area. Thereby, one can clearly differentiate between the Au and SiO_2 regions. The yellow dashed line on Figure 3.8a and 3.8b indicate the same line location for cross-sectional analysis as shown in Figure 3.8c. The topographic profile (black dotted line, Figure 3.8c) shows a feature with a width of 155 nm at HWHM resulting from the Au grid. Because the Au surface enhanced the tip current, the electrochemical profile also shows a feature whose HWHM is 241 nm. The resolution of the SECM measurement can be assessed by comparing the sharpness of the physical height profile to that of the SECM profile. The left shoulders show that 75% of the variation in signal occurs over distance of ~120 nm and ~180 nm for topography and tip current, respectively. These comparisons show that the electrochemical profile tracks the topographic variation. The broadening of the SECM current was consistent with diffusion of the generated product to the lift height of 75 nm.

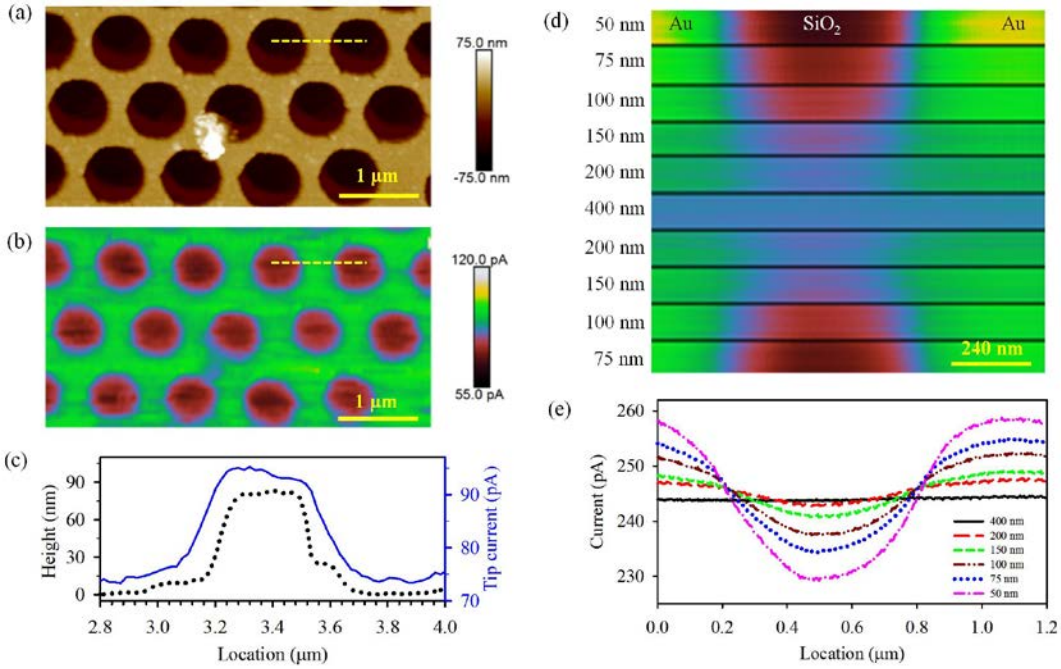

Figure 3.8. PeakForce SECM imaging of an Au nanomesh electrode in 5 mM $[Ru(NH_3)_6]^{3+}$ and 0.1 M KNO_3. (a) Surface topography shows a hole pattern of 0.75 µm × 1 µm (diameter x spacing). (b) Tip current captured from the lift scan at a lift height of 75 nm. (c) Cross-sectional analysis of topography (black dotted) and tip current from lift scan (solid blue) at locations indicated by the yellow dashed line on (a) and (b). (d) Tip current at sequentially varied lift height (as indicated on the left of the image). The slow scan direction was disabled so to the tip scanned the same line profile over a hole feature for all the measurements. (e) SECM current traces from panel (d). The tip and sample potential were -0.1 and -0.4 V vs Ag/AgCl, respectively.

Figure 3.8d shows the SECM tip current profile over a single SiO_2 hole in the Au nanomesh as the lift height was changed between 50, 75, 100, 150, 200, 400, 200, 150, 100, and 75 nm. The slow scan direction was disabled to ensure the nanoelectrode tip scanned the same line for each height. The resulting current line scans obtained from the image are shown in Figure 3.8e. As the lift height increased, the tip current decreased on the two Au regions and increased on the SiO_2 surface. These two-dimensional electrochemical maps show that the three surface regions were clearly spatially resolved at a tip lift height of 50 nm, while the current contrast was largely lost at a lift height of 200 nm. At a tip-sample distance of 400 nm, the variation of the current was negligible.

Conductivity measurement in liquid. Figure 3.9 shows an example of conductivity measurements in dimethyl carbonate, performed in an Ar-filled glovebox with < 1 ppm O_2 and H_2O content. Here, the mesh electrode described above was employed. The PF-

TUNA module was used and the tip remained grounded while a bias of 10 mV was applied to the sample. Figure 3.9a is a topographic map showing nitride islands at four corners and residual nitride on the Pt surface. The conductivity map shown in Figure 3.9b resolved the exposed Pt region. These current signals were captured by averaging the data collected over the ~ 70 µs tip-sample contact at every tapping cycle. This differs from the tapping-cycle-averaged contact current captured by the bipotentiostat in PeakForce SECM. On the Pt region the current was highly variable, ranging from 7.5 pA to 5 nA (which is the saturation current at the 1 nA/V gain setting selected). PeakForce TUNA is also capable of point-and-shoot measurement to pinpoint areas of interest for current-voltage (*I-V*) measurement, as shown in Figure 3.9c. The plots are labelled corresponding to the location (1, 2, and 3) indicated in Figure 3.9b. The measurements were collected using a ramp rate of 40 mV/s and repeated five times at each location, while maintaining the constant tip-sample contact at a force of 20 nN. *I-V* curve 1 captured from the Pt region exhibited a strong current response and quickly reached ~5 nA at ~5 mV. *I-V* curve 2 captured from a spot shows less current, reaching the saturation currents at ~10 mV. *I-V* curve 3 was captured from a nitride region where only a capacitive current of ~ 5 pA is measured.

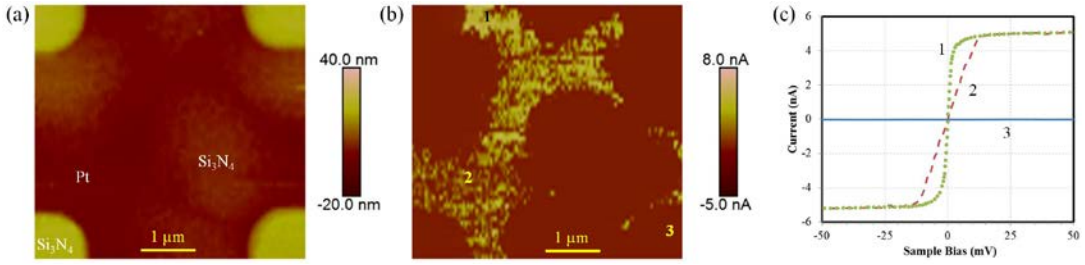

Figure 3.9. PeakForce TUNA measurement of a Pt surface partially covered by Si_3N_4 in dimethyl carbonate solvent. (a) Topography image. (b) TUNA currents at a sample bias of 10 mV. (c) Point-and-shoot *I-V* spectroscopy at specified locations in (b). This measurement was performed in an Ar-filled glove box with < 1 ppm O_2 and H_2O content. The plateau on plot #1 and #2 are the saturation current at the 1 nA/V i/E converter sensitivity setting.

Multimodal imaging of highly ordered pyrolytic graphite (HOPG). Figure 3.10 is an example of PeakForce SECM on an HOPG electrode in 10 mM $[Ru(NH_3)_6]^{3+}$ and 0.1 M KCl. This measurement was carried out using a SECM feedback mode, where the tip

voltage was -0.5 V vs AgQRE for reducing $[Ru(NH_3)_6]^{3+}$ and the sample potential was 0 V vs AgQRE for oxidation of the tip-regenerated $[Ru(NH_3)_6]^{2+}$ that diffused to the sample surface. The surface topography on Figure 3.10a showed steps of 1 - 3 graphene layers, ~ 0.3 to 1 nm in height. A ~ 900 nm × 600 nm defective area on the HOPG surface is shown on the left. This defect region was 0.4 nm higher than the surrounding terrace. Figure 3.10b is a quantitative map of adhesion force, which was achieved through the real time analysis of the force curve captured from each tapping cycle. On the edge sites, the adhesion force was ~ 1 to 4 nN lower than the terraces resulting from both the different chemical properties and reduced tip-sample contact area. This quantitative mechanical map also differentiates the flat defective region, which was 3.1 nN less adhesive than the terraces. In addition to the difference in mechanics, this defect region presented a distinct electrochemical response as shown in Figure 3.10c. The faradic current was captured during the lift scan at a lift height of 75 nm. The defective area had a faradic current ~55 pA or 10 % less than the remainder of the sample. Figure 3.10c also shows SECM tip currents that were ~ 2 to 5 pA larger at the step edges relative to the rest of the non-defective region. Figure 3.10d shows the topographic (black dashed line, 0.4 nm step height) and electrochemical response (red solid line) for a line scan (indicated by the dashed line in Figures 3.10a and 3.10c) across the defective zone.

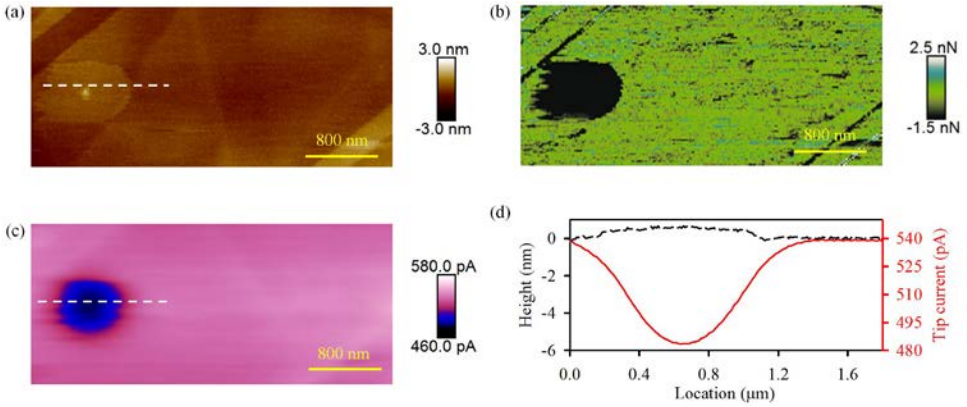

Figure 3.10. PeakForce SECM images of a HOPG sample. (a) Surface topography shows an elliptical defect region of approximately 900 nm × 600 nm. (b) Quantitative map of adhesion force, which was obtained through the real time analysis of the force curve captured from each tapping cycle. (c) Tip current captured from the lift scan at a lift height of 75 nm. (d) Cross-sectional analysis of topography (black dashed line) and tip current from lift scan (solid red line) at locations indicated by the white dashed line on (a) and (b). The sample and tip potential were 0 and -0.5 V vs AgQRE, respectively. The solution was 10 mM $[Ru(NH_3)_6]^{3+}$ and 0.1 M KCl.

Figure 3.11 shows PF-TUNA conductivity measurement of an HOPG sample in deionized water. Figure 3.11a is a high-resolution topographic map (584 nm × 227 nm) showing terraces, edges and flake sheets on the HOPG surface. Edges had step heights of 0.3 to 1.5 nm, accounting for one to five graphene layers. The flake in the middle of the image had a height variation from 0.6 to 5 nm. The corresponding electrical tip contact current image at a sample bias of 10 mV is shown in Figure 3.11b. On the terrace, the contact current was 15 to 25 nA, while edges site generally showed > 100 nA contact current. The most conductive region on the flake showed 300 to 500 nA contact current. In addition, a trench of ~10 nm width and 0.3 nm depth on the terrace to the left of the flake that was barely seen on the topography scan (Figure 3.11a) was clearly visible on the current map. The contact current from this trench was 150 to 250 nA. For a better comparison, profiles of both topography and contact current at the same location (as indicated by the black dash line in Figure 3.11a and 3.11b) are plotted together on Figure 3.11c. The terrace showed typical contact current of ~20 nA, while edges show an order of magnitude higher current although the step height of these edges was ~1 nm or less.

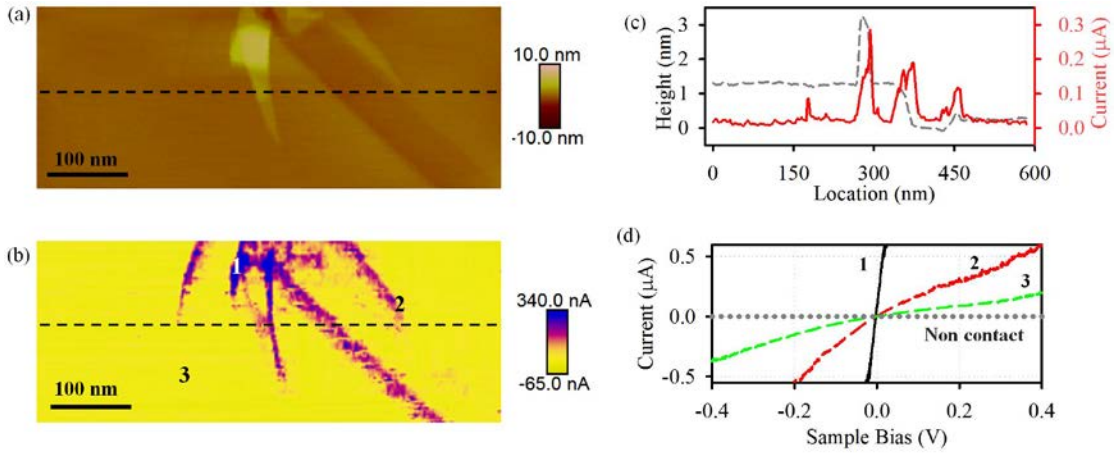

Figure 3.11. PeakForce TUNA on HOPG in deionized H_2O. (a) Topographic AFM image. (b) Corresponding contact currents for (a) with the HOPG biased to 0.1 V versus ground. (c) Line profiles of both the topographic height (grey dashed line) and contact current (red solid line) at the same location labeled by the black dashed lines in (a) and (b). (d) Current-voltage sweeps were performed on locations correspondingly labelled in (b). A background sweep (grey dotted line) when the tip is 1 mm away from the sample surface is also shown and labelled as "Non contact". The voltage sweep rate was 0.48 V/s.

Figure 3.11d shows plots from the *I-V* measurements labelled corresponding to the location (1, 2, and 3) indicated in Figure 3.11b. The measurements were performed at a ramp rate of 0.48 V/s. *I-V* curve 1 captured from on the flake region exhibited a strong current response at low applied potentials and quickly reached an instrument saturation current of ~550 nA at ~25 mV. *I-V* curve 2 captured from a step edge shows less current, -550 nA and 550 nA saturation currents at -0.2 V and 0.4 V, respectively. *I-V* curve 3 captured from a basal plane shows the smallest current, -360 and 200 nA at -0.4 and 0.4 V, respectively. The dotted line is a plot of background current captured when the tip was 1 mm away from the sample surface, which had a current ~0.1 nA.

Discussion

Properties of the nanoelectrode probe. Prior to this work, fabrication techniques of AFM-SECM nanoelectrode probes include electrochemical etching of Pt or Au wires,[24,25] micro-electro-mechanical systems (MEMS),[19,26-30] and abrasion[31] have been reported. Some of these approaches successfully prepared nanoelectrodes with end-tip diameters < 100 nm.[30,47] For example, Macpherson *et al.* prepared nanowire tips with an exposed active electrode of ~80 nm diameter from single-walled carbon nanotube AFM tips that served as a template for subsequent metal deposition.[47] Conical nanoelectrode tips prepared by Staufer and Frederix *et al.* have end-tip diameters of ~20 nm obtained through a MEMS process.[29,30] In this work, we also prepare AFM-SECM probes through a wafer-based MEMS approach that allows for high batch-to-batch consistency. In addition, the conductive-path technique (Figure 3.4b) avoids coating the whole Si AFM tip with a thin film of Pt, and thus minimizes stray capacitance.[48] This approach has been widely used in the fabrication of conductive probes for nanoelectrical measurements and in the context of AFM-SECM has been shown to reduce the probability of pinholes in the passivation layer on the Pt surface.[26,28] The mounted nanoelectrode probe (Figure 3.1b) is larger than regular AFM probes (11.7 mm × 6.1 mm × 3.7 mm vs. 3.4 mm × 1.6 mm × 0.3 mm)[28,49] and the glass packaging includes designed grooves for ease of handling. These features mitigate the risk of probe damage during handling, as demonstrated by the ability to use the same probe for multiple experiments. For example, the probe used for

the stability test in Figure 3.6a went through > 4 cycles of cleaning, drying, and testing. The exposed nanoelectrode tip height is 250 ± 100 nm, which sets the upper limit for the topographic variations of samples under investigation. The spring constant of the cantilever is 1.5 ± 1 N/m. Although the tips can be used to accurately measure adhesion forces of more than 100 nN (75 nN tip bending), the tips are also suitable for modulus measurement on samples with moduli from 1 MPa to 200 MPa using PeakForce quantitative nanomechanical measurement mode.

Materials used for assembling the probes were selected or developed to meet the requirements of chemical compatibility with a range of solvents and solutions. These materials are in pH 1 and pH 13 aq. solution prepared from a variety of acids and bases, as well as in strong oxidants, e.g. HNO_3 and H_2O_2. The nanoelectrode probes are also stable in organic solvents that are frequently used for cleaning or in electrochemical experiments. For example, the conductivity measurement in dimethyl carbonate in a glovebox lasted for > 6 h with multiple clean/dry/test cycles and showed no probe damage. In addition, $LiPF_6$ in organic solvent (e.g. propylene carbonate) is typically used in the studies of Li ion batteries. The changes in mass of the probe components (glass and epoxy) measured over 124-hour immersion were negligible. These results demonstrate the excellent chemical stability of the probes.

For nanoelectrodes, various probe failure mechanisms are possible including delamination, pinhole development, metal tip etching or mechanical abrasion.[50] Another well-known cause of nanoelectrode probe failure is electrostatic discharge (ESD).[51] This was mitigated by using appropriate ESD-protected accessories. Tip contamination is also a problem that is experiment-specific (e.g. it depends on handling, solution used, and voltage applied). There is no universal approach for tip cleaning, although an air plasma cleaning method has been reported by Sun *et al*.[52] In this work, mechanical abrasion at a force of 40 –100 nN using AFM contact mode, fast CV cycling (0.3 to 0.5 V/s) in a -0.5 V to +0.5 V window, or a simple tip cleaning in de-ionized water frequently recovered the performance of the probe. Caution should be taken when probe cleaning. We observed mechanical abrasion of the Pt coating layer at 200 nN when imaging the Pt/Si_3N_4 sample. Further, a current-limiting resistor, e.g. the 10 MΩ resistor in the strain-release module, is necessary to regulate the maximum current to < 100 nA. Bypassing the

resistor may cause electrical damage to the probe when it constantly contacts a metal surface, such as in contact mode or ramp mode. CV cycling is effective for probe cleaning, but Pt stripping can occur at improper voltage ranges. Nonetheless, the sum of our data shows that the nanoelectrode is stable under broad electrochemical conditions allowing the insulated AFM tip to serve as a robust SECM nanoprobe.

The simulations reported here support the experimental capabilities of the SECM nanoprobe. Previously, Denuault *et al.* and Bard et al. conducted more-comprehensive simulations on conical nanoelectrodes with varied tip and sheath geometries.[53-55] Our simulations ignore imperfections associated with practical fabrication, such as a non-flat sheath and the non-hemispherical end-tip curvature, and assume a hemispherical tip with radius of 25 nm (Figure 3.2). Despite these simplifications, our simulations were consistent with the previously reported results and show typical radial diffusive transport and an established steady-state diffusion zone. The diffusion layer is larger than the characteristic dimension of the tip electrode. For a spherical UME, where the diffusion layer grows much larger than the tip radius r_0, the concentration or redox species near the surface becomes linear with $1/r$, where r is the distance from the electrode surface to the center of the spherical electrode.[46] Figure 3.5b shows that the approximation for a spherical UME accurately fits the simulated steady-state response of the nanoelectrode if the sphere radius is taken as 57 nm. This radial diffusion of a nanoelectrode results in a sigmoidal shape of CV curves and a steady-state diffusion-limited current, as shown Figure 3.6a. The combination of well-defined steady-state diffusion-limited current, and reliable nanoscale dimension are key criteria for achieving high-spatial-resolution AFM-SECM imaging.[50]

The ability to achieve high SECM imaging resolution is suggested by the SECM approach curves shown in Figure 3.6b. In negative feedback mode the diffusion to the electrode is blocked by an insulating surface. In positive feedback mode the SECM current is enhanced by re-generation of the active redox species by the planar electrode under bias. Comparing the simulated concentration profiles in Figure 3.5a and 3.5d shows that the current comes significantly from the tip apex. This simulation is consistent with the experimental approach curves shown in Figure 3.6b. The data collectively confirms that the current modulation observed in the approach curves originates from the

exposed tip apex and not from pin holes in the protective layer or other accidently exposed conductive components in the nanoelectrode AFM assembly. It also suggests that the spatial resolution for electrochemical imaging is primarily determined by the end-tip dimension and sub-100 nm resolution is possible, as will be discussed in the next section. Another limiting factor of the spatial resolution is the small bandwidth of the bipotentiostat and data averaging during acquisition to reduce noise. For example, a 1 nA i/E converter sensitivity was generally used when measuring currents of ~ 100 pA to a few nA. This introduces a 1 GΩ resistor in the circuit. The stray capacitance of common bipotentiostats can be 10's of pF, which results in a RC time constant of 10's of ms. Generally, for nA-level current measurement, a filter of 10's of Hz (32 Hz in this work) was used. This causes delays in electronics and data averaging in space frequently observed in AFM-SECM electrochemical mapping. Thus a slow scan rate, typically less than 0.5 Hz, is recommended for high-resolution electrochemical imaging. Figure A.A.1 shows the effect of the electronic delay at a high scan rate (12 μm/s).

PeakForce SECM. Previous SECM measurements have been performed using PeakForce tapping mode with a recessed ring electrode probe.[12] This enabled topography, electrochemical activity, and quantitative nanomechanical properties to be collected concurrently on a gold electrode patterned onto polydimethylsiloxane. While recessed electrodes provide high topographic resolution, electrochemical resolution is limited by the tip-electrode distance (> 500 nm) and electrode size (~ 500 nm). The unique contribution of the approach we have described here is the combination of lift-mode SECM with PeakForce tapping, which results in good SECM resolution, while, as demonstrated above, the ability to concurrently measure topography, mechanical properties, as well as contact electrical conduction current between the tip and substrate.

Because we control the tip-electrode distance (lift height) precisely down to ~50 nm (Figure 3.8d) and the diameter of the end-tip curvature is ~50 nm (Figure 3.4c and Table 1), ~100 nm spatial resolution in SECM current imaging is possible (Figure 3.7d and 3.8c). The disadvantage of using the same nanoelectrode tip for PeakForce tapping as for electrochemical current imaging is that contact with real-world surfaces (e.g. in biology or batteries) might contaminate the electrode surface in some cases.

Table 3.1. Geometric, mechanic, and chemical properties of the nanoelectrode probes.

Cantilever	Shape	Resonant Frequency (kHz)	Spring Constant (N/m)	Length (μm)	Width (μm)	Thickness (μm)	Height (μm)
	Rectangular	69 ± 21	1.5 ± 1	225 ± 25	25 ± 2	3.2 ± 0.6	12.5 ± 2.5
Exposed Nano-electrode	Shape	Height (nm)	Tip ROC [a] (nm)	Base Cone Radius (nm)	Sheath Radius (nm)	Electrode Material	Passivation
	Conical	250 ± 100	25 ± 8	125 ± 75	350 ± 100	Pt	SiO_2

[a] ROC: Radius of curvature

In addition to the SECM current, we can also capture and analyze the contact current. The contact current results from two sources. First, when the Pt-coated probe is landed on a conductive area, the faradic current increases due to the increased effective electrode area. Therefore, it is possible to differentiate sample areas with different surface conductivity or electrochemical reactivity through the tip contact. Second, the tip and the sample are frequently biased at different potentials for different reactions, for example, in the SECM feedback mode as shown in Figure 3.3c. The voltage difference between the nanoelectrode probe and the sample leads to the electrical current – this contact current thus contains information about interfacial conductivity between the sample and the substrate. The contact current resulting from these sources is generally higher than the diffusion-limited faradaic current and thus instrumental current saturation is frequently observed at a sensitivity setting (1 nA/V i/E converter sensitivity) suitable for acquiring the faradaic current (Figure 3.7b). For resistive surfaces the faradaic current dominates over the contact current. In this case, the tapping-cycle averaged faradaic current is captured during the main scan. This is also the case in the example of the recessed electrode probe where a single-pass scan instead of dual-pass lift mode can be used for electrochemical imaging.[12]

One unique capability for SECM electrochemical analysis is the ability to collect approach curves and perform lift-height-dependent imaging. Assisted by numerical simulation, spatially dependent interfacial charge transfer dynamics can be quantified.[56]

Figure 3.7f shows force curves on surface locations with varied electrochemical activity. The positive feedback from the Pt surface results in increased current compared to that on the nitride surface at the same tip-sample distance. The shape of these approach curves on the Pt regions depends on surface electrochemical redox activity. The higher the surface redox activity (in this case presumably due to variations in the etching of the nitride layer) the more the positive feedback competes with the blocking of the diffusive transport as the tip approaches the surface. In addition to the electrochemical response, the current spikes upon the tip-sample contact characterize the surface/interfacial electrical conductivity. Such approach curves and lift-height dependent studies can also be used to study the structure of the diffusion layers as shown by earlier nanoelectrode array examples.[57-59] For example, in Figure 3.8d, the spatial variation in SECM current is negligible at 400 nm lift height. This suggests that the concentration gradient at 400 nm away from the surfaces of both the tip and the sample electrodes are small.

Conductivity measurement in liquid with a fast sensor circuit. The SECM probe allows for electrical measurement in liquids due to the design of the tip. The tip is fully insulated except at its apex. This reduces both stray capacitance and stray currents due to the small electrically exposed area and from electrochemical reactions due to chemical impurities in liquid. Kalinin *et al.* demonstrated piezoresponse force microscopy in liquid using a conical tip of similar design in the studies of the piezo-force response of a $BaFeO_3/SrRuO_3/SrTiO_3(100)$ sample.[60-62] Pobelov *et al.* reported using a home-made conical tip with an apparent diameter of > 700 nm for simultaneous current and topography in contact mode in a ferrocene/methanol solution on a sample with Au lines on a SiO_2 surface.[63] However, contact mode suffers from high shear and imaging forces, which can damage both the tip and the sample. It also leads to the constant electrical shorting, and thus, saturation current due to the constant tip-sample contact.

In this work, we integrated our nanofabricated conductive nanoelectrode tips with PeakForce tapping for conductivity measurement in liquid. For contact current measurements, a fast electronic circuit is used to address the low bandwidth issue in a bipotentiostat. During each tapping cycle in PeakForce tapping, the tip is in contact with the sample surface from 10's to 100's of μs. The contact duration depends on the tapping frequency and amplitude. For example, at 1 kHz and 100 nm, it is about 160 μs. For

conductivity measurement, an electronic sensor module with bandwidth of 10 ~ 20 kHz was used to capture the current signals during the contact duration. This is the principle of PeakFroce Tunneling AFM (PF-TUNA).[44] In this work, we demonstrated high-performance conductivity imaging (< 10 pA background current) in organic solvent with PF-TUNA using the nanoelectrode probe to characterize a Pt surface partially covered by nitride (Figure 3.9). This example also implies the potential application of the AFM-SECM technique to battery systems for *in situ* studies. There have been a few reports of SECM for in situ and/or in operando investigation of battery systems, which has been mainly reviewed in a recent article by Schuhmann.[64] For conical probes used in AFM-SECM, however, the tip height sets the upper-limit of surface variation for topographic studies, e.g., ~250 nm for probes in this work. Fortunately, there have been many model systems with surface-height variations below 200 nm, for example, as recently shown on thin film[65], HOPG,[66] and graphene electrodes[67].

Heterogeneity in HOPG electrode properties from AFM-SECM. The demonstrated high resolution and the multimodal imaging abilities of PeakForce SECM provide new insights into many different material systems. One example is HOPG, a lamellar semi-metallic material consisting of a periodic stack of two-dimensional graphene sheets. It is widely used as an electrode material in biochemistry, catalysis, and batteries applications. Therefore, its electrical properties and electrochemical activities in liquid are important to understand. The edge planes of HOPG have long been considered to be electrochemically active with the basal planes being relativity inert in comparison.[68,69] However, recent work utilizing advanced scanning electrochemical cell microscopy,[70-74] as well as other nanoscale[75-77] and macroscale[73,78,79] techniques, found that pristine basal planes demonstrated fast electron-transfer kinetics, similar to the edge planes. In addition, the Unwin group also found that aged samples exhibit an enhanced electrochemical activity at the step edges compared to the terraces.[80,81] In this work, HOPG step edges were resolved on topography images by PeakForce SECM (Figure 3.10a). While there is some small enhancement in electrochemical activity at these step edges (Figure 3.10c), the enhancement is minor in comparison with the basal plane activity. We also observed defect sites associated with sub-nm height steps (Figure 3.10a). The corresponding electrochemical activity (Figure 3.10c) at the defect site is ~10%

lower than the basal plane. A similar type of defect was observed by Wain *et al.*,[28] although they were not able to resolve related topography variations. In addition to high resolution topographical and SECM imaging, we measured quantitative adhesion forces collected simultaneously. From Figure 3.10b it is apparent that a distinct variation in surface mechanics exists at the defect site. The correlation between the mechanics and electrochemistry remain unclear and requires further investigation.

In addition to the electrochemical inhomogeneity at the nanoscale, we find the HOPG sample has varying resistivity across the sample surface (Figure 3.11). Generally, the electrical resistivity along the basal plane is ~4 orders of magnitude lower than in the vertical inter-layer direction (4×10^{-5} vs. 0.15 Ω·cm).[82] Therefore, one might expect the edge sites to show higher current than the basal surface area in local contact conductivity measurements. However, the measured current also depends on the type of edges (*i.e.*, stable armchair or active zigzag configuration) which the probe encounters. The armchair edge is less conducting and can show less current than the terrace.[83] In addition, loosely held graphite sheets were also found to have enhanced conductivity.[82] The conductivity map collected here shows clear current contrasts between terraces, edges and flake sheets. Although edges generally have higher currents than terraces, they show inhomogeneity among different edge sites. The most conductive sites appear to be on the flake sheets. These conductive properties were also confirmed by the *I-V* characteristics at the locations of different features. During the *I-V* curve measurement, the tip constantly contacted the sample surface. Finally, we note that the repeated measurement of the saturation current of ~550 nA, and thus ~ 5.5×10^5 mA cm^{-2} (the electrode surface area is ~ 10^{-9} cm^2), suggests that these nanoelectrode probes are electrically robust for carrying high current.

Conclusion and Bridge

A combined SECM-AFM technique using PeakForce tapping and lift mode, enabling high resolution multimodal imaging, has been detailed. PeakForce tapping allows for topography, contact current and nanomechanics to be mapped simultaneously with the SECM current collected in lift mode. Experiments were performed using batched-fabricated probes from a reproducible MEMS process. These probes were subject to tests

of chemical compatibility with a wide range of electrochemical environments, electrochemical performance, mechanical stability, and multiple-cycle handling. COMSOL modeling of the SECM process provides insights about the electrochemical properties of the probes, including the diffusion-limited current, concentration profiles and approach curves. These probes enabled high resolution electrochemical imaging (≤ 100 nm) and electrical characterization techniques in liquid. We have demonstrated these capabilities on lithographically prepared samples (patterned Pt strands and Au nanomesh electrodes). More importantly, the developed probe and technique reported in this work were used to characterize a HOPG electrode, showing the edge planes have slightly enhanced electrochemical activity compared to the basal planes (consistent with other literature reports). New observations from this work include the identification of defect sites on HOPG, where a sharp drop in SECM current corresponded to a change in the adhesion force as well as a small height step. Finally, high-resolution conductivity measurements in liquid using the nanoelectrode probe and fast sensor electronics for the first time show the conductivity heterogeneity of the HOPG surface in liquid. The described system presents an advance in the field of combined AFM-SECM due to its multimodal imaging capabilities at high resolution.

By testing these electrochemical abilities, we have completed proof-of-principle work demonstrating these probes are likely suitable to operate under water oxidation conditions. We will focus the next chapter (Chapter IV) on exploring the ability of the nanoelectrode probes to sense catalyst surface potentials. This will provide insight into the operation of OER catalysts and the role of the sem|cat interface on more complicated semiconductors, like Fe_2O_3.

CHAPTER IV

POTENTIAL-SENSING ELECTROCHEMICAL ATOMIC FORCE MICROSCOPY FOR IN-OPERANDO ANALYSIS OF ELECTOCATALYST DURING (PHOTO)ELECTROCHEMCIAL WATER SPLITTING

Chapter IV contains co-authored work published in volume 3 of Nature Energy in 2017 (*Nat. Energy* **2018**, *3*,46−52). This work was written primarily by me. Hajibabaei, H.; Sivula, K. and Hamann, T. W. provided experimental assistance. Laskowski, F. A. L.; Qiu, J. and Boettcher S. W. provided editorial assistance.

Introduction

Photoelectrochemical (PEC) water-splitting enables the direct conversion and storage of solar energy into energy dense chemical fuel, H_2[1]. Significant effort has been devoted to develop earth-abundant material systems to drive water splitting, for example water-oxidizing photoanodes made from nanostructured metal-oxide light absorbers with catalytic surface layers[2–5]. Understanding the interfacial charge-transfer processes for these systems, specifically the role of the catalyst layer in the enhancement of the oxygen evolution reaction (OER), has been a major challenge[6]. For example, it has been proposed that the catalyst increases band bending in the semiconductor[7,8], improves charge separation in the semiconductor[9], or simply enables more facile OER kinetics[10,11]. Improving the performance of catalyzed photoanodes requires a detailed understanding of the system's fundamental electronic processes. A major roadblock is that the charge state, or surface electrochemical potential, of the catalyst layer cannot easily be measured directly by standard (photo)electrochemical techniques that rely only on an ohmic back contact to the semiconductor.

To directly probe charge-transfer processes in catalyst-coated photoanodes, we previously developed a "dual-working-electrode" (DWE) technique[12,13] where a thin, electrolyte-permeable, Au layer is deposited on the catalyst. The layer is used as a second working electrode to sense or control the voltage and/or current at the catalyst surface. We initially studied model TiO_2 semiconductors coated with Ni(Fe) (oxy)hydroxide

catalysts and showed photogenerated holes accumulate in the catalyst layer, oxidizing it to potentials where catalytic water oxidation occurs. Because the catalyst is permeable to electrolyte, the effective barrier height at the catalyst-semiconductor junction increases as the catalyst is oxidized, which we termed an "adaptive junction"[13–15]. The technique was further applied to Si photoanodes, a model low-bandgap absorber, which illustrated that the need for a non-porous protection layer, in this case metallic-Ni, precluded such adaptive behavior[16]. Most recently, DWE photoelectrochemistry of $Ni_{0.8}Fe_{0.2}O_x$-coated planar α-Fe_2O_3 was enabled by using very smooth spin-coated catalyst layers (< 1 nm RMS roughness)[17].

While a powerful tool to understand charge-transfer processes in planar model systems with uniform catalyst layers, the DWE approach is limited. Application of the second working electrode layer to the top of a catalyst with imperfect or non-uniform coverage results in direct electrical shorting to the underlying substrate. This has prevented the study of highly structured semiconductors, patterned catalyst architectures, or photoanodes with (photo)electrodeposited catalyst films that crack when they are removed from electrolyte and dried. A more versatile and, ideally, spatially resolved potential-sensing technique is needed.

Scanning electrochemical potential microscopy (SECPM), wherein a piezo actuator and a nanometer potential probe can be used to measure the potential gradient of an electrical double layer as the probe approaches a biased conductive surface[18–21], provides one possible route to measure surface potentials in situ. SECPM has been used to map high resolution images in constant potential mode, an analogue of electrochemical scanning tunneling microscopy which operates in constant current mode[22–24]. SECPM imaging, however, conflates topography with potential, which makes it difficult to apply to systems where both the surface topography and potential are unknown, such as catalyst coated photoelectrodes.

Other groups have worked to extend Kelvin probe force microscopy (KPFM) to liquid environments for nano-scale potential sensing, but these techniques are complicated by mobile ions in solution. This has limited their application to non-polar liquids[25], pure water[26,27], or low concentration electrolyte (<10 mM) solutions[28,29] –

conditions that are not representative of most practical (photo)electrochemical environments.

Here we demonstrate a potential-sensing electrochemical atomic force microscopy (PS-EC-AFM) technique to directly measure the surface electrochemical potential in heterogeneous electrochemical systems *in operando*. We define *in operando* in the context of semiconductor photoelectrochemistry as where the sample is illuminated, under bias, passing photocurrent, and in a practical electrolyte solution. For potential sensing, we employ a conductive nano-tip of an otherwise electrically insulated atomic force microscope cantilever (Figure 4.1a)[30,31] that is placed in direct contact with the sample. As an AFM-based technique, PS-EC-AFM integrates force-feedback to control tip-substrate interactions (*via* cantilever deflection). This is allows for maintaining stable electrical connection between the substrate and the AFM nanoelectrode potential sensing tip, without damaging the catalyst or AFM tip *via* excessive force. The small area over which the tip interacts with the electrolyte ($\sim 10^{-9}$ cm^2) minimizes capacitive and surface electrochemical processes that may prevent measurement of the catalyst potential. We demonstrate the utility of PS-EC-AFM by measuring operating surface potentials in two prototypical (photo)electrochemical systems – cobalt (oxyhydroxide) phosphate "CoPi" electrocatalyst films[32,33] on conducting glass electrodes and CoPi-catalyzed hematite (α-Fe_2O_3) photoelectrodes. The Fermi level of the catalyst and the tip are assumed to be in equilibrium, enabling the catalyst surface potential to be probed via the tip (Figure 4.1b). We show that CoPi is a good electrical conductor only when oxidized to potentials anodic of the $Co^{2+/3+}$ redox wave. When CoPi is deposited on hematite, we show that it collects photogenerated holes from the hematite surface and charges to a potential sufficient to drive water oxidation at the (simultaneously measured) photocurrent density. These measurements thus directly demonstrate the role of CoPi as both a hole collecting contact and electrocatalyst for water oxidation. Studying these systems with macroscopic DWE measurements would not be possible due to the roughness of mesostructured hematite and cracking of (photo)electrodeposited films during the drying step.

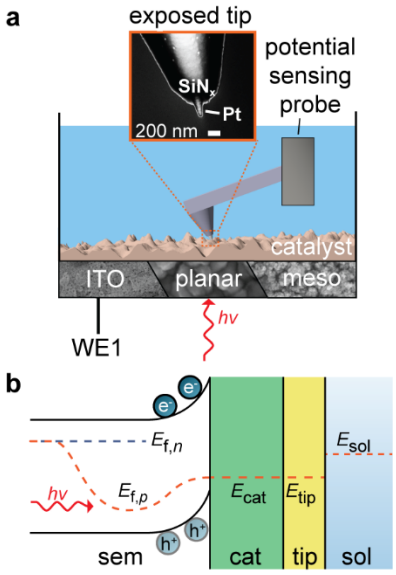

Figure 4.1. AFM method to measure catalyst surface potential during (photo)electrochemical experiments. (a) The potential-sensing electrochemical AFM setup with the cantilever, fully electrically insulated except for the exposed nano-tip, serving as a potential probe. The inset is an electron micrograph of the AFM tip used. The blue color represents electrolyte. The approach allows for the study of a wide range of (photo)electrochemical structures *in operando*, including electrodeposited catalysts on conducting indium tin oxide (ITO), planar hematite and nano/mesostructured hematite. (b) Band diagram for an illuminated semiconductor (sem) electrode (e.g. Fe_2O_3) coated with a catalyst (cat) layer (e.g. CoPi). $E_{f,n}$ and $E_{f,p}$ are the electron and hole quasi fermi levels, respectively. E_{cat} and E_{tip} are the Fermi levels of the catalyst and AFM tip, which are assumed to be in equilibrium. E_{sol} is the redox potential of the electrolyte, here given by the thermodynamic potential for the oxygen evolution reaction $\mathcal{E}_{O_2/OH^-}$. The difference between E_{sol} and E_{cat} is the overpotential driving water oxidation.

Direct measurement of electrocatalyst surface potentials

To demonstrate the viability of the potential-sensing technique, we first studied CoPi deposited on a conductive ITO substrate. Despite its wide use, little is known about the electrical properties of CoPi. Recent reports have suggested that there are potential losses related to charge transport through the film at sufficiently high current densities[34,35]. Thus, even when controlling the substrate potential *via* a potentiostat, the electrochemical potential driving oxygen evolution at the catalyst surface remains uncertain.

PS-EC-AFM measurements were made using a custom EC-AFM cell/stage that allowed for bottom illumination with a 405 nm LED, an Ag/AgCl reference electrode, and a Pt counter electrode (Figure A.B.1). A high impedance (1 TΩ) sense lead of the potentiostat was used to measure the tip potential, V_{tip} (Figure A.B.2) *via* the conductive AFM probe. The setup was tested by sensing V_{tip} when the tip was in contact with an Au substrate whose potential, V_{sub}, was controlled using the first working electrode of the potentiostat. V_{tip} tracked V_{sub} exactly at a contact force of ~25 nN (Figure A.B.3).

CoPi films were deposited on an ITO substrate from a 0.5 mM aq. $Co(NO_3)_2$ solution at an anodic current density of 50 μA cm^{-2} for 10-30 min. Catalyst loading was monitored by the integration of the Co^{2+}/Co^{3+} reduction wave. The exposed conductive AFM tip was brought into contact with the ITO or catalyst-coated ITO and the surface was imaged using a force-sensitive tapping mode (Figure 4.2a and 2b). The probe was rested on the catalyst surface with an applied force of ~25 nN, which was sufficiently small to prevent damage to CoPi films (Figure A.B.4), and the potential of the ITO was stepped anodically in 100 mV steps. At $V_{sub} < 0.2$ V vs $\mathcal{E}_{O_2/OH^-}$ (the OER thermodynamic redox potential), V_{tip} was largely unaffected by changes in V_{sub}. When V_{sub} was ≥ 0.27 V vs $\mathcal{E}_{O_2/OH^-}$, V_{tip} began closely tracking V_{sub} (Figure 4.2c, Figure A.B.3). This observation is consistent with the dramatic increase in electrical conductivity that has been observed when $Co(OH)_2$ species are oxidized to CoOOH, supporting the idea that CoPi is composed of Co (oxy)hydroxide nanosheet fragments that are only electrically conductive when oxidized[36,37]. We observe similar behavior for a range of catalyst loadings (Figure A.B.5), although thicker films require less anodic potentials, as measured by the EC-AFM tip, to achieve any given current density (Figure 4.2d). This is expected as CoPi is a volume-active electrocatalyst (i.e. porous and electrolyte permeable)[38]. For the thickest films employed (~125 nm) we measured V_{sub} - V_{tip} = ~20 mV at current densities of ~1 mA cm^{-2} (Figure A.B.6) – indicative of electrical resistivity losses for transport through the CoPi layer. Some of this potential drop can also be attributed to contact resistance between the catalyst and the probe, which can vary between probes and with the series resistance through the ITO substrate. We note that at current densities of ~1 mA cm^{-2} or greater, oxygen evolving from the sample surface can

disrupt the tip, lifting it from the substrate. Because the potential sensing tip is composed of Pt, which is a much-worse OER catalyst than CoPi,[39] negligible catalytic current flows through the Pt itself as shown in Figure A.B.7.

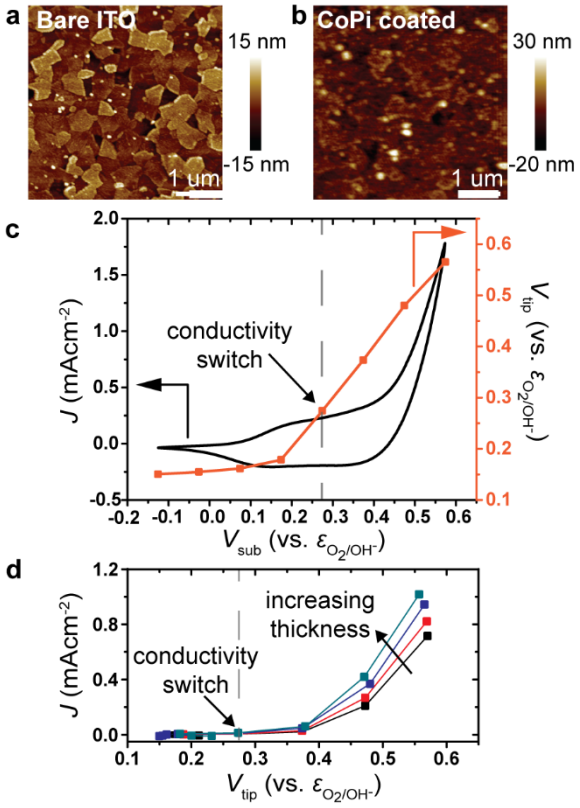

Figure 4.2. Surface potentials of CoPi on an ITO substrate. (a) AFM topographic image of bare ITO surface. (b) AFM topographic image of CoPi-coated ITO surface. (c) Potential stepping experiments performed in 0.1 M aq. potassium phosphate, buffered to pH 6.9. V_{tip} began tracking V_{sub} at 0.27 V vs ε_{O_2/OH^-}, corresponding to the oxidation of the CoPi. The substrate was held at each potential for up to 1 min, allowing the V_{tip} measurement to stabilize. Voltammetry for the CoPi/ITO is also shown (20 mV s^{-1}). The potential labeled "conductivity switch" is the point where the catalyst is sufficiently oxidized that it becomes electrically conductive and thus its potential can be sensed. (d) V_{tip} (measured catalyst potential) and the corresponding steady-state currents taken from potential step experiments as shown in panel c. As the thickness of the catalyst is increased both the number of catalytically active sites, and the current at a fixed overpotential, increases. Approximate catalyst thicknesses for the black, red, purple and teal lines are 49 nm, 59 nm, 103 nm and 126 nm, respectively.

The measurements on CoPi/ITO demonstrate that PS-EC-AFM can accurately measure the applied potential (typically within 25 mV, Figure A.B.6) at catalyst surfaces and differentiate between electrically conducting and non-conducting states of the catalyst. The technique further allows for measurement of heterogeneity in electrical properties on the same sample. Figure A.B.8 shows that a nanoscale pinhole exposing the Au substrate can be distinguished from electrodeposited Co (oxy)hydroxide catalyst by sensing the surface potential during a cyclic voltammogram (CV). PS-EC-AFM therefore provides direct information about the local electrochemical potential available to drive catalysis. Such information is not readily available by other techniques. Impedance analysis has been used to assess the series resistance of catalytic electrodes, but it is difficult to extract the resistance of the catalyst network for porous catalyst structures where solution permeation through the catalyst promotes mixed ionic/electronic transport[40,41].

Semiconductor/electrocatalyst junction behavior

The data above demonstrates the prerequisites for applying the measurement to photoelectrodes with porous catalyst overlayers. We use PS-EC-AFM to directly measure the surface potential of CoPi on planar hematite semiconductor photoelectrodes prepared *via* atomic layer deposition[42]. Following CoPi photo-electrodeposition (50 μA cm^{-2} under illumination, 6.9 mC cm^{-2} redox-active cobalt, ~100 nm thick), the CoPi/planar hematite was imaged and the conductive nanoelectrode AFM cantilever was rested on the sample surface with an applied force of 25 nN. The substrate potential, V_{sub} (applied to the hematite ohmic back contact, while under illumination), was stepped anodically in 100 mV increments while V_{tip} was measured. From V_{sub} = -0.8 V to -0.43 V vs $\mathcal{E}_{O_2/OH^-}$, V_{tip} did not substantially change, consistent with the catalyst remaining uncharged/reduced (and thus nonconductive) under these conditions. At V_{sub} = -0.33 V vs $\mathcal{E}_{O_2/OH^-}$, sufficient photogenerated holes were injected to oxidize the CoPi to the conductive state (Figure 4.3a). At that conductivity switch potential, V_{tip} equilibrates to 0.29 V vs $\mathcal{E}_{O_2/OH^-}$ (the potential of the catalyst). The catalyst potential build-up is driven by the system photovoltage (V_{ph}), which is given by $V_{ph} = V_{tip} - V_{sub}$ = 0.62 V. For the catalyst loadings

used here, the potential loss through the CoPi film should be small relative to the photovoltage.

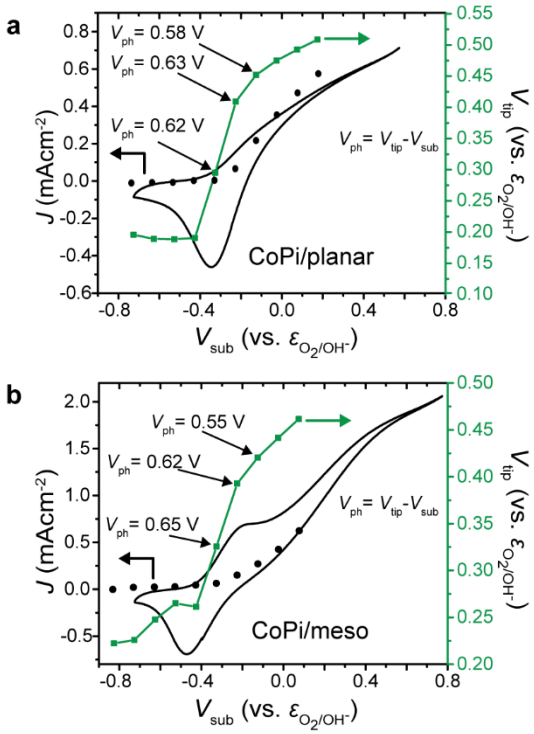

Figure 4.3. *In operando* PS-EC-AFM potential-stepping photoelectrochemical experiments. The measured potential of CoPi on planar hematite (a) and the measured potential of CoPi on mesostructured hematite (b). The green squares represent the catalyst potential measured by the AFM tip. The simultaneously measured steady-state photocurrent is depicted with black circles. The black lines are voltammograms collected after the potential stepping experiment (20 mV s^{-1}). Both systems were illuminated with 405 nm light calibrated to 27 mW cm^{-2} and collected in 0.1 M potassium phosphate, buffered to pH 6.9. The substrate was held at each potential for up to 2 min, allowing V_{tip} readings and currents to stabilize. *In situ* AFM images and SEM images of the CoPi coated hematite, as well as voltammetry of the bare electrodes, are shown in Figures A.B.10- A.B.12.

The technique was further extended to nanostructured hematite synthesized by atmospheric pressure chemical vapor deposition (APCVD)[43,44]. These samples are rougher than the ALD deposited “planar” hematite and contain substantial mesoporosity (Figure A.B.9 shows SEM and AFM images). Due to sample roughness, measuring the semiconductor/catalyst junction would be impossible using macroscopic DWE

techniques that we have employed previously. CoPi was photo-electrodeposited onto the mesostructured hematite (50 μA cm^{-2}, under illumination). Compared to planar hematite, higher catalyst loadings (9.1 mC cm^{-2} of redox active Co, ~140 nm planar-equivalent thickness) were required due to the larger surface area of the mesostructured sample. When loading/film thickness was too low, the probe did not make sufficient electrical contact with the catalyst and the potential could not be reliably sensed.

As in the case of the planar hematite, the probe was rested on the sample surface (force ~25 nN) and V_{sub} was stepped anodically while the steady-state V_{tip} was measured (typically after 1-2 min per step), under illumination. At V_{sub} = -0.33 V vs ε_{O_2/OH^-} the CoPi film was oxidized to the conductive state, driven by the photogenerated holes in the hematite. Based on the measured potential of the CoPi film, V_{ph} is ~0.62 - 0.65 V. We also quantify the photovoltage by comparing V_{sub} at the conductivity switch for CoPi/ITO and CoPi/α-Fe_2O_3 systems. For both planar and mesostructured hematite, the conductivity switch occurred ~0.6 V cathodic of the CoPi/ITO system, consistent with the ~0.6 V photovoltage measured directly between the probe tip and substrate.

The ability to measure the surface potential for a catalyst on a photoelectrode allows us to directly test whether steady-state hole current flows through the CoPi layer or whether the water oxidation happens primarily on the hematite surface. This question is important because several recent studies have suggested that the CoPi acts largely as a spectator that favorably modulates the interface energetics but does not directly drive the OER[7,45,46]. Using PS-EC-AFM, we compare catalyst potentials necessary to drive a given OER current for CoPi/hematite and CoPi/ITO systems (Figure 4.4) with nominally the same catalyst loading (as measured by the integration of the Co redox wave). For the CoPi/hematite (planar) system, the catalyst potentials, for a given photocurrent density, are nearly identical to those measured at the same current density for CoPi/ITO in the dark. This demonstrates that the CoPi is charged by photogenerated holes from hematite until it reaches a potential where the rate of CoPi-mediated water oxidation is equal to the steady-state junction photocurrent.

For the mesostructured system, we also observe that the CoPi is charged to potentials where it drives oxygen evolution. However, for a given measured catalyst potential (V_{tip}), the CoPi on ITO passes a slightly smaller *average* current density than the

CoPi on hematite. This difference is likely due to the morphology differences of the CoPi between the planar ITO and rough hematite. Because light is incident on the backside of the hematite, the <10 nm collection length of photogenerated holes dictates that a large portion of the photocurrent is passed through catalytic particles at the base of the porous hematite film[47,48]. These catalyst particles at the bottom are likely not well-electrically integrated with the catalyst film at the top of the porous semiconductor, where AFM sensing occurs. Catalyst regions at the top (and sensed by the AFM tip) would therefore sit at less anodic potentials and pass a local current density that is lower than the average measured through the substrate and shown in Figure 4.4. Nonetheless, at relevant catalyst potentials of ~0.4 – 0.45 V vs $\mathcal{E}_{O_2/OH^-}$ the differences between the average current measured on the CoPi/ITO and CoPi/hematite are only ~5 - 25% of the photocurrent, again consistent with the hypothesis that photogenerated holes oxidize the CoPi which then directly drives the OER.

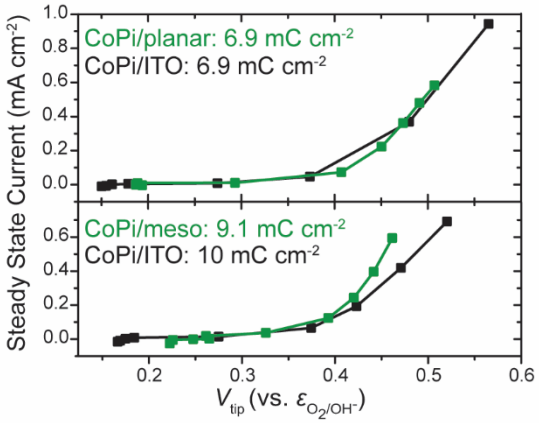

Figure 4.4. CoPi surface potential measurements at given current densities**.** For illuminated CoPi/planar hematite (top) and illuminated CoPi/mesostructured hematite (bottom), the corresponding dark CoPi/ITO systems shown have nominally the same catalyst loadings. The fact that the curves for the conducting ITO substrates overlay those of the semiconductor photoelectrode substrates indicates the catalyst is behaving in the same fashion in both cases, independent of whether the holes originate from the ITO or are photogenerated in the hematite. The CoPi acts as a hole-collecting contact and a OER catalyst.

Finally, we note that samples with very high surface roughness may make these measurements more difficult as the contact area between tip and surface may change. We have, however, reliably measured samples with root-mean-squared (RMS) roughness

varying from ~17 to 40 nm (Figures A.B.13 and A.B.14). A consistent electrical contact is ensured in these cases by the ability of the AFM to maintain a constant contact force.

Methods

Planar Fe_2O_3. Thin films of Ga_2O_3 and Fe_2O_3 were prepared by atomic layer deposition (ALD) (Savannah 100, Cambridge Nanotech Inc.), using a previously reported procedure.[42,48,50,51] Prior to deposition of Fe_2O_3, a ~2 nm Ga_2O_3 underlayer was deposited on F:SnO_2 (FTO) coated aluminoborosilicate glass substrates (Solaronix, 10 Ω/sq). The FTO substrates were cleaned by sequential sonication in soap, water, and isopropyl alcohol for ~ 15 min followed by drying in a stream of N_2. The Ga_2O_3 was deposited using tris-(dimethylamido)gallium(III) (Strem Chemicals Inc.) and H_2O as the Ga precursor and oxidant, respectively, using a modified version of previously reported recipe.[52] Briefly, the Ga precursor was kept at 150 °C and was pulsed for 0.2 s under exposure mode for 8 s, followed by purging for 12 s. Subsequently, H_2O was pulsed for 15 ms with the same exposure/purge time to complete one ALD cycle. A growth rate of ~ 1.1 Å Ga_2O_3 per cycle was measured by spectroscopic ellipsometry (Horiba Jobin Yvon, Smart-SE) on a Si wafer. The Ga_2O_3-coated FTO substrates were then coated with a ~ 30-nm-thick film of Fe_2O_3 by alternating pulses of ferrocene and a combination of water and ozone as the iron precursor and the oxidant, respectively. The ferrocene cylinder was kept at 70 °C and was pulsed for 20 s. Then, an oxidation cycle which included 10 subcycles of H_2O pulsed for 15 ms followed by a 2 s pulse of ozone was completed. Each subcycle was separated by purging for a duration of 5 s. After the deposition of Fe_2O_3, films were annealed at 500 °C for 30 min with a ramp rate of 17 °C min^{-1}, and allowed to cool to room temperature over 2 h. Subsequently, the films were sintered in a preheated oven at 800 °C for 4 min then quenched to room temperature by removing from the oven.

Mesostructured Fe_2O_3. Films were prepared *via* atmospheric-pressure chemical vapor deposition (APCVD), as previously described[43,44]. Briefly, iron pentacarbonyl ($Fe(CO)_5$, Acros 99.5%,) and tetraethoxysilane (TEOS, Aldrich 99.999%, for Si doping) were used as precursors and brought into the gas phase by bubbling argon gas (99.9999%) through each precursor liquid, in separate vials, at different rates: 36 mL min^{-1} for $Fe(CO)_5$ and 30 mL min^{-1} for TEOS at 25 °C. A carrier gas stream (dry air, 6 L min^{-1}) was combined

with the reactive gas streams and was directed vertically onto a heated substrate (12 mm × 30 mm F:SnO_2 on float glass, TEC 15 measured to be at 420 °C) through a glass tube of 12 mm inner diameter from a distance of 20 mm. A sheath flux of dry air (total 12 L min^{-1}) was directed around the heater to facilitate the exhaust of the unreacted precursors. The film was deposited over 3 min giving an approximate film thickness of 500 nm. After cooling, the films were stored in ambient conditions until use. Films were annealed at 350 ˚C for 10 min prior to electrode preparation to remove any volatile organic compounds on the surface.

Photoelectrochemistry. All experiments were performed in 0.1 M phosphate buffer adjusted to pH 6.9. Solutions were prepared from 18 MΩ·cm water. *In operando* AFM experiments were performed using a custom-modified commercial Bruker EC-AFM cell. The modifications enabled bottom illumination of the hematite as well as the use of a standard Ag/AgCl reference electrode with a saturated KCl filling solution (Pine Research). The potential vs. the Ag/AgCl reference electrode was converted to the potential vs the thermodynamic potential for oxygen evolution using the formula $V \text{ vs. } \mathcal{E}_{O_2/OH^-} = V \text{ vs. } \mathcal{E}_{Ag/AgCl} + 0.197\,V - 1.23\,V + (0.059\,V * pH)$. Substrates were adhered to the homemade Teflon or Kel-F baseplate using double-sided copper tape, electrically connected to a copper wire with silver paint and epoxied to secure the substrate as well as to isolate the conductive components (excluding the substrate) from the electrolyte. A Pt wire lined the inside of the cell and was used for the counter electrode. The cell was illuminated by a 405 nm LED light source (ThorLabs). Light intensities were calibrated using a GaP photodiode to provide the same photocurrent on the GaP as 100 mW cm^{-2} of AM1.5 illumination; i.e. ~27 mW cm^{-2} at 405 nm. The light intensity was verified using a broadband thermopile power meter (Melles Griot). A hematite sample and the Teflon baseplate, as well as the custom-built AFM stage used for photoelectrochemical experiments, are shown in Figure A.B.1.

CoPi deposition. Cobalt phosphate OER catalysts were deposited using a 0.1 M phosphate buffer at pH 6.9 with 0.5 mM $Co(NO_3)_2$, at a current density of ~50 µA cm^{-2}. Deposition times were varied, or additional depositions were performed, to control CoPi loading. Hematite samples were illuminated using a 405 nm LED at 27 mW cm^{-2}, as described above. Catalyst loading was monitored by the integration of the reduction wave

for ITO and hematite samples. AFM and SEM images of CoPi- coated hematite electrodes are shown in Figure A.B.11. SEM cross-sections of CoPi-coated mesostructured hematite and coated ITO are shown in Figure A.B.12.

Estimation of CoPi thickness. To estimate the CoPi thickness we started with the relationship defined by Surendranath *et al.*[53] based on previous work[54,55].

$$\text{thickness (nm)} = 1.5 \left(\frac{\text{nm} \cdot \text{cm}^2}{\text{mC}}\right) \cdot Q_{\text{dep}} \left(\frac{\text{mC}}{\text{cm}^2}\right)$$

Q_{dep} is the charge per cm^2 passed during the deposition, with the assumption that all charge passed is used to oxidize Co^{2+}. This assumption holds for slow deposition rates, while faster depositions may have some percentage of charge used to oxidize water[32,56]. We chose to deposit at a constant current density of 50 μA cm^{-2} because of the speed of catalyst deposition, as well as the ability to maintain similar deposition parameters for a variety of substrates (ITO, planar and mesostructured hematite). Therefore, we used the integration of the reduction wave to directly compare loadings. Since it has been suggested that only 10% of the CoPi film is redox active[34], we replaced Q_{dep} with $10 \times Q_{\text{red}}$, as shown below, where Q_{red} is the integrated charge in the CoPi reduction wave.

$$\text{thickness (nm)} = 1.5 \left(\frac{\text{nm} \cdot \text{cm}^2}{\text{mC}}\right) \cdot 10 \cdot Q_{\text{red}} \left(\frac{\text{mC}}{\text{cm}^2}\right)$$

Measurements. A Dimension ICON AFM (Bruker, USA) was used for both topographical imaging of bare substrates in air (Tapping mode, TESPA V2 probes) and for *in operando* electrochemical work (PeakForce Tapping mode, scanning electrochemical microscope [SECM] module, SECM probes). A Bio-Logic SP300 potentiostat fitted with an ultra-low current option was used for (photo)electrochemical measurement. For potential-sensing DWE measurements, the counter-electrode potential sense probe was separated from the counter electrode and attached to the AFM tip (through the strain release module). The SECM probe was held on the sample surface using the point-and-shoot function in the Bruker software. All the results reported were reproducible and representative of the typical behavior observed for each system (Figure A.B.14). Scanning electron microscope images (SEM) were collected using a Zeiss Ultra 55 SEM at 5 keV beam energy and with a 30-μm aperture.

Conclusion and Bridge

We report a PS-EC-AFM technique that enables the probing of the electrical and interfacial properties of heterogeneous electrochemical systems. This allows investigation of electrodeposited catalysts like CoPi, *in operando* – a material that was not able to be studied by macroscopic potential-sensing techniques previously used. We obtain insight into CoPi electrical conductivity, as well as demonstrate a route to interrogate the role of CoPi on hematite photoanodes. We show that for both planar and mesostructured hematite samples, the CoPi is oxidized to a sufficiently high potential to drive water oxidation at a rate commensurate with the junction photocurrent. This data therefore shows that CoPi acts as a hole collecting contact and oxygen evolution catalyst. These results thus add substantially to previous studies, where in some cases CoPi was thought only to improve band bending and/or surface passivation while the OER predominantly occurred on the semiconductor surface. The results here do not rely on modelling, fitting, or indirect optical measurements. Since the approach is versatile (and can be applied with any device-fabrication strategy), it may be further used to elucidate the roles of catalyst thickness, morphology, and semiconductor structure in semiconductor photoelectrodes.

The PS-EC-AFM technique should be broadly applicable in the study of other electrochemical systems. Because it is based on a scanning-probe platform, the technique is suited for understanding heterogeneity in surface or interface electrochemical response (although not fully exploited in this work, our preliminary results in Figures A.B.8 and A.B.15 indicate this is possible). We have recently hypothesized the presence of a spatially inhomogeneous interface barrier for metallic-Ni-protected Si due to adventitious SiO_2 formation[16]. PS-EC-AFM could provide direct evidence for this hypothesis, which would be difficult to obtain in any other way. The technique could also provide insight into corrosion processes, where there is evidence for nanoscale potential domains[49], as well as new routes to understand the operation of batteries, fuel cells, and other electrochemical systems. Measuring and mapping the electrochemical potential *in operando* could provide insight into such systems' operation and efficiency losses.

While this work provides conclusive evidence of the role of CoPi on Fe_2O_3, lingering questions remain for other semiconducting substrates- specifically bismuth vanadate. These questions are in part rooted by the idea that bismuth vanadate has faster

OER kinetics than Fe_2O_3. This suggests that the primary role of catalysts like CoPi, when paired with $BiVO_4$, is to reduce recombination rather than catalyzing OER. By expanding the PS-EC-AFM technique to study catalyzed bismuth vanadate, we can develop a clear understand of how the role of the catalyst may change based on the semiconductor it is on.

CHAPTER V

CO-PI IS A HOLE COLLECTOR AND OXYGEN EVOLUTION CATALYST ON $BiVO_4$ WATER-SPLITTING PHOTOANODES

Chapter V contains co-authored unpublished work that has been submitted to *ACS Energy Letters*. This work was written primarily by me. Qiu, J.; Laskowski, F. A. L. and Toma, F. M. provided experimental assistance. Boettcher S. W. provided editorial assistance.

Introduction

Bismuth vanadate ($BiVO_4$) has been studied extensively as an oxygen-evolving photoanode for solar water splitting.[1,2] Bare $BiVO_4$, however, is thought to suffer from high rates of bulk and surface recombination.[3,4] To overcome this, $BiVO_4$ is often paired with different oxygen evolution reaction (OER) catalysts, including CoPi,[3,5–9] NiOOH/Ni borate,[10,11] FeOOH,[12,13] NiFeOOH-borate[14] and layered FeOOH/NiOOH,[15] all of which have been shown to improve onset potentials for photoelectrochemical (PEC) water oxidation.

The exact role these catalytic materials play in enhancing PEC performance is still poorly understood, but multiple competing mechanistic hypotheses exist. Several studies report that catalytic layers serve only to reduce surface recombination and do not drive the OER directly.[16–18] Based on photo-induced optical absorption measurements, Ma *et. al.* report that CoPi on $BiVO_4$ never reaches sufficiently anodic potentials to drive water oxidation,[17] and that holes on the surface of $BiVO_4$ directly oxidize water without transferring to the catalyst. Zachäus *et al.* came to a similar conclusion for $BiVO_4$|CoPi under low applied potentials (V_{sem} < 1 V vs. RHE), using intensity modulated photocurrent spectroscopy.[18] At higher potentials, however, they hypothesize that CoPi must partially drive water oxidation because kinetics on the $BiVO_4$ are too slow.

Conversely, it has also been hypothesized that CoPi on $BiVO_4$ suppresses surface recombination, but also collects photogenerated holes to catalyze water oxidation with near 100% quantum efficiency.[5] For $BiVO_4$ coated with a FeOOH|NiOOH layered

catalyst, Kim *et al.* suggested that the FeOOH reduces interfacial recombination while NiOOH enhances OER kinetics.[15] This implies that the NiOOH collects photogenerated holes from the $BiVO_4$ and catalyzes the OER. Likewise, Lange *et al.* used *operando* soft X-ray absorption spectroscopy to study MnO_x coated $BiVO_4$ and found that photogenerated holes are transferred to the MnO_x film where water oxidation reportedly takes place at Mn^{3+} sites.[19]

Clarifying the function by which oxide/(oxy)hydroxide overlayers enhance $BiVO_4$ performance is important because it enables strategic photoanode design targeted to passivate surface states (reduce recombination), enhance hole collection efficiency, and/or lower the overpotential lost in driving the OER reaction. To understand the overlayer role, we develop a model $BiVO_4$|CoPi system amenable to direct electrical measurement of the CoPi potential in an electrochemical cell under illumination using an atomic-force-microscope (AFM) nanoelectrode potential probe that rests on the catalyst surface.[20–22] We find that the catalyst potential increases to a value sufficient to drive the photocurrent at all applied potentials studied; CoPi collects photogenerated holes from the illuminated $BiVO_4$ and drives the OER.

Results

We first studied thin $BiVO_4$ electrodes, prepared via spin coating from a solution of 0.026 M bismuth (III) nitrate and vanadyl acetylacetonate,[23] in acetylacetone. Each layer was spun onto a fluorine-doped tin oxide (FTO) conductive glass slide and annealed at 500 ºC for 10 min. Thin $BiVO_4$ electrodes were imaged with scanning electron microscopy (SEM) and AFM (Figure 5.1a, c and e). Complete experimental procedures are in Appendix C.

Illuminated cyclic voltammograms (CVs, Figure 5.2a) of the bare $BiVO_4$ in pH 6.9 potassium phosphate buffer (KPi) showed poor performance. Upon photodepositing a thin layer of CoPi on the electrode surface, a dramatic enhancement in the photoactivity was observed. We attempted to measure the potential of the catalyst layer using a nanoelectrode AFM probe,[22] but failed to achieve reproducible electrical contact with the thin CoPi layer. Thicker CoPi layers were deposited, but these led to a dramatic decay of the illuminated device performance (Figure 5.2a), with marked increases in dark current.

Based on our previous related work on hematite,[24] this result suggests that CoPi is shunting to the FTO via holes in the $BiVO_4$ film.

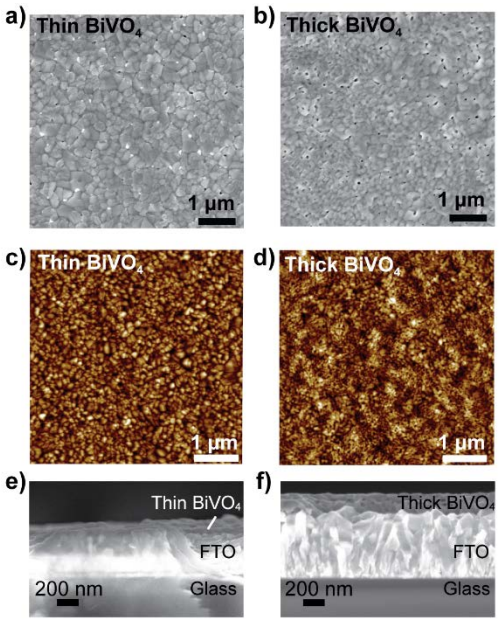

Figure 5.1. Physical characterization of $BiVO_4$ electrodes. Top down SEM images for thin and thick $BiVO_4$ (a, b). Topography measured via tapping mode AFM of thin and thick $BiVO_4$ (c, d). The root mean square roughness is 6.2 ± 0.2 nm for thin $BiVO_4$ and 6.1 ± 0.2 nm for thick $BiVO_4$. AFM images have a height scale of 40 nm. Cross-sectional SEM images for thin and thick $BiVO_4$ (e, f). The images show a ~50 nm and ~200 nm $BiVO_4$ thickness for the thin and thick film, respectively.

The proposed model for the shunting phenomena is shown in Figure 5.2b. For low CoPi loading the thin catalyst sparsely coats the surface and is not well interconnected (Figure 5.2b, top). The PEC performance increases compared to the bare semiconductor, as the CoPi can collect holes from the $BiVO_4$ and drive water oxidation. As more CoPi is deposited, exposed regions of FTO between $BiVO_4$ grains become filled with CoPi and the catalyst transitions from small, isolated domains to a coalesced film (Figure 5.2b, bottom). Because oxidized CoPi is composed of CoOOH, which is electrically conductive,[22,25,26] photogenerated holes injected into the CoPi from the $BiVO_4$ can recombine with electrons in the FTO. Consistent with this picture, we see evidence of direct oxidation/reduction of the CoPi at ~ 0.3 V vs ε_{O_2/OH^-} via the FTO in the dark voltammetry data for the thin $BiVO_4$ film with high catalyst loading (Figure 5.2a).

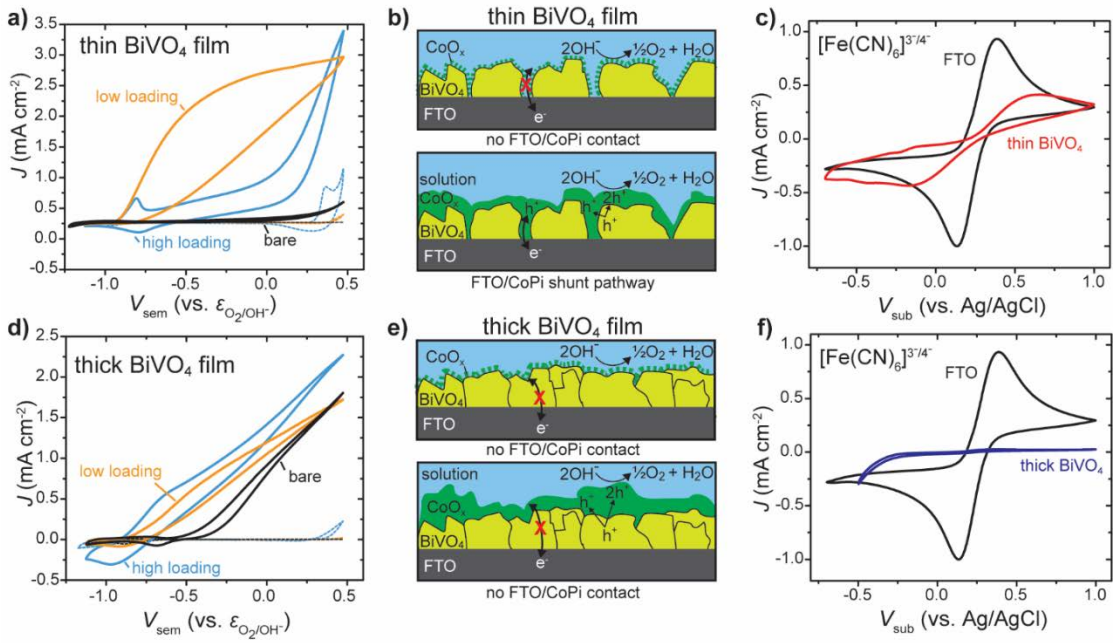

Figure 5.2. Impact of $BiVO_4$ thickness and CoPi loading on activity. (a) Low CoPi loading (yellow, 0.3 mC cm^{-2} reduction wave integration) on thin $BiVO_4$ results in a dramatic improvement in OER activity compared to the bare semiconductor (black). Additional CoPi quickly degrades performance (blue, 2.7 mC cm^{-2} integration). Dark CV's are shown with dashed lines. (b) For thin films of $BiVO_4$ with low CoPi loading, the catalyst does not significantly shunt to the underlying FTO (top), whereas at high loadings the catalyst is in contact with both the $BiVO_4$ and the FTO (bottom). (c) Dark CVs of bare FTO (black) and thin $BiVO_4$ (red) in a 10 mM ferri/ferrocyanide solution with 0.1 M KCl supporting electrolyte. (d) Cyclic voltammetry for the thick $BiVO_4$ shows that high catalyst loadings enhance OER to a greater extent than lower catalyst loadings (high loading and low loading samples shown have CoPi reduction-wave integrations of 1.1 mC cm^{-2} and are 5.3 mC cm^{-2}, respectively). (e) For thick $BiVO_4$ films, it does not matter if the catalyst has low (top) or high (bottom) loading, the shunt pathway is blocked. (f) CVs for thick $BiVO_4$ (purple) in a 10 mM ferri/ferrocyanide solution pass negligible current, consistent with a lack of pinholes. In panels (a) and (d) the electrodes were back illuminated with a 405-nm light source at a power of 27 mW cm^{-2} (calibrated using a GaP photodiode to provide the same photocurrent as 100 mW cm^{-2} of AM 1.5 illumination).

To further test the shunting hypothesis, we collected dark CV data in 10 mM ferri/ferrocyanide solution to assess the coverage of the FTO substrate by the $BiVO_4$ film (Figure 5.2c). On bare FTO, a reversible redox wave of ferri/ferrocyanide is observed. For the thin $BiVO_4$ (in the dark) a reversible wave is also observed, although smaller in height. This indicates a fraction of the underlying FTO remains exposed after the thin

$BiVO_4$ film is deposited. We also compared electrically conductive spun coat $Ni_{0.8}Fe_{0.2}O_x$ catalyst with electrically insulating $Ni_{0.5}Fe_{0.5}O_x$ on thin $BiVO_4$ (see Figure A.C.1). While insulating $Ni_{0.5}Fe_{0.5}O_x$ resulted in reasonable PEC response; $Ni_{0.8}Fe_{0.2}O_x$ on $BiVO_4$ performed poorly as the holes injected in the catalyst are presumably conducted to the supporting FTO electrode. This data is consistent with what we observed for hematite[24] and could explain the results from Kim *et al.* showing that an insulating layer of FeOOH topped with OER-active Ni(Fe)OOH on porous $BiVO_4$ enabled efficient devices.[15]

To prevent shunting in the presence of thick CoPi layers (that we hypothesized would enable the nanoelectrode potential measurement) we prepared thicker $BiVO_4$ films on FTO.[27] A precursor solution of 0.05 M bismuth (III) nitrate and 0.05 M vanadyl acetylacetonate in acetylacetone and acetic acid was spun coated on FTO and heated at 450 ºC for 15 min after each spin coating cycle (Figure 5.1 b, d). This resulted in ~200-nm-thick films (Figure 5.1f); four times thicker than the thin $BiVO_4$ (Figure 5.1c). Voltammetry of the thick $BiVO_4$ in ferri/ferrocyanide solution passes little current in the dark (Figure 5.2f), indicating complete coverage of the underlying FTO (Figure 5.2e). As a result, both low and high CoPi loadings on the thick $BiVO_4$ improve PEC performance compared to the bare electrode (Figure 5.2 d, e). Furthermore, higher loadings of CoPi yield better photoelectrode performance (Figure A.C.2), consistent with CoPi collecting holes from $BiVO_4$ and driving water oxidation.

Other strategies could also be implemented to eliminate the shunting pathway, such as blocking layers. Bard and coworkers demonstrated that an amorphous TiO_2 layer could be electrodeposited in regions where the supporting conductive substrate was exposed.[28] This improved performance by preventing oxidized reaction products evolving from the $BiVO_4$ from being reduced by the supporting conductive oxide. Similarly, others have shown that a thin layer of SnO_2 between the FTO and $BiVO_4$ helped to reduce charge recombination at the interface.[29,30] While these studies do not incorporate any OER catalysts, such blocking layers could help to prevent some of the shunting recombination we observe.

Thick $BiVO_4$, in which the catalyst cannot shunt to the underlying FTO substrate, was used as a model system to study CoPi hole collection and catalysis with potential-sensing electrochemical AFM (PS-EC-AFM).[22] Building upon dual-working-electrode voltammetry techniques we developed,[31–33] PS-EC-AFM enables direct observation of the catalyst electrochemical potential, *in operando*, independent of the semiconductor substrate. The $BiVO_4$ photoelectrode was mounted in a custom electrochemical cell that allowed for back illumination and simultaneous AFM imaging. A CoPi film was photoelectrodeposited (until the nominal $Co^{2+/3+}$ reduction wave reached an integrated charge of 6.6 mC cm^{-2}) onto the mounted $BiVO_4$ electrode. The electrolyte was switched to fresh 0.1 M pH 6.9 phosphate buffer. The nanoelectrode AFM probe was brought into contact and scanned over the electrode surface to record a topology map (Figure A.C.3). A representative location was selected and the probe was held in contact with ~ 25 nN of applied force. This provides enough force to maintain consistent electrical contact without damaging the catalyst film. The potential of the $BiVO_4$ electrode (V_{sub}) was then stepped anodically via WE1 (attached to the FTO) while illuminated with 27 mW cm^{-2} of 405-nm light. The nanoelectrode probe concurrently measured the surface potential of the CoPi layer (V_{tip}). The CoPi potential was unchanged until the $BiVO_4$ potential was stepped anodic of -0.75 V vs. ε_{O_2/OH^-}. At this potential photogenerated holes transfer to the CoPi, oxidizing it from the electrically insulating $Co(OH)_2$, to electrically conductive CoOOH (Figure 5.3a).[25] We directly measure the photovoltage generated by the $BiVO_4$|CoPi junction (~1.05 V) by the potential difference between that of the catalyst and that applied to the $BiVO_4$ (V_{tip} - V_{sub}). For the CoPi-coated FTO control sample (Figure 5.3b), once the catalyst is fully oxidized in the dark at V_{sub} > 0.35 V vs. ε_{O_2/OH^-} the measured potential of the CoPi (V_{tip}) matches the applied potential to the substrate, as expected.

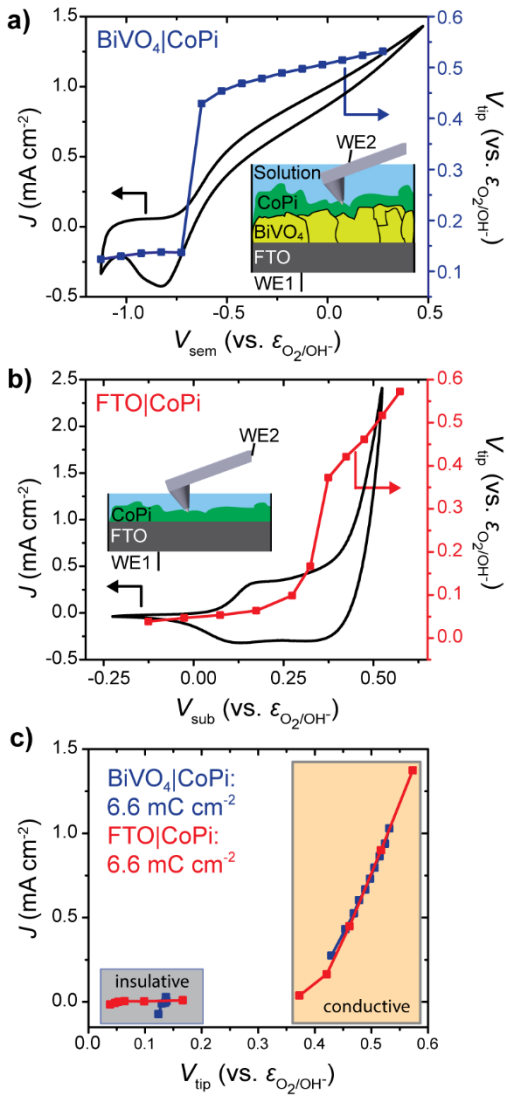

Figure 5.3. Operando PS-EC-AFM potential stepping experiments. (a) CV for CoPi-coated $BiVO_4$ (black) and the measured tip potential (V_{tip}, purple) during potential stepping, while illuminated. The inset shows the operational setup. (b) CV for CoPi coated FTO (black) and the measured tip potential (red) during potential stepping. (c) Comparison of the current (J) passed, and the CoPi surface potential (V_{tip}) measured via the nanoelectrode probe, for $BiVO_4$|CoPi (purple) under illumination and FTO|CoPi (red) in the dark. The integrated reduction wave of CoPi on both samples was the same indicating similar amounts of CoPi were loaded on the surface.

The rise in CoPi potential coincident with the onset of photocurrent demonstrates CoPi collects photogenerated holes from the $BiVO_4$. This is not however, proof that the CoPi drives the OER current at steady state. In fact, it was reported that CoPi is not

sufficiently oxidized to drive water oxidation on $BiVO_4$ based on indirect optical measurements.[17] Here we directly test if CoPi acts as an OER catalyst by comparing the CoPi potential (V_{tip}) during OER to the current that is measured through the device for both $BiVO_4$|CoPi under illumination and FTO|CoPi in the dark (Figure 5.3c). The data show that increasing currents are correlated with increasing V_{tip} in an identical fashion for both samples. In other words, the CoPi potentials measured on $BiVO_4$, for a given photocurrent density, are identical to those measured on FTO at the same current density in the dark. This demonstrates that CoPi is charged by photogenerated holes from $BiVO_4$ until it reaches sufficiently anodic potentials to drive the OER at the photocurrent density at steady state.

Conclusion

The measurements reported here show that CoPi is acting as both a hole collector and water oxidation catalyst. The loading-dependent shunting mechanism discovered for $BiVO_4$|CoPi is consistent with CoPi collecting holes from $BiVO_4$ and demonstrates the importance of controlling the semiconductor morphology to prevent direct contact between conducting substrates and electrically conducting catalysts. PS-EC-AFM enables, for the first time, the direct measurement of the catalyst potential *in operando* on $BiVO_4$ and shows that, regardless of the source of holes, CoPi drives water oxidation with the same potential dependence. This finding is consistent with measurements we made on hematite photoelectrodes, where CoPi and NiFeOOH both act as hole collectors and water oxidation catalysts.[22,34] These previous results, combined with those reported here, therefore present a consistent picture of the role of metal-(oxy)hydroxide-based catalytic surface layers in water-oxidizing oxide photoanodes. The results guide the design of enhanced photoelectrodes because they indicate that carrier collection by the catalyst and its water oxidation kinetics are both important. Tuning the interfacial charge transfer kinetics between semiconductor and catalyst (i.e. development of hole-selective catalyst contacts that allow for hole transfer but prevent the electron transfer that drives recombination), and the development of better OER catalysts will both increase the performance of an integrated photoelectrode system.

APPENDIX A

CHAPTER III SUPPLEMENTARY INFORMATION

Chapter III contains co-authored work published in volume 28 of *Nanotechnology* in 2017 (*Nanotechnology* **2017**, *28*, 095711). This work was written by myself and Huang, Z.; Chen, Y.; Mark, A.; Gödrich, S.; Stelling, C.; Jiang, J.; Poddar, R.; Li, C.; Kumar, R.; Papastavrou, G. and Retsch, M. provided experimental assistance. Brunschwig, B. S.; Xiang, C. and Boettcher, S. W provided editorial assistance.

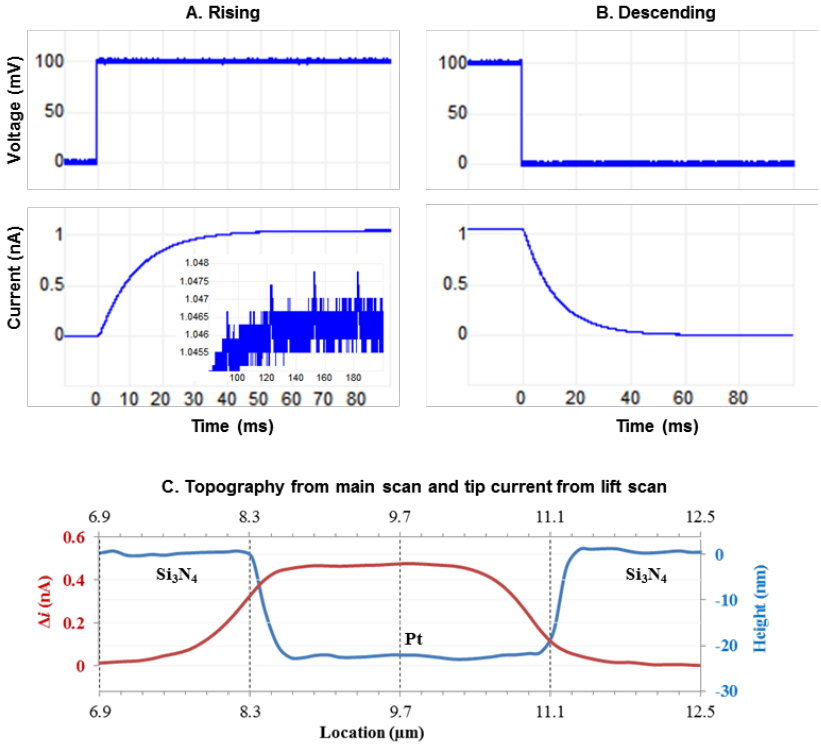

Figure A.A.1. Effect of electronic delay on data acquisition with a 32 Hz filter setting and 30 ms data averaging. (A) Rising current signals. The inset shows the noise level of < 2 pA, peak to peak. (B). Descending current signals. (C) Comparison of the topographic line profile from the main scan and the tip current from the lift scan. Retrace scan is at a tip velocity of 12 µm/s. (A) and (B) show the same 30 ms delays, (C) shows the spatial delay of the current signal. The step voltage pulse was generated by a bipotentiostat (CHI760D, CHI instrument) and the current signal was measured by the same bipotentiostat. Both the generated voltage signal and the resulting current signal were routed to the Nanoscope V controller of the AFM. The low-speed analog-to-digital

converter in this controller has a sample rate of 500 kHz and was able to capture the high-temporal resolution details as shown in (A) and (B).

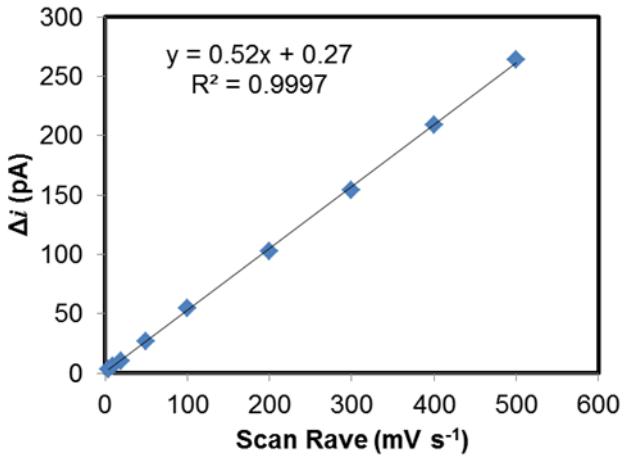

Figure A.A.2. Capacitive charging current vs CV scan rate (solid diamonds). The solid line is a linear regression of the results. The current signal was extracted and averaged from the non-faradaic region (0 to ~ 0.03 V vs Ag/AgCl) of the CV curves. Solution conditions: 5 mM $[Ru(NH_3)_6]^{3+}$, 0.1 M KNO_3. We note the capacitive current is much larger than that which would be attributed solely to the nano-tip electrode double layer capacitance. This is likely the result of ionic polarization in the protective layers that isolate the much larger areas of the conductive tip and current path, and additional stray capacitances of the measurement system.

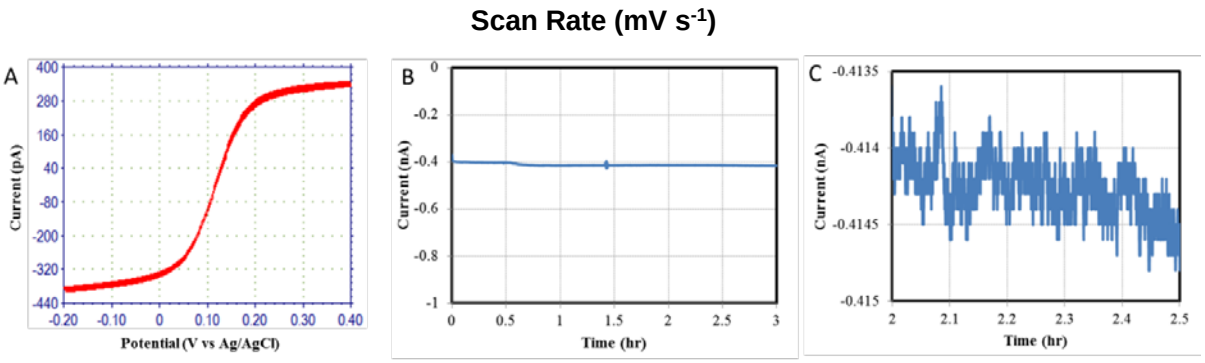

Figure A.A.3. (A) 50 CV cycles plotted together. (B) 3 hr of amperometric measurement. (C) Magnification of a section in (B) to illustrate noise levels. Solution: 5 mM / 5 mM $[Fe(CN)_6]^{4-/3-}$ in aq. 0.1 M KNO_3. Reference electrode: Ag/AgCl. The continuously-captured 50 CV cycles plotted together in (A) show no change of probe performance (no increase or decrease), The 3 hr of amperometric measurement in (B) also demonstrates the stability of the probe. The slight increase (15 pA or < 2.9%) from 32 to 44 min may be due to the drift of the reference electrode. (C) The noise level is < 2 pA over 30 min in this measurement.

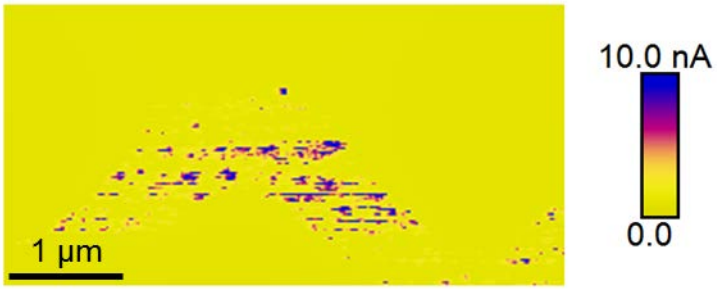

Figure A.A.4. Same image as Figure 3.7b while at a different current scale.

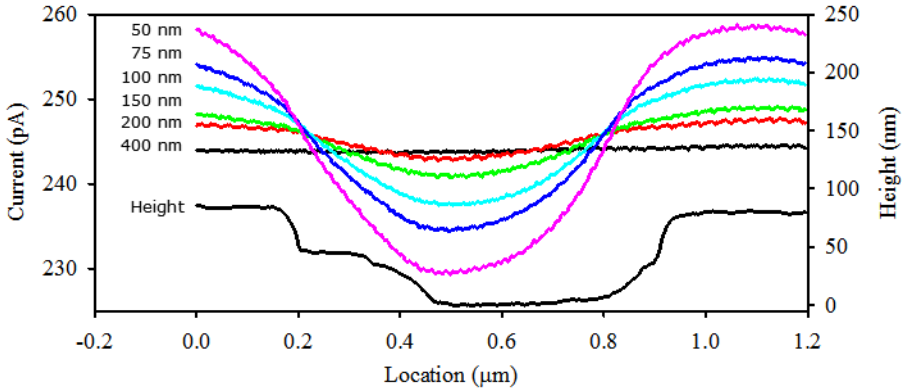

Figure A.A.5. This the same plot as Figure 3.8e with the topographic line profile added as well. The distance labels indicate the lift height. The in-hole structure (Au step inside the hole between 0.2 and 0.4 µm) as well as the electronic delays lead to the asymmetric response of the current measured with the tip lifted over the hole. As the tip is lifted away from the hole surface with increased lift height, the response becomes more symmetric.

Effect of convective transport on the measured tip current

During tip scanning, tip motion leads to convective transport of redox species to the tip surface. There are two motions that must be accounted for. During the lift scan the tip is not oscillating vertically. Therefore, there is no enhancement of the diffusion-limited current from this vibration. However, there is lateral translation. This, as shown below, is likely small.

Briefly, at steady state, the average flux to the tip is:

$$< J >= \frac{i_0}{nFS}$$

where i_0 is the diffusion limited current (1 nA), n is the moles of electrons from the balanced redox reaction (n =1), F is Faraday's constant (9.65×10^4 C/mol), and S is the surface area of the electrode (9.3×10^{-10} cm^2). $<J>$ is thus estimated to be 1.1×10^{-5} mole cm^{-2} s^{-1}.

For tip scanning in the horizontal direction, the tip velocity is small and the convective flux can be ignored. For example, for a scan size of 5 um at 0.4 Hz scan rate (Figure 3.8), the tip velocity is 4×10^{-6} m/s. This results in a flux of 4×10^{-9} mol cm^{-2} s^{-1} as estimated by the equation below with a redox species concentration of 10 mM.

$$J_{xy} = v_{tip} C_0$$

The electrochemical map was captured from the lift scan when the tip is not oscillating. Therefore, this raster tip scanning has negligible effect on the tip current.

However, in the main scan, the vertical convective flux, J_y, due to PFT tip motion, is:

$$J_y = < s > C_0 \ = 4Af C_0$$

where $<s>$ is the average speed of the tip; A and f are PFT amplitude (150 nm) and frequency (2 kHz), respectively; and C_0 is 10 mM, the bulk concentration of $[Ru(NH_3)_6]^{3+}$. J_y is estimated as 1.2×10^{-6} mole cm^{-2} s^{-1}. This is 10 times lower than $<J>$. Therefore, the vertical flux due to PFT tip motion may have a slight effect on the faradic process (in this simple approximation, which ignores convection driven by the tip structure). Consistent with this, we observed negligible effect on the diffusion limited current by comparing CV curves captured when the tip is still and when the tip PFT oscillates.

Effect of dissolved O_2 in electrolyte

The diffusion-limited current of a nanoelectrode is approximately proportional to the bulk concentration and the diffusion coefficient of the species. Therefore, the contribution of the dissolved O_2 to the tip current is:

$$q = \frac{i_{O_2}}{i_{Ru} + i_{O_2}} \sim \frac{D_{O_2}[O_2]}{D_{Ru}[Ru] + D_{O_2}[O_2]}$$

Where i_{O_2} and i_{Ru} are contribution to the tip current from dissolved O_2 and $[Ru(NH_3)_6]^{3+}$, respectively. D_{O_2} and D_{Ru} are the diffusion coefficients. $[O_2]$ and $[Ru]$ are the concentrations of these two species. The O_2 content in air-saturated pure water at 293 K is 0.26 mM.[1] The diffusion coefficient of O_2 in pure water is 1.8×10^{-5} cm^2 s^{-1}.[2] The diffusion coefficients of $[Ru(NH_3)_6]^{3+}$ in 0.1 M KCl and KNO_3 electrolyte solution are 8.4×10^{-6} cm^2 s^{-1} and 8.0×10^{-6} cm^2 s^{-1}, respectively.[3] Therefore, for 5 mM and 10 mM $Ru(NH_3)_6]^{3+}$, q are ~10% and 5%, respectively.

As all the handling is performed in the air rigorous degassing of the electrolyte solution is difficult. We only used a small volume of solution ~ 2.0 – 2.5 mL) and this was transferred in air. Further, the electrochemical cell was not sealed and measurement normally proceeded for > 30 min. Therefore, in this work (and similar to most literature reports on AFM-SECM) we did not degas the electrolyte before use. However, as reported by Mirkin et al.,[4] as oxygen can be reduced at the electrodes, degassing of the electrolytes can be important for high resolution imaging at low currents/voltages.[4] Purging the electrolytes with Ar or N_2 prior to use is therefore recommended when such information is needed.

APPENDIX B

CHAPTER IV SUPPLEMENTARY INFORMATION

Chapter IV contains co-authored work published in volume 3 of Nature Energy in 2017 (*Nat. Energy* **2018**, *3*,46−52). This work was written primarily by me. Hajibabaei, H.; Sivula, K. and Hamann, T. W. provided experimental assistance. Laskowski, F. A. L.; Qiu, J. and Boettcher S. W. provided editorial assistance.

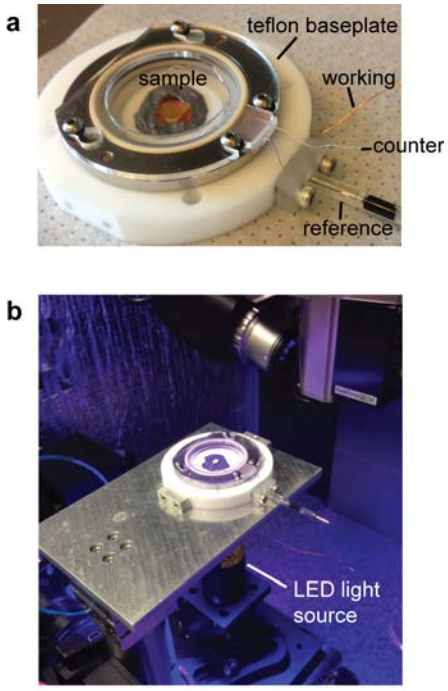

Figure A.B.1. PS-EC-AFM setup for potential sensing photoelectrochemical experiments. (a) Modified electrochemical cell for AFM. (b) Photo-illumination from the bottom of the EC cell on the AFM stage.

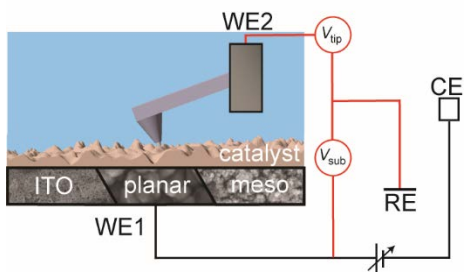

Figure A.B.2. Wiring schematic for the PS-EC-AFM. The potential of the first working electrode (WE1) was controlled relative to the reference electrode while the second working electrode (WE2) measured potentials relative to the reference electrode.

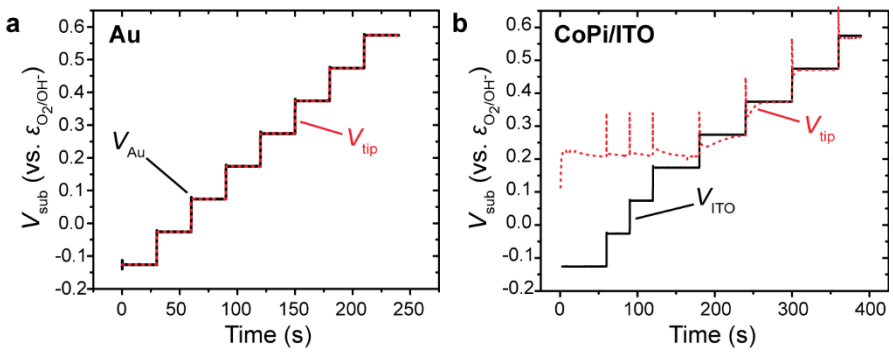

Figure A.B.3. Potential sensing on conductive substrates. (a) A bare Au electrode in potassium phosphate buffer. The black line corresponds to the potential applied at the substrate whereas the red line corresponds to the potential measured at the tip. (b) CoPi-coated ITO electrode in potassium phosphate buffer. The black line corresponds to the potential applied at the substrate whereas the red line corresponds to the potential measured at the tip resting on the CoPi. At low applied potentials the catalyst is in the non-conductive state, therefore the surface potential does not track the applied potential. At potentials greater than 0.27 V vs ε_{O_2/OH^-}, the potential measured at the tip tracks well with the applied potential. At larger applied potentials there is a slight deviation in the measured potential from the applied potential, presumably in part due to a potential drop in the catalyst layer when current is flowing to drive the oxygen evolution reaction (OER).

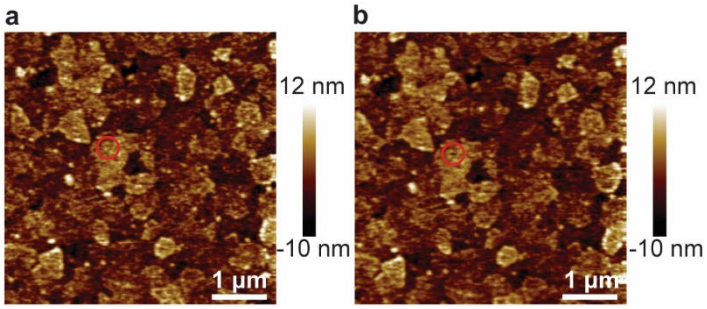

Figure A.B.4. In-Situ AFM images, collected using the nanoelectrode probe. (a) AFM image of a CoPi coated (~65 nm) ITO substrate. The center of the red circle indicates the location the probe was rested on the surface, with an applied force of ~25 nN, for 5 min using the point and shoot function on the AFM software. (b) AFM image collected after the probe was rested on the surface for 5 min, with the red circle indicating the location of the probe. Little change to the catalyst film was observed.

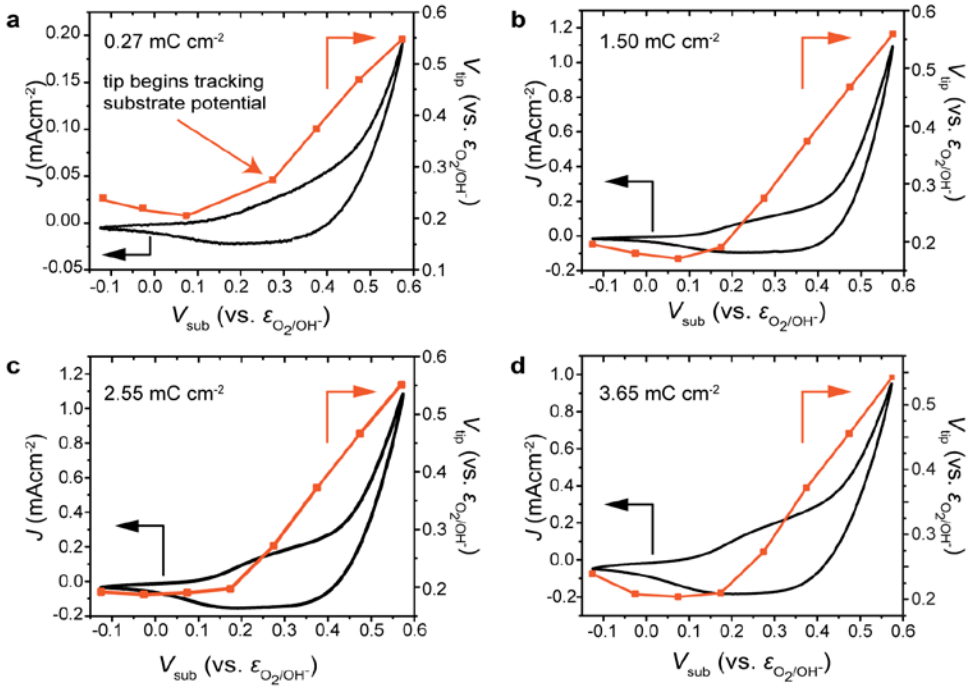

Figure A.B.5. PS-EC-AFM experiments for CoPi-coated ITO electrodes. In each case, CoPi was electrodeposited and the electrode was cycled over three cyclic voltammograms (CVs) at 20 mV s^{-1}. The integrated charge associated with the CoPi reduction wave, which is proportional to film thickness, is given in each panel. The potential was stepped anodically while the tip was in contact with the CoPi measuring the surface potential. The electrode was then returned to the deposition solution and the experiments repeated. A CV of CoPi on an ITO substrate, overlaid with a potential stepping experiment, are shown after (a) the first deposition, (b) the second deposition, (c) the third deposition, and (d) the fourth deposition.

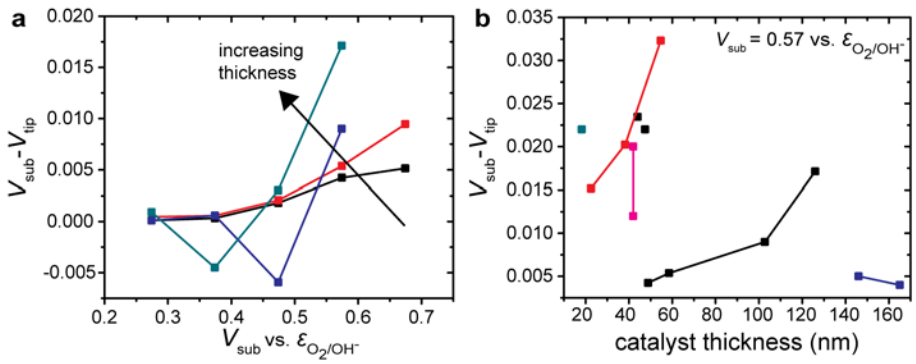

Figure A.B.6. Effect of the CoPi thickness on the potential measurements. (a) Relating the potential loss between the substrate and the tip to the current being passed through the substrate for a variety of CoPi loadings on ITO (approximate catalyst thicknesses are 49 nm, 59 nm, 103 nm and 126 nm). The trend indicates that thicker CoPi films have a greater potential loss (approximately 20 mV for thickest films). All of the data was collected using the same probe. (b) Potential loss between the substrate and the tip related to the estimated thickness of CoPi on an ITO substrate with V_{sub} = 0.57 V vs ε_{O_2/OH^-}. Data points of the same color were collected with the same probe. Data points connected with lines were collected on the same sample with varying catalyst thicknesses deposited by sequential electrodeposition steps. The pink data points are for CoOOH on Au, while all others are CoPi on ITO. Based on this dat(a) there is evidence that differences in catalyst thickness can affect the potential differences between V_{sub} and V_{tip}. The tip-sample contact resistance may also vary.

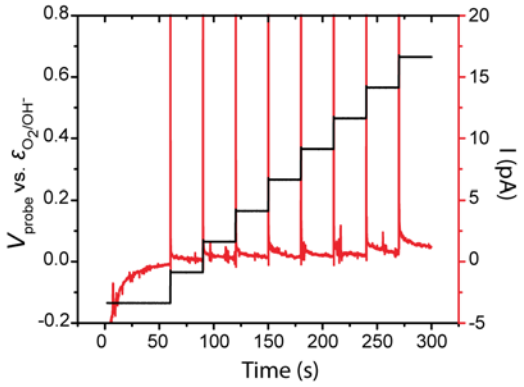

Figure A.B.7. Potential stepping *via* the Pt nano-electrode in KPi electrolyte. Potentials were stepped over the same range that the probe was used to measure. Steady-state currents were less than 2 pA. This current is negligible compared to the OER current passed by the substrate.

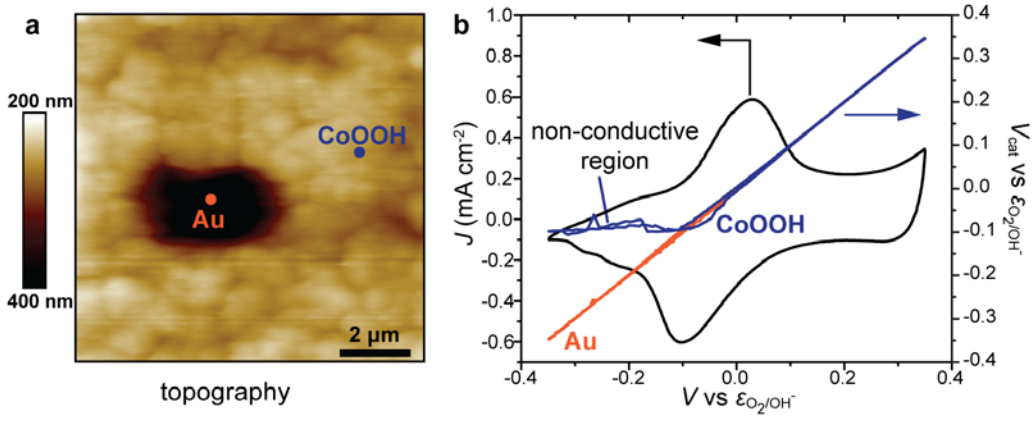

Figure A.B.8. Cobalt (oxy)hydroxide on a conductive Au substrate. (a) AFM topographic image of a pinhole in the catalyst film. (b) PS-EC-AFM results with the probe placed on Au and CoOOH (locations denoted with the dots on the AFM image). The Au (red) measured potential is identical to the applied potential of the substrate over the complete scan cycle. The CoOOH region (blue) however, only tracks the substrate potential when the catalyst is oxidized and in a conductive state (V_{sub} > -0.1 V vs ε_{O_2/OH^-}). At more negative potentials, V_{tip} reaches a constant value and no longer tracks the V_{sub}. A voltammogram for this catalyst film is also shown. We note that the depth of the hole (~500 nm) is sufficiently shallow to allow the tip to contact the bottom. For smaller holes with higher aspect ratios the width (~ 1 micron at 500 nm up from the apex) of the EC-AFM probe will limit the ability to probe the potential at the bottom of the hole. A Pt wire was used as a reference electrode for these experiments and the potentials were then approximately referenced to the thermodynamic redox potential for the OER, based on the position of the redox wave. The experiments here were performed in 0.1 M KOH. The CoOOH catalyst was electrodeposited on an Au electrode from a 0.1 M $Co(NO_3)_2$ solution dissolved in 18.2 MΩcm nanopure water by passing a current density of -2 mA cm^{-2}. The conductivity onset for this sample, measured in 0.1 M KOH, is more cathodic than that measured for CoPi in neutral electrolyte, consistent with the known electrochemical behavior of CoOOH[1].

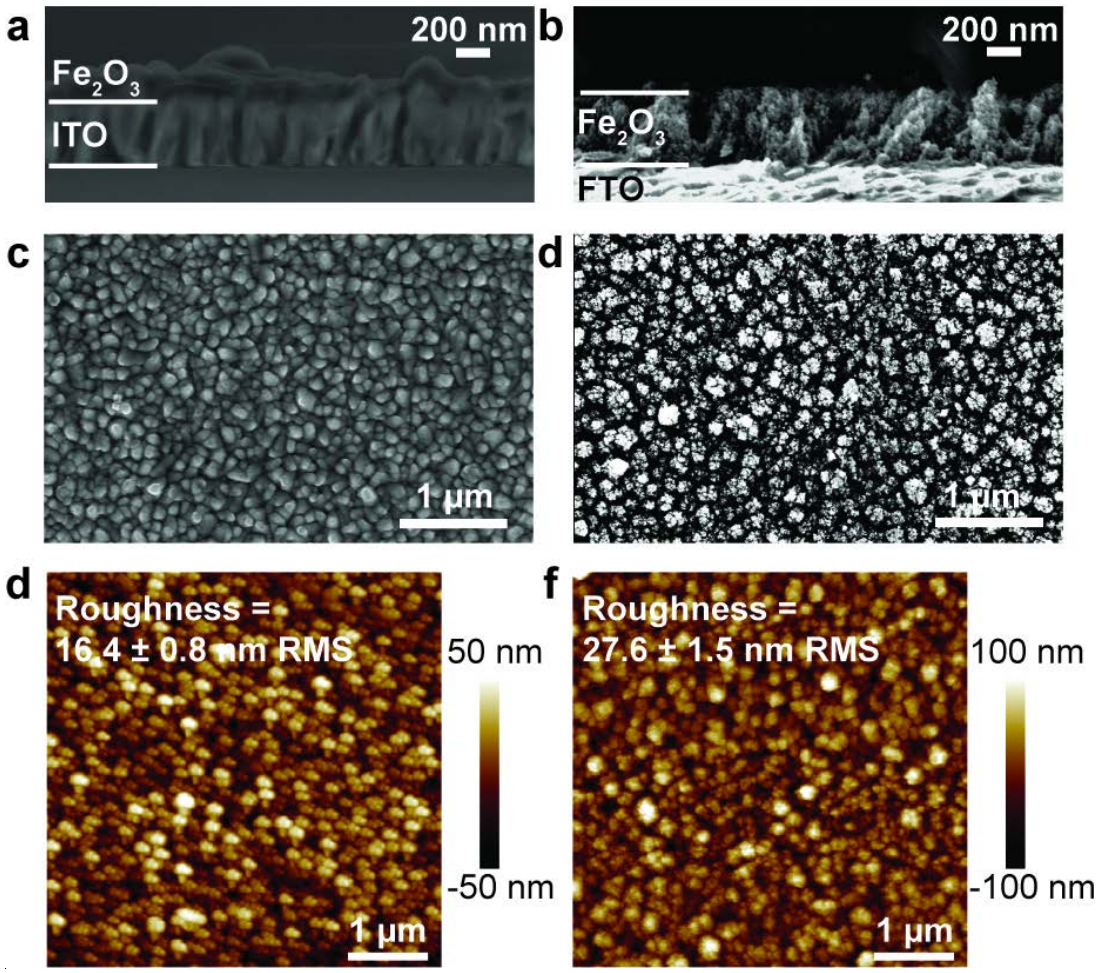

Figure A.B.9. Comparison of planar and mesostructured Fe_2O_3 photoelectrodes. Cross-sectional SEM images of planar (a) and mesostructured (b) as well as top-down SEM images of planar (c) and mesostructured (d) Fe_2O_3. Tapping mode AFM images of planar (d) and mesostructured (e) Fe_2O_3 are also shown, with an average root-mean-squared (RMS) surface roughness of 16.4 nm and 27.6 nm, respectively. AFM images were collected using tapping mode in air with Tespa-V2 probes.

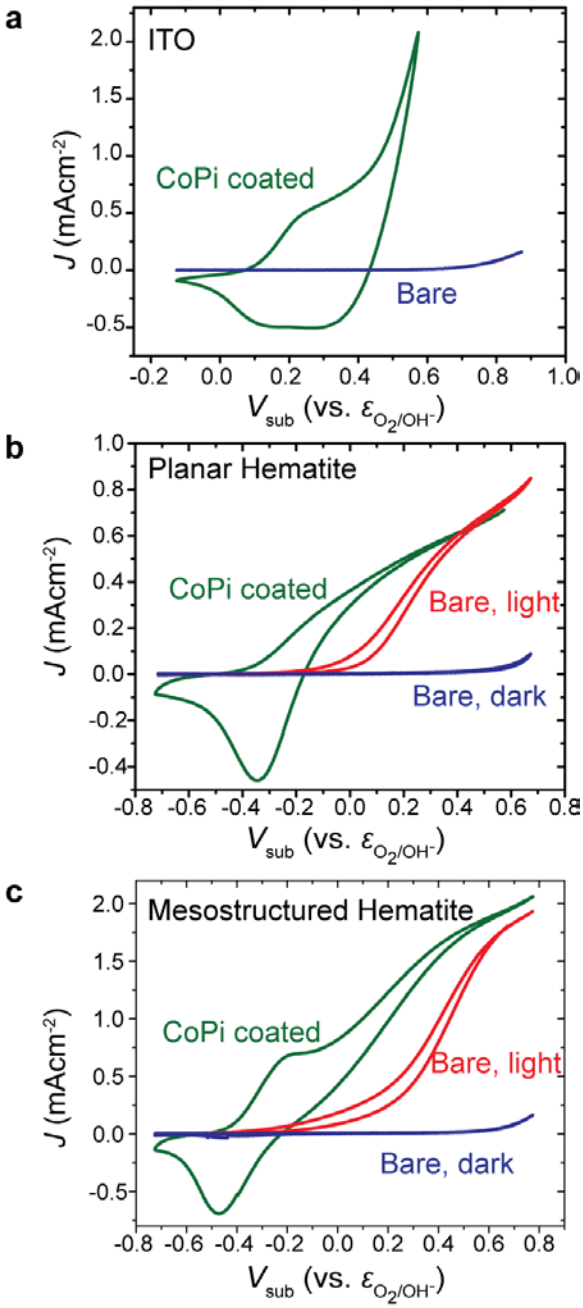

Figure A.B.10. Voltammetry for bare and CoPi-catalyzed electrodes. Results for (a) ITO, (b) planar hematite and (c) mesostructured hematite. For hematite samples, the bare electrodes are shown both under illumination and in the dark. As expected, the mesostructured samples have higher photocurrents than the thin planar hematite samples. Both hematite samples and the ITO sample show significant enhancement in performance (observed primarily by the cathodic shift in the onset potential) after the addition of the CoPi layer.

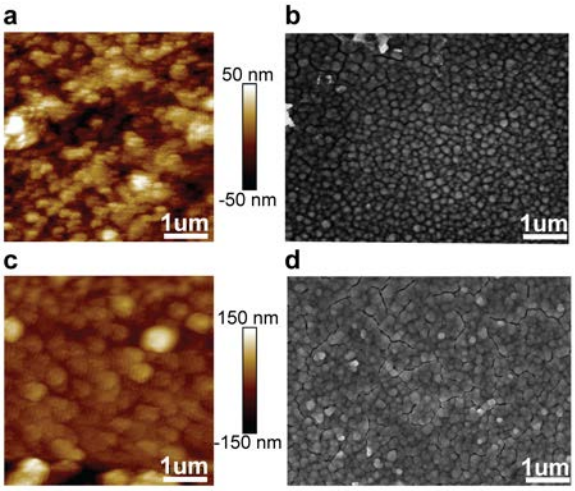

Figure A.B.11. CoPi coated hematite samples. (a) AFM image, collected *in-situ* using the nanoelectrode probe and (b) SEM image of CoPi coated planar hematite (6.9 mC cm^{-2} reduction wave integration). (c) AFM image, collected *in-situ* using the nanoelectrode probe and (d) SEM image of CoPi coated mesostructured hematite (9.1 mC cm^{-2} reduction wave integration).

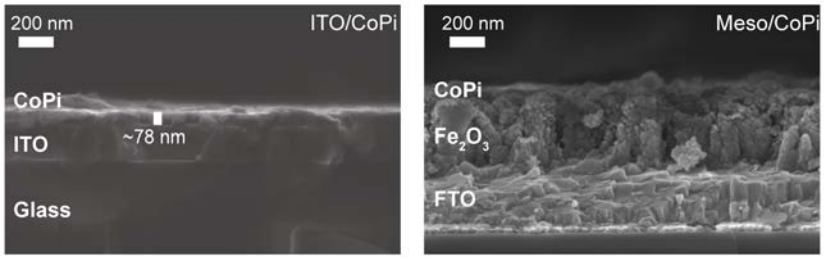

Figure A.B.12. Cross-sectional SEM images for CoPi-coated ITO (left) and CoPi coated mesostructured hematite (right). For each sample, 20 nm of Au was deposited on the sample surface to dissipate charging during imaging. The CoPi layer was 60 ± 20 nm thick on ITO. This is close to the CoPi thicknesses estimated, 80 nm on ITO, based on the integration of the reduction wave (5.4 mC cm^{-2}). A discussion on how thickness of CoPi is estimated can be found below. A CoPi layer is also visible on mesostructured hematite, however, a thickness value cannot accurately be estimated due to the highly-structured nature of the hematite. Based on the integration of the reduction wave, we estimate the film would be 110 nm thick if deposited on a smooth substrate.

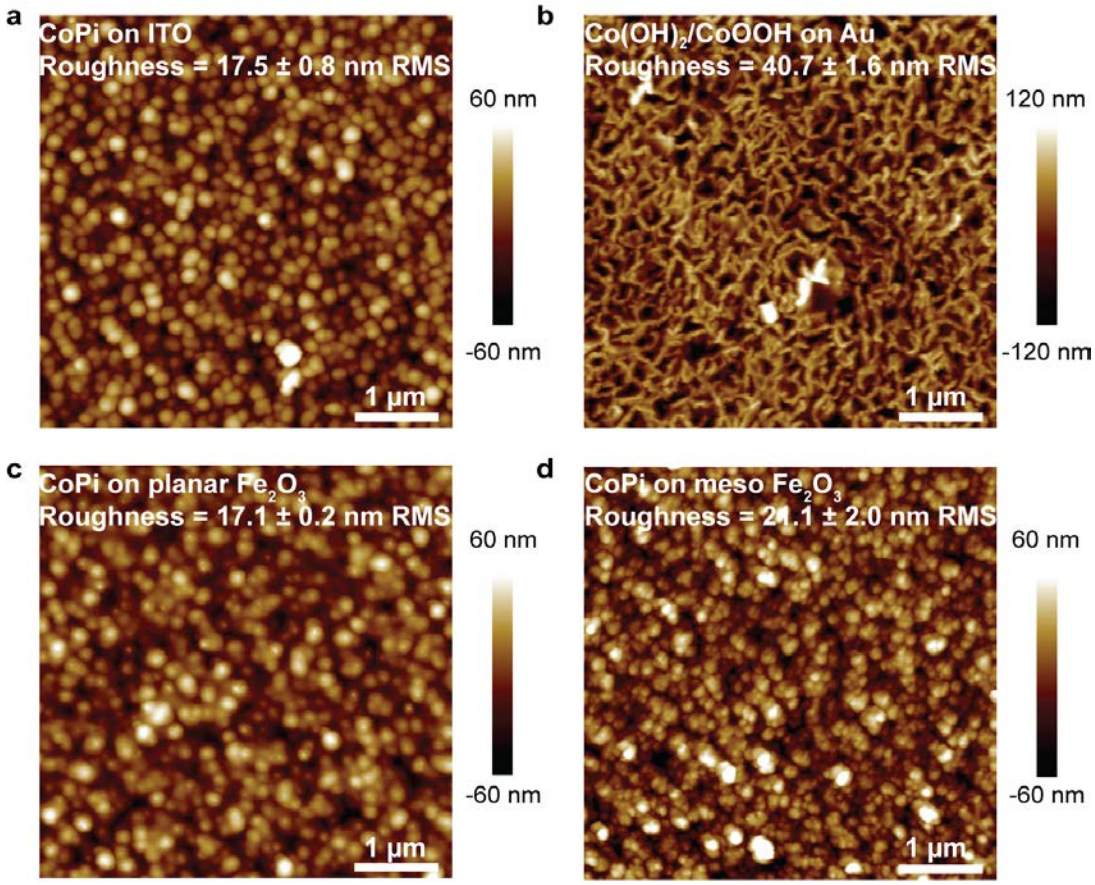

Figure A.B.13. Topographic AFM images for Co-based catalysts on different conducting and semiconducting substrates. Reported RMS roughness for (a) CoPi on ITO (b) CoOOH on Au (c) CoPi on planar Fe_2O_3 and (d) CoPi on mesostructured Fe_2O_3. In each case, images were collected in tapping mode, in air, with Tespa-V2 AFM probes. Roughness was measured at three distinct locations for each sample and the average roughness and standard deviation is reported on each image.

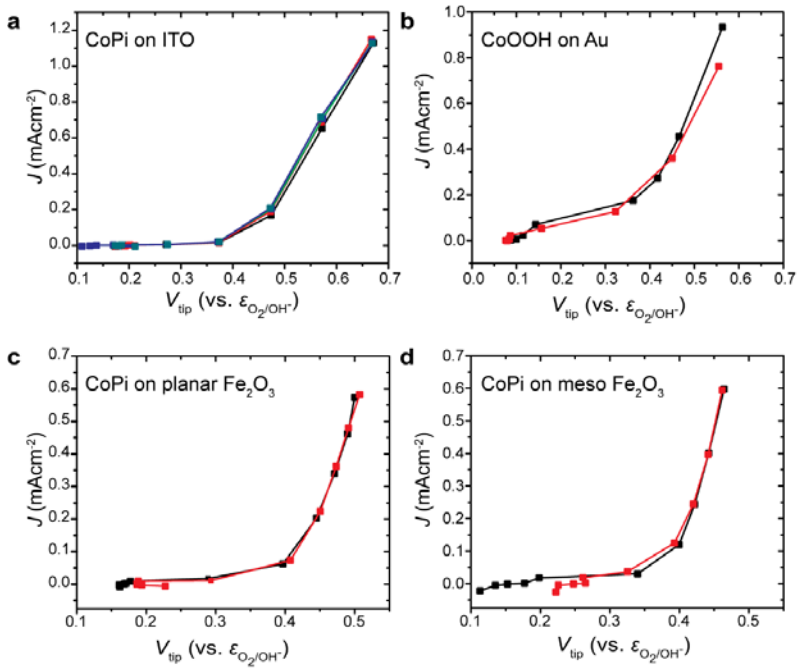

Figure A.B.14. Reproducibility of tip potentials for different catalyst/substrate systems. Current density versus catalyst potential curves for (a) CoPi on ITO (b) CoOOH on Au (c) CoPi on planar Fe_2O_3 and (d**)** CoPi on mesostructured Fe_2O_3. In each case, experiments were run in at least two locations on the same sample and yield curves that nearly superimpose on one another.

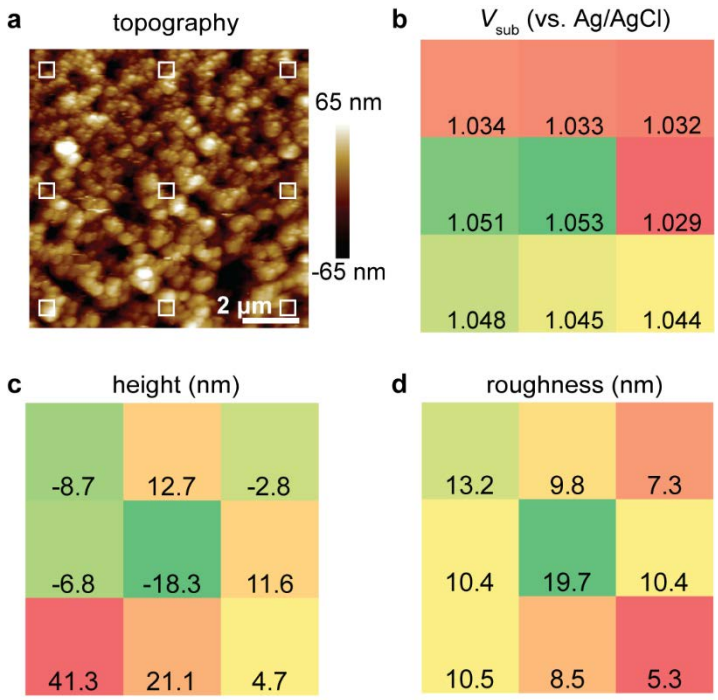

Figure A.B.15. Measuring heterogeneity for a CoPi-coated electrode in KPi electrolyte. (a) topographic image collected *via* peak force tapping imaging using the nanoelectrode probe. The area was subsequently used for "point and shoot" measurements where the probe was rested on the catalyst for 15 s to take a potential measurement of the surface while 1.1 V vs Ag/AgCl was applied to the substrate. (b) the potentials measured at the probe, corresponding to the center of each white square in **a**. Potentials varied by ~20 mV throughout the surface. (c) Average height inside each 500 nm × 500 nm white box, with the box centered on the location the probe was rested. (d) roughnesses corresponding to the area inside of the white boxes. There is no meaningful correlation between the height, roughness and the potential variation measured.

APPENDIX C

CO-PI IS A HOLE COLLECTRO AND OXYGEN EVOLUTION CATALYST ON $BiVO_4$ WATER-SPLITTING PHOTOANODES

This appendix contains co-authored unpublished work that has been submitted to *ACS Energy Letters*. This work was written primarily by me. Qiu, J.; Laskowski, F. A. L. and Toma, F. M. provided experimental assistance. Boettcher S. W. provided editorial assistance.

Experimental

Thin $BiVO_4$: Films were prepared based on a previously reported procedure.[1] In short, fluorine doped tin oxide (FTO) (~13Ω/sq, Sigma Aldrich) slides were washed with isopropanol and 18 M Ω water, dried with a nitrogen and treated with an ozone cleaner for 10 min. 15 mL of a 0.2 M solution of bismuth (III) nitrate pentahydrate (Sigma Aldrich, ≥98%) in acetylacetone (Sigma Aldrich, ≥ 99%) and 100 mL of a 0.03 M solution of vanadium(IV) oxy(acetylacetonate) in acetylacetone were prepared and sonicated for 10 min. The two solutions were combined and sonicated for 5 min. The solution was filtered through a 0.45 μm nylon filter (Thermoscientific), and dispensed onto the FTO such that the surface was coated. The substrate was then spun twice at 1000 rpm for 6 s. After this spin-coating cycle, the substrate was annealed for 10 min at 500 °C in a muffle furnace. Nine spin-coating and annealing cycles were completed, with the last annealing step lasting 2 h. The final $BiVO_4$ film thickness was approximately 50 nm (Figure 1e).

Thick $BiVO_4$: Thicker $BiVO_4$ films were prepared with small modifications to a previously reported procedure.[2] Briefly, FTO substrates (~10 Ω/sq, Techinstro,) were sonicated in acetone, then 18 M Ω water, for 5 min each. Substrates were dried with nitrogen, and heated to 450 °C for 30 min on a hotplate. Bismuth nitrate pentahydrate (Sigma Aldrich, ≥98.0%) was dissolved in acetic acid (5 mL, 0.200 M) and vanadyl acetylacetonate (Sigma Aldrich, 98%) was dissolved in acetylacetone (15 mL, 0.066 M).

The two solutions were sonicated for 10 min, combined, and sonicated for an additional 10 min.

$BiVO_4$ films were prepared by spin coating. The precursor solution was filtered through a 0.45 μm PTFE filter (VWR) such that the FTO substrate was completely coated. The substrate was spun at 1000 RPM for 20 s, removed from the spin coater, and heated at 450 °C for 15 min. The spin-coating/annealing procedure was repeated between 7 and 10 times. After the last cycle, the coated FTO was heated in a box furnace to 450 °C for 5 h.

Electrode Preparation: Electrodes were prepared by dicing $BiVO_4$/FTO and FTO substrates and electrically connecting the FTO using Sn-Cu wire and silver paint (Ted Pella, Inc.). For thick $BiVO_4$ samples, a small portion of the $BiVO_4$ was etched with HCl (2 M) and electrical contact was made with the underlying FTO. The wire was run through a glass tube and epoxy was used to cover the contact and isolate the wire from solution. Electrodes used for AFM experiments were mounted on a custom Teflon baseplate using double-sided copper tape. A copper wire was electrically connected to the $BiVO_4$ and FTO samples with silver paint and covered with epoxy to isolate conductive components, leaving the substrates exposed.

(Photo)electrochemistry: Experiments were performed in 0.1 M phosphate buffer at pH 6.9, prepared with 18 MΩ water. Macroscopic electrochemistry experiments were performed in a three-neck flask while AFM experiments were performed with a modified electrochemical cell and a custom AFM illumination stage, as previously described.[3] Pt was used for a counter electrode and an Ag/AgCl electrode with a saturated KCl filling solution as the reference. All potentials are referenced to the thermodynamic potential for oxygen evolution unless otherwise noted. The conversion formula is $\mathrm{V\ vs.\ }\mathcal{E}_{O_2/OH^-} = \mathrm{V\ vs.\ }\mathcal{E}_{Ag/AgCl} + 0.197\ \mathrm{V} - 1.23\ \mathrm{V} + (0.059\ \mathrm{V} * \mathrm{pH})$. Samples were illuminated by a 405-nm light-emitting diode (ThorLabs). Light intensities were calibrated using a GaP photodiode to provide the same photocurrent on the GaP as 100 mW cm^{-2} of AM 1.5 illumination (~ 27 mW cm^{-2} at 405 nm). A broadband thermopile power meter (Melles Griot) was used to verify the light intensity. All cyclic voltammograms were collected at a scan speed of 20 mV/s, with the exception of the work in ferri/ferrocyanide solution, which was collected at 50 mV/s.

CoPi deposition: Cobalt oxyhydroxide phosphate was deposited from a 0.1 M phosphate solution, buffered to pH 6.9, containing 0.5 mM $Co(NO_3)_2$. For $BiVO_4$ samples, CoPi was photoelectrodeposited on its surface by applying a current density of ~10 μA cm^{-2} while back illuminated with a 405-nm light-emitting diode at 27 mW cm^{-2} power. For FTO, CoPi was electrodeposited on the electrode at a current density of ~10 μA cm^{-2}. Catalyst loading was adjusted by changing deposition times and performing subsequent depositions. Loading was monitored via the integration of the reduction wave of CoPi during cyclic voltammetry.

Photochemical-metal-organic-deposited $Ni_{0.5}Fe_{0.5}O_x$ and $Ni_{0.8}Fe_{0.2}O_x$: Photochemical-metal-organic-deposited (PMOD) $Ni_{0.5}Fe_{0.5}O_x$ and $Ni_{0.8}Fe_{0.2}O_x$ preparation has been described previously.[4,5] In short, precursors of iron(III) 2-ethylhexanoate (50% in mineral spirits, Alfa Aesar), and nickel(II) 2-ethylhexanoate (78% in 2-ethylhexanoic acid, Sigma Aldrich) were used. Precursor solutions were prepared by dissolving the appropriate ratio of metal complexes in hexanes to achieve a 15% w/w solution. 200 μL of precursor solution was used to coat the thin $BiVO_4$ substrate, and the substrate was spun at 3000 rpm for 60 s. The films were irradiated under UV light (Novascan PSD Pro Series) for 70 min, and then annealed in the air at 100 °C for 1 h.

Measurements: All atomic force microscope (AFM) work was performed using a Dimension ICON AFM (Bruker). Bare $BiVO_4$ samples were imaged in tapping mode (TESPA V2 probes). Operando electrochemical experiments were performed using scanning electrochemical microscopy (SECM) probes (Bruker) and a SECM module in PeakForce tapping mode. During potential-sensing experiments, the probe was rested on the CoPi catalyst with ~25 nN force, using the “point and shoot” function of the Bruker software. (Photo)electrochemical experiments were completed using a Biologic SP-300 potentiostat, fitted with an ultra-low current cable. The counter-electrode potential-sense lead was separated from the counter electrode and attached to the AFM tip to sense potentials at the tip of the nanoelectrode probe. Potentials were stepped anodically in 50 to 100 mV intervals and held at each potential for up to 2 min, or the amount of time needed to stabilize potential readings and reach steady state currents. A Zeiss Ultra 55 SEM at 5 keV beam energy and with a 30 μm aperture was used to collect scanning electron microscopy images.

Supplementary Figures

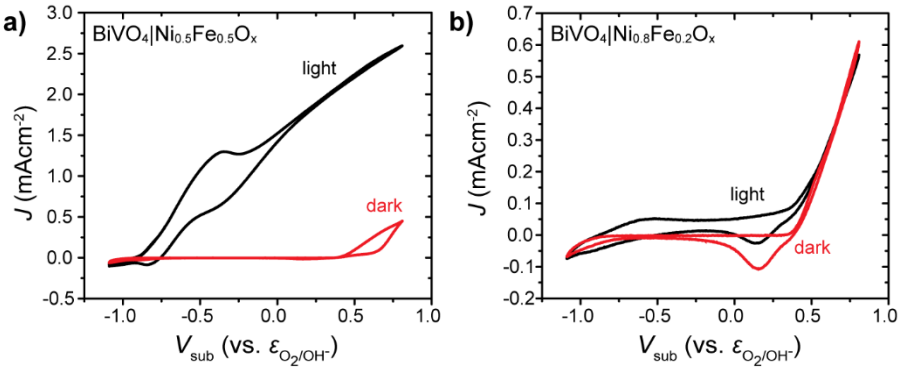

Figure A.C.1. Photoelectrochemical response of spun-coat photochemical-metal-organic-deposited $Ni_{0.5}Fe_{0.5}O_x$ (a) and $Ni_{0.8}Fe_{0.2}O_x$ (b) on thin $BiVO_4$**.** $Ni_{0.5}Fe_{0.5}O_x$ is an electrically insulating catalyst, preventing the entire thick catalyst film from being shunted to the FTO. While $Ni_{0.8}Fe_{0.2}O_x$ is known for being a superior catalyst for OER it is also electrically conducting and the illuminated cyclic voltammogram is marginally better than that in the dark. This implies that the shunting current is significant. Experiments were completed in 0.1 M potassium borate solution buffered to pH 9.2.

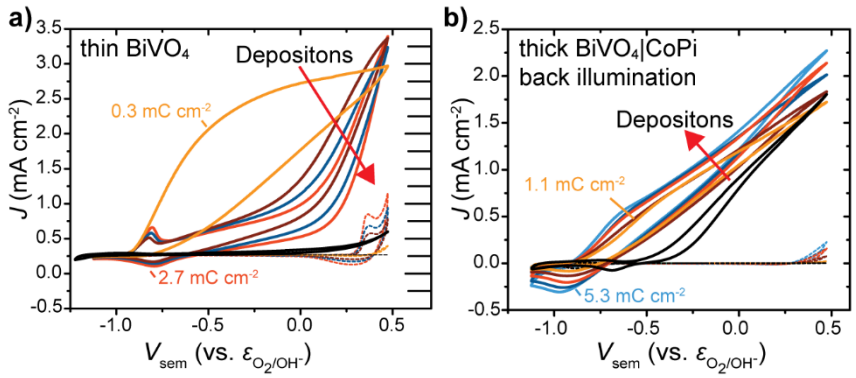

Figure A.C.2. Effects of CoPi loading on thin and thick $BiVO_4$ photoelectrochemical response. (a) Thin $BiVO_4$ with low CoPi loadings (0.3 mC/cm^2) show a significant enhancement in photoactivity under back illumination. However, with each subsequent CoPi deposition, the activity decreases. At the maximum loading shown (2.7 mC/cm^2) the photoelectrochemical response was quite poor. Dark current (dashed lines) increased with additional CoPi loading. The redox features of CoPi also become more prominent as the loading is increased. This demonstrates direct contact between CoPi and FTO for films with high loading. (b) Thick $BiVO_4$ also shows activity enhancement when loaded

with CoPi under back illumination. Additional CoPi loading further enhances activity. Dark CVs show little current at all catalyst loadings. These data indicate that the CoPi does not short to the FTO through the thick $BiVO_4$. Bare $BiVO_4$ CVs are shown in black.

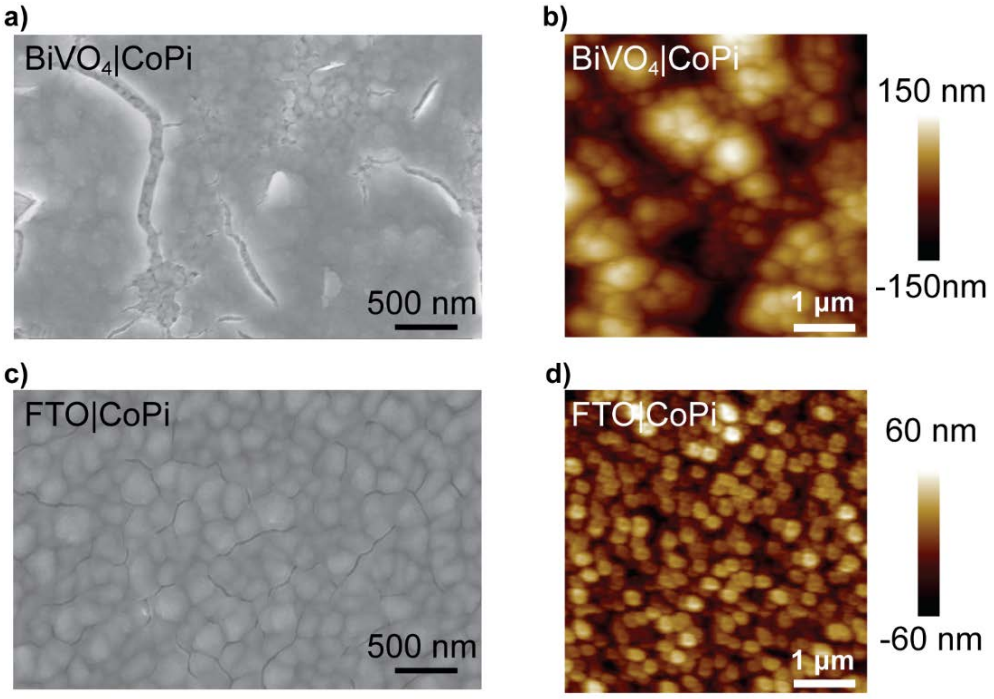

Figure A.C.3. SEM and AFM images of CoPi-loaded thick $BiVO_4$ (a, b) and CoPi loaded FTO (c, d). AFM images were collected with SECM probes in potassium phosphate electrolyte. The cracking in the films shown in the SEM images presumably occurs during drying of the samples and would not be present in the samples studied under electrochemical conditions.

REFERENCES CITED

CHAPTER I

(1) Lewis, N. S. Powering the Planet. *MRS Bull.* **2007**, *32* (10), 808–820.

(2) Trotochaud, L.; Boettcher, S. W. Precise Oxygen Evolution Catalysts: Status and Opportunities. *Scr. Mater.* **2014**, *74*, 25–32.

(3) Lin, F.; Boettcher, S. W. Adaptive Semiconductor/Electrocatalyst Junctions in Water-Splitting Photoanodes. *Nat. Mater.* **2014**, *13*, 81–86.

(4) Gamelin, D. R. Water Splitting: Catalyst or Spectator? *Nat. Chem.* **2012**, *4* (12), 965–967.

(5) Klahr, B. M.; Gimenez, S.; Fabregat-Santiago, F.; Bisquert, J.; Hamann, T. W. Photoelectrochemical and Impedance Spectroscopic Investigation of Water Oxidation with "Co-Pi"-Coated Hematite Electrodes. *J. Am. Chem. Soc.* **2012**, *134*, 16693–16700.

(6) Barroso, M.; Cowan, A. J.; Pendlebury, S. R.; Grätzel, M.; Klug, D. R.; Durrant, J. R. The Role of Cobalt Phosphate in Enhancing the Photocatalytic Activity of α-Fe_2O_3 toward Water Oxidation. *J. Am. Chem. Soc.* **2011**, *133*, 14868–14871.

(7) Barroso, M.; Mesa, C. A; Pendlebury, S. R.; Cowan, A. J.; Hisatomi, T.; Sivula, K.; Grätzel, M.; Durrant, J. R. Dynamics of Photogenerated Holes in Surface Modified α-Fe_2O_3 Photoanodes for Solar Water Splitting. *Proc. Natl. Acad. Sci. U. S. A.* **2012**, *109*, 15640–15645.

(8) Ma, Y.; Kafizas, A.; Pendlebury, S. R.; Le Formal, F.; Durrant, J. R. Photoinduced Absorption Spectroscopy of CoPi on $BiVO_4$: The Function of CoPi during Water Oxidation. *Adv. Funct. Mater.* **2016**, *26* (27), 4951–4960.

(9) Zachäus, C.; Abdi, F. F.; Peter, L. M.; van de Krol, R. Photocurrent of $BiVO_4$ Is Limited by Surface Recombination, Not Surface Catalysis. *Chem. Sci.* **2017**, *8*, 3712–3719.

(10) Carroll, G. M.; Zhong, D. K.; Gamelin, D. R. Mechanistic Insights into Solar Water Oxidation by Cobalt-Phosphate-Modified α-Fe_2O_3 Photoanodes. *Energy Environ. Sci.* **2015**, *8* (2), 577–584.

(11) Carroll, G. M.; Gamelin, D. R. Kinetic Analysis of Photoelectrochemical Water Oxidation by Mesostructured Co-Pi/α-Fe_2O_3 Photoanodes. *J. Mater. Chem. A* **2016**, *4*, 2986–2994.

CHAPTER II

(1) Peter, L. M.; Wijayantha, K. G. U. Photoelectrochemical Water Splitting at Semiconductor Electrodes: Fundamental Problems and New Perspectives. *ChemPhysChem* **2014**, *15*, 1983-1995.

(2) Gamelin, D. R. Water Splitting: Catalyst or Spectator? *Nat. Chem.* **2012**, *4*, 965-967.

(3) Liu, R.; Zheng, Z.; Spurgeon, J.; Yang, X. G. Enhanced Photoelectrochemical Water-Splitting Performance of Semiconductors by Surface Passivation Layers. *Energy Environ. Sci.* **2014**, *7*, 2504-2517.

(4) Zhong, D. K.; Choi, S.; Gamelin, D. R. Near-Complete Suppression of Surface Recombination in Solar Photoelectrolysis by "Co-Pi" Catalyst-Modified W:$BiVO_4$. *J. Am. Chem. Soc.* **2011**, *133*, 18370-18377.

(5) Barroso, M.; Mesa, C. A.; Pendlebury, S. R.; Cowan, A. J.; Hisatomi, T.; Sivula, K.; Gratzel, M.; Klug, D. R.; Durrant, J. R. Dynamics of Photogenerated Holes in Surface Modified a-Fe_2O_3 Photoanodes for Solar Water Splitting. *Proc. Natl. Acad. Sci. U. S. A.* **2012**, *109*, 15640-15645.

(6) Le Formal, F.; Pendlebury, S. R.; Cornuz, M.; Tilley, S. D.; Gratzel, M.; Durrant, J. R. Back Electron-Hole Recombination in Hematite Photoanodes for Water Splitting. *J. Am. Chem. Soc.* **2014**, *136*, 2564-2574.

(7) Trotochaud, L.; Mills, T. J.; Boettcher, S. W. An Optocatalytic Model for Semiconductor–Catalyst Water-Splitting Photoelectrodes Based on In Situ Optical Measurements on Operational Catalysts. *J. Phys. Chem. Lett.* **2013**, *4*, 931-935.

(8) Du, C.; Yang, X.; Mayer, M. T.; Hoyt, H.; Xie, J.; McMahon, G.; Bischoping, G.; Wang, D. Hematite-Based Water Splitting with Low Turn-On Voltages. *Angew. Chem., Int. Ed.* **2013**, *52*, 12692-12695.

(9) Young, K. M. H.; Hamann, T. W. Enhanced Photocatalytic Water Oxidation Efficiency with $Ni(OH)_2$ Catalysts Deposited on a-Fe_2O_3 via ALD. *Chem. Commun.* **2014**, *50*, 8727-8730.

(10) Carroll, G. M.; Zhong, D. K.; Gamelin, D. R. Mechanistic Insights into Solar Water Oxidation by Cobalt-Phosphate-Modified a-Fe_2O_3 Photoanodes. *Energy Environ. Sci.* **2015**, *8*, 577-584.

(11) Kim, T. W.; Choi, K. S. Nanoporous $BiVO_4$ Photoanodes with Dual-Layer Oxygen Evolution Catalysts for Solar Water Splitting. *Science* **2014**, *343*, 990-994.

(12) Huang, Z.; Lin, Y.; Xiang, X.; Rodriguez-Cordoba, W.; McDonald, K. J.; Hagen, K. S.; Choi, K.-S.; Brunschwig, B. S.; Musaev, D. G.; Hill, C. L.; Wang, D.; Lian, T. In Situ Probe of Photocarrier Dynamics in Water-Splitting Hematite (a-Fe_2O_3) Electrodes. *Energy Environ. Sci.* **2012**, *5*, 8923-8926.

(13) Klahr, B.; Gimenez, S.; Fabregat-Santiago, F.; Bisquert, J.; Hamann, T. W. Photoelectrochemical and Impedance Spectroscopic Investigation of Water Oxidation with "Co-Pi"-Coated Hematite Electrodes. *J. Am. Chem. Soc.* **2012**, *134*, 16693-16700.

(14) Walter, M. G.; Warren, E. L.; McKone, J. R.; Boettcher, S. W.; Mi, Q.; Santori, E. A.; Lewis, N. S. Solar Water Splitting Cells. *Chem. Rev.* **2010**, *110*, 6446-6473.

(15) Sivula, K. Metal Oxide Photoelectrodes for Solar Fuel Production, Surface Traps, and Catalysis. *J. Phys. Chem. Lett.* **2013**, *4*, 1624-1633.

(16) Hu, S.; Lewis, N. S.; Ager, J. W.; Yang, J.; McKone, J. R.; Strandwitz, N. C. Thin-Film Materials for the Protection of Semiconducting Photoelectrodes in Solar-Fuel Generators. *J. Phys. Chem. C* **2015**, *119*, 24201-24228.

(17) Lin, F.; Bachman, B. F.; Boettcher, S. W. Impact of Electrocatalyst Activity and Ion Permeability on Water-Splitting Photoanodes. *J. Phys. Chem. Lett.* **2015**, *6*, 2427-2433.

(18) Burke, M. S.; Enman, L. J.; Batchellor, A. S.; Zou, S.; Boettcher, S. W. Oxygen Evolution Reaction Electrocatalysis on Transition Metal Oxides and (Oxy)hydroxides: Activity Trends and Design Principles. *Chem. Mater.* **2015**, *27*, 7549-7558.

(19) Trotochaud, L.; Ranney, J. K.; Williams, K. N.; Boettcher, S. W. Solution-Cast Metal Oxide Thin Film Electrocatalysts for Oxygen Evolution. *J. Am. Chem. Soc.* **2012**, *134*, 17253-17261.

(20) Louie, M. W.; Bell, A. T. An Investigation of Thin-Film Ni–Fe Oxide Catalysts for the Electrochemical Evolution of Oxygen. *J. Am. Chem. Soc.* **2013**, *135*, 12329-12337.

(21) Friebel, D.; Louie, M. W.; Bajdich, M.; Sanwald, K. E.; Cai, Y.; Wise, A. M.; Cheng, M.-J.; Sokaras, D.; Weng, T.-C.; Alonso-Mori, R.; Davis, R. C.; Bargar, J. R.; Nørskov, J. K.; Nilsson, A.; Bell, A. T. Identification of Highly Active Fe Sites in (Ni,Fe)OOH for Electrocatalytic Water Splitting. *J. Am. Chem. Soc.* **2015**, *137*, 1305-1313.

(22) Trotochaud, L.; Young, S. L.; Ranney, J. K.; Boettcher, S. W. Nickel-Iron Oxyhydroxide Oxygen-Evolution Electrocatalysts: The Role of Intentional and Incidental Iron Incorporation. *J. Am. Chem. Soc.* **2014**, *136*, 6744-6753.

(23) Batchellor, A. S.; Boettcher, S. W. Pulse-Electrodeposited Ni–Fe (Oxy)hydroxide Oxygen Evolution Electrocatalysts with High Geometric and Intrinsic Activities at Large Mass Loadings. *ACS Catal.* **2015**, *5*, 6680-6689.

(24) Burke, M. S.; Kast, M. G.; Trotochaud, L.; Smith, A. M.; Boettcher, S. W. Cobalt-Iron (Oxy)hydroxide Oxygen Evolution Electrocatalysts: The Role of

Structure and Composition on Activity, Stability, and Mechanism. *J. Am. Chem. Soc.* **2015**, *137*, 3638-3648.

(25) Klingan, K.; Ringleb, F.; Zaharieva, I.; Heidkamp, J.; Chernev, P.; Gonzalez-Flores, D.; Risch, M.; Fischer, A.; Dau, H. Water Oxidation by Amorphous Cobalt-Based Oxides: Volume Activity and Proton Transfer to Electrolyte Bases. *ChemSusChem* **2014**, *7*, 1301-1310.

(26) Bediako, D. K.; Lassalle-Kaiser, B.; Surendranath, Y.; Yano, J.; Yachandra, V. K.; Nocera, D. G. Structure–Activity Correlations in a Nickel–Borate Oxygen Evolution Catalyst. *J. Am. Chem. Soc.* **2012**, *134*, 6801-6809.

(27) Farrow, C. L.; Bediako, D. K.; Surendranath, Y.; Nocera, D. G.; Billinge, S. J. L. Intermediate-Range Structure of Self-Assembled Cobalt-Based Oxygen-Evolving Catalyst. *J. Am. Chem. Soc.* **2013**, *135*, 6403-3406.

(28) Simon, P.; Gogotsi, Y. Materials for Electrochemical Capacitors. *Nat. Mater.* **2008**, *7*, 845-854.

(29) McKeown, D. A.; Hagans, P. L.; Carette, L. P. L.; Russell, A. E.; Swider, K. E.; Rolison, D. R. Structure of Hydrous Ruthenium Oxides: Implications for Charge Storage. *J. Phys. Chem. B* **1999**, *103*, 4825-4832.

(30) Nielander, A. C.; Shaner, M. R.; Papadantonakis, K. M.; Francis, S. A.; Lewis, N. S. A taxonomy for solar fuels generators. *Energy Environ. Sci.* **2015**, *8*, 16-25.

(31) Bansal, A.; Tan, M. X.; Tufts, B. J.; Lewis, N. S. Distinguishing Between Buried Semiconductor/Metal Contacts and Hybrid Semiconductor/Metal/Liquid Contacts at n-Gallium Arsenide/Potassium Hydroxide-Selenium ($Se^{-/2-}$)(aq) Junctions. *J. Phys. Chem.* **1993**, *97*, 7309-7315.

(32) Tilley, S. D.; Cornuz, M.; Sivula, K.; Graetzel, M. Light-Induced Water Splitting with Hematite: Improved Nanostructure and Iridium Oxide Catalysis. *Angew. Chem. Int. Ed.* **2010**, *49*, 6405-6408.

(33) Lin, F.; Walker, E. M.; Lonergan, M. C. Photochemical Doping of an Adaptive Mix-Conducting p-n Junction. *J. Phys. Chem. Lett.* **2010**, *1*, 720-723.

(34) Reiss, H. Photocharacteristics for Electrolyte-Semiconductor Junctions. *J. Electrochem. Soc.* **1978**, *125*, 937-949.

(35) Miller, E. L.; Rocheleau, R. E.; Deng, X. M. Design Considerations for a Hybrid Amorphous Silicon/Photoelectrochemical Multijunction Cell for Hydrogen Production. *Int. J. Hydrogen Energy* **2003**, *28*, 615-623.

(36) Surendranath, Y.; Bediako, D. K.; Nocera, D. G. Interplay of Oxygen-Evolution Kinetics and Photovoltaic Power Curves on the Construction of Artificial Leaves. *Proc. Natl. Acad. Sci. U. S. A.* **2012**, *109*, 15617-15621.

(37) Winkler, M. T.; Cox, C. R.; Nocera, D. G.; Buonassisi, T. Modeling Integrated Photovoltaic-Electrochemical Devices Using Steady-state Equivalent Circuits. *Proc. Natl. Acad. Sci. U. S. A.* **2013**, *110*, E1076-E1082.

(38) Reece, S. Y.; Hamel, J. A.; Sung, K.; Jarvi, T. D.; Esswein, A. J.; Pijpers, J. J. H.; Nocera, D. G. Wireless Solar Water Splitting Using Silicon-Based Semiconductors and Earth-Abundant Catalysts. *Science* **2011**, *334*, 645-648.

(39) Mills, T. J.; Lin, F.; Boettcher, S. W. Theory and Simulations of Electrocatalyst-Coated Semiconductor Electrodes for Solar Water Splitting. *Phys. Rev. Lett.* **2014**, *112*, 148304.

(40) Bard, A. J.; Fan, F.-R. F.; Gioda, A. S.; Nagasubramanian, G.; White, H. S. On the Role of Surface States in Semiconductor Electrode Photoelectrochemical Cells. *Faraday Discuss. Chem. Soc.* **1980**, *70*, 19-31.

(41) Lin, F.; Boettcher, S. W. Adaptive Semiconductor/Electrocatalyst Junctions in Water-Splitting Photoanodes. *Nat. Mater.* **2014**, *13*, 81-86.

(42) Barroso, M.; Cowan, A. J.; Pendlebury, S. R.; Gratzel, M.; Klug, D. R.; Durrant, J. R. The Role of Cobalt Phosphate in Enhancing the Photocatalytic Activity of a-Fe_2O_3 Toward Water Oxidation. *J. Am. Chem. Soc.* **2011**, *133*, 14868-14871.

(43) Klahr, B.; Gimenez, S.; Fabregat-Santiago, F.; Hamann, T.; Bisquert, J. Water Oxidation at Hematite Photoelectrodes: The Role of Surface States. *J. Am. Chem. Soc.* **2012**, *134*, 4294-4302.

(44) Bard, A. J.; Bocarsly, A. B.; Fan, F. R. F.; Walton, E. G.; Wrighton, M. S. The Concept of Fermi Level Pinning at Semiconductor/Liquid Junctions. Consequences for Energy Conversion Efficiency and Selection of Useful Solution Redox Couples in Solar Devices. *J. Am. Chem. Soc.* **1980**, *102*, 3671-3677.

(45) Gerischer, H. Electron-Transfer Kinetics of Redox Reactions at the Semiconductor Electrolyte Contact - A New Approach. *J. Phys. Chem.* **1991**, *95*, 1356-1359.

(46) Vanmaekelbergh, D. Direct and Surface-state Mediated Electron Transfer at Semiconductor/Electrolyte Junctions. 1. A Comparison of Steady-state Results. *Electrochim. Acta* **1997**, *42*, 1121-1134.

(47) Peter, L. M. Dynamic Aspects of Semiconductor Photoelectrochemistry. *Chem. Rev.* **1990**, *90*, 753-769.

(48) Peter, L. M.; Li, J.; Peat, R. Surface Recombination at Semiconductor Electrodes. 1. Transient and Steady-state Photocurrents. *J. Electroanal. Chem.* **1984**, *165*, 29-40.

(49) Nishida, M. A Theoretical Treatement of Charge-Transfer via Surface States at a Semiconductor-Electrolyte Interface - Analysis of the Water Photoelectrolysis Process. *J. Appl. Phys.* **1980**, *51*, 1669-1675.

(50) Carroll, G. M.; Gamelin, D. R. Kinetic Analysis of Photoelectrochemical Water Oxidation by Mesostructured Co-Pi/a-Fe_2O_3 Photoanodes. *J. Mat. Chem. A* **2016**, *4*, 2986-2994.

(51) Hu, S.; Shaner, M. R.; Beardslee, J. A.; Lichterman, M.; Brunschwig, B. S.; Lewis, N. S. Amorphous TiO_2 Coatings Stabilize Si, GaAs, and GaP Photoanodes for Efficient Water Oxidation. *Science* **2014**, *344*, 1005-1009.

(52) Smith, W. A.; Sharp, I. D.; Strandwitz, N. C.; Bisquert, J. Interfacial Band-Edge Energetics for Solar Fuels Production. *Energy Environ. Sci.* **2015**, *8*, 2851-2862.

(53) Wurfel, P.: *Physics of Solar Cells*; Wiley: Weinheim, 2009.

CHAPTER III

(1) O'Connell, M. A. & Wain, A. J. Combined electrochemical-topographical imaging: a critical review. *Anal Methods* **7**, 6983-6999 (2015).

(2) Sun, P., Laforge, F. O. & Mirkin, M. V. Scanning electrochemical microscopy in the 21st century. *Phys Chem Chem Phys* **9**, 802-823 (2007).

(3) Mirkin, M. V., Nogala, W., Velmurugan, J. & Wang, Y. X. Scanning electrochemical microscopy in the 21st century. Update 1: five years after. *Phys Chem Chem Phys* **13**, 21196-21212 (2011).

(4) Barker, A. L., Gonsalves, M., Macpherson, J. V., Slevin, C. J. & Unwin, P. R. Scanning electrochemical microscopy: beyond the solid/liquid interface. *Anal Chim Acta* **385**, 223-240 (1999).

(5) Bard, A. J., Fan, F. R. F., Kwak, J. & Lev, O. Scanning electrochemical microscopy - introduction and principles. *Anal Chem* **61**, 132-138 (1989).

(6) Sun, T., Yu, Y., Zacher, B. J. & Mirkin, M. V. Scanning electrochemical microscopy of individual catalytic nanoparticles. *Angew Chem Int Edit* **53**, 14120-14123 (2014).

(7) Kim, J., Renault, C., Nioradze, N., Arroyo-Curras, N., Leonard, K. C. & Bard, A. J. Electrocatalytic activity of individual Pt nanoparticles studied by nanoscale scanning electrochemical microscopy. *J Am Chem Soc* **138**, 8560-8568 (2016).

(8) Ludwig, M., Kranz, C., Schuhmann, W. & Gaub, H. E. Topography feedback mechanism for the scanning electrochemical microscope based on hydrodynamic-forces between tip and sample. *Rev Sci Instrum* **66**, 2857-2860 (1995).

(9) Eckhard, K. & Schuhmann, W. Alternating current techniques in scanning electrochemical microscopy (AC-SECM). *Analyst* **133**, 1486-1497 (2008).

(10) Morris, C. A., Chen, C. C. & Baker, L. A. Transport of redox probes through single pores measured by scanning electrochemical-scanning ion conductance microscopy (SECM-SICM). *Analyst* **137**, 2933-2938 (2012).

(11) Wiedemair, J., Moon, J.-S., Eaton, D. E., Mizaikoff, B. & Kranz, C. in *Micro-and nanosystems in medicine, active implants, biosensors* Vol. 25 *IFMBE Proceedings* (eds O. Dissel & W. C. Schlegel) 372-375 (2009).

(12) Knittel, P., Mizaikoff, B. & Kranz, C. Simultaneous nanomechanical and electrochemical mapping: combining peak force tapping atomic force microscopy with scanning electrochemical microscopy. *Anal Chem* **88**, 6174-6178 (2016).

(13) Eifert, A. & Kranz, C. Hyphenating atomic force microscopy. *Anal Chem* **86**, 5190-5200 (2014).

(14) Zhu, Y. Y. & Williams, D. E. Scanning electrochemical microscopic observation of a precursor state to pitting corrosion of stainless steel. *J Electrochem Soc* **144**, L43-L45 (1997).

(15) Macpherson, J. V. & Unwin, P. R. Combined scanning electrochemical-atomic force microscopy. *Anal Chem* **72**, 276-285 (2000).

(16) Kranz, C., Friedbacher, G. & Mizaikoff, B. Integrating an ultramicroelectrode in an AFM cantilever: Combined technology for enhanced information. *Anal Chem* **73**, 2491-2500 (2001).

(17) Kranz, C., Kueng, A., Lugstein, A., Bertagnolli, E. & Mizaikoff, B. Mapping of enzyme activity by detection of enzymatic products during AFM imaging with integrated SECM-AFM probes. *Ultramicroscopy* **100**, 127-134 (2004).

(18) Kueng, A., Kranz, C., Lugstein, A., Bertagnolli, E. & Mizaikoff, B. AFM-tip-integrated amperometric microbiosensors: High-resolution imaging of membrane transport. *Angew Chem Int Edit* **44**, 3419-3422 (2005).

(19) Shin, H., Hesketh, P. J., Mizaikoff, B. & Kranz, C. Batch fabrication of atomic force microscopy probes with recessed integrated ring microelectrodes at a wafer level. *Anal Chem* **79**, 4769-4777 (2007).

(20) Eifert, A., Mizaikoff, B. & Kranz, C. Advanced fabrication process for combined atomic force-scanning electrochemical microscopy (AFM-SECM) probes. *Micron* **68**, 27-35, (2015).

(21) Kranz, C. Recent advancements in nanoelectrodes and nanopipettes used in combined scanning electrochemical microscopy techniques. *Analyst* **139**, 336-352 (2014).

(22) Knittel, P., Bibikova, O. & Kranz, C. Challenges in nanoelectrochemical and nanomechanical studies of individual anisotropic gold nanoparticles. *Faraday Discuss.* **193**, 353-369 (2016).

(23) Macpherson, J. V. & Unwin, P. R. Noncontact electrochemical imaging with combined scanning electrochemical atomic force microscopy. *Anal Chem* **73**, 550-557 (2001).

(24) Kueng, A., Kranz, C., Mizaikoff, B., Lugstein, A. & Bertagnolli, E. Combined scanning electrochemical atomic force microscopy for tapping mode imaging. *Appl Phys Lett* **82**, 1592-1594 (2003).

(25) Abbou, J., Demaille, C., Druet, M. & Moiroux, J. Fabrication of submicrometer-sized gold electrodes of controlled geometry for scanning electrochemical-atomic force microscopy. *Anal Chem* **74**, 6355-6363 (2002).

(26) Dobson, P. S., Weaver, J. M. R., Holder, M. N., Unwin, P. R. & Macpherson, J. V. Characterization of batch-microfabricated scanning electrochemical-atomic force microscopy probes. *Anal Chem* **77**, 424-434 (2005).

(27) Shin, H., Hesketh, P. J., Mizaikofff, B. & Kranz, C. Development of wafer-level batch fabrication for combined atomic force-scanning electrochemical microscopy (AFM-SECM) probes. *Sensor Actuat B-Chem* **134**, 488-495 (2008).

(28) Wain, A. J., Pollard, A. J. & Richter, C. High-resolution electrochemical and topographical imaging using batch-fabricated cantilever probes. *Analytical Chemistry* **86**, 5143-5149 (2014).

(29) Akiyama, T., Gullo, M. R., de Rooij, N. F., Staufer, U., Tonin, A., Engel, A. & Frederix, P. L. T. M. Insulated conductive probes for in situ experiments in structural biology. *Aip Conf Proc* **696**, 166-171 (2003).

(30) Gullo, M. R., Frederix, P. L. T. M., Akiyama, T., Engel, A. deRooij, N. F., Staufer, U. Characterization of microfabricated probes for combined atomic force and high-resolution scanning electrochemical microscopy. *Anal Chem* **78**, 5436-5442, (2006).

(31) Morton, K. C., Derylo, M. A. & Baker, L. A. Conductive atomic force microscopy probes from pyrolyzed parylene. *J Electrochem Soc* **159**, H662-H667 (2012).

(32) Huang, Z., De Wolf, P., Poddar, R., Li, C., Mark, A., Nellist, M. R., Chen, Y., Jiang, J., Papastavrou, G., Boettcher, S. W., Xiang, C. and Brunschwig, B. S. PeakForce Scanning Electrochemical Microscopy with Nanoelectrode Probes. *Microscopy Today*, **24**, 18-25 (2016).

(33) Kaemmer, S. B. Introduction to Bruker's ScanAsyst and PeakForce tapping AFM technology. *Bruker Application Notes* **133**, 1-12 (2011).

(34) Stelling, C., Mark, A., Papastavrou, G. & Retsch, M. Showing particles their place: deterministic colloid immobilization by gold nanomeshes. *Nanoscale* **8**, 14556-14564 (2016).

(35) Retsch, M., Zhou, Z., Rivera, S., Kappl, M., Zhao, X. S., Jonas, U. & Li, Q. Fabrication of large-area, transferable colloidal monolayers utilizing self-assembly at the air/water interface. *Macromol Chem Physic* **210**, 230-241 (2009).

(36) Chen, Y. K., Sun, K., Audesirk, H., Xiang, C. X. & Lewis, N. S. A quantitative analysis of the efficiency of solar-driven water-splitting device designs based on

tandem photoabsorbers patterned with islands of metallic electrocatalysts. *Energ Environ Sci* **8**, 1736-1747 (2015).

(37) Walker, S. M., Marcano, M. C., Bender, W. M. & Becker, U. Imaging the reduction of chromium(VI) on magnetite surfaces using in situ electrochemical AFM. *Chem Geol* **429**, 60-74 (2016).

(38) Berquand, A. Quantitative imaging of living biological samples by PeakForce QNM atomic force microscopy. *Bruker Application Notes* **135**, 1-10 (2011).

(39) Berquand, A., Lafont, F., Hafner, M., Petersen, M., Schroeder, J., Landwher, S., Schwarz, J., Hyotyla, J., Lim, R. & Koenig, M. Combined optical and atomic force microscopy. *Bruker Application Notes* **138**, 1-10 (2012).

(40) Huang, Z., Drevniok, B., de Wolf, P., Dixon-Waren, J., Amster, O., Friedman, S., Pittenger, B., Li, C. & Yang, Y. Nanoscale mapping of permittivity and conductivity with scanning microwave impedance microscopy. *Bruker Application Notes* **145**, 1-10 (2016).

(41) Kaemmer, S. B. AFM and Raman Spectroscopy —Correlated imaging and tip enhanced raman scattering. *Bruker Application Notes* **139**, 1-8 (2013).

(42) Kindt, J. H. Performing enhanced multiparameter cell imaging with combined fluorescence lifetime imaging microscopy and atomic force microscopy. *Bruker Application Notes* **137**, 1-8 (2012).

(43) Li, C. PeakForce Kelvin Probe Force Microscopy. *Bruker Application Notes* **140**, 1-14 (2013).

(44) Li, C. Minne, S., Pittenger, B. & Mednick, A. Simultaneous electrical and mechanical property mapping at the nanoscale with PeakForce TUNA. *Bruker Application Notes* **132**, 1-12 (2011).

(45) Wagner, M. 10nm-Resolution infrared chemical mapping — Breaking the diffraction limit with InSpire. *Bruker Application Notes* **143**, 1-9 (2015).

(46) Bard, A. J. & Faulkner, L. R. *Electrochemical methods: fundamentals and applications*. 2 edition edn, (Wiley, 2000).

(47) Burt, D. P., Wilson, N. R., Weaver, J. M. R., Dobson, P. S. & Macpherson, J. V. Nanowire probes for high resolution combined scanning electrochemical Microscopy - Atomic force Microscopy. *Nano Lett* **5**, 639-643 (2005).

(48) Yang, Y., Lai, K., Tang, Q., Kundhikanjana, W., Kelly, M. A., Zhang, K., Shen, Z.-X. & Li, X. Batch-fabricated cantilever probes with electrical shielding for nanoscale dielectric and conductivity imaging. *J Micromech Microeng* **22**, 115040 (2012).

(49) Wain, A. J., Cox, D., Zhou, S. Q. & Turnbull, A. High-aspect ratio needle probes for combined scanning electrochemical microscopy-Atomic force microscopy. *Electrochem Commun* **13**, 78-81 (2011).

(50) Clausmeyer, J. & Schuhmann, W. Nanoelectrodes: Applications in electrocatalysis, single-cell analysis and high-resolution electrochemical imaging. *Trac-Trend Anal Chem* **79**, 46-59 (2016).

(51) Nioradze, N., Chen, R., Kim, J., Shen, M., Santhosh, P. & Amemiya, S. Origins of nanoscale damage to glass-sealed platinum electrodes with submicrometer and nanometer size. *Anal Chem* **85**, 6198-6202 (2013).

(52) Sun, T., Blanchard, P. Y. & Mirkin, M. V. Cleaning nanoelectrodes with Air Plasma. *Anal Chem* **87**, 4092-4095 (2015).

(53) Leonhardt, K., Avdic, A., Lugstein, A., Pobelov, I., Wandlowski, T., Gollas, B. & Denuault, G. Scanning electrochemical microscopy: Diffusion controlled approach curves for conical AFM-SECM tips. *Electrochem Commun* **27**, 29-33 (2013).

(54) Leonhardt, K., Avdic, A., Lugstein, A., Pobelov, I., Wandlowski, T., Wu, M., Gollas, B. & Denuault, G. Atomic force microscopy-Scanning electrochemical microscopy: Influence of tip geometry and insulation defects on diffusion controlled currents at conical electrodes. *Anal Chem* **83**, 2971-2977 (2011).

(55) Zoski, C. G., Liu, B. & Bard, A. J. Scanning electrochemical microscopy: Theory and characterization of electrodes of finite conical geometry. *Analytical Chemistry* **76**, 3646-3654 (2004).

(56) Amemiya, S., Ding, Z. F., Zhou, J. F. & Bard, A. J. Studies of charge transfer at liquid vertical bar liquid interfaces and bilayer lipid membranes by scanning electrochemical microscopy. *J Electroanal Chem* **483**, 7-17 (2000).

(57) Peinetti, A. S., Gilardoni, R. S., Mizrahi, M., Requejo, F. G., Gonzalez, G. A. & Battaglini, F. Numerical simulation of the diffusion processes in nanoelectrode arrays using an axial neighbor symmetry approximation. *Anal Chem* **88**, 5752-5759 (2016).

(58) Zoski, C. G. & Wijesinghe, M. Electrochemistry at ultramicroelectrode arrays and nanoelectrode ensembles of macro- and ultramicroelectrode dimensions. *Isr J Chem* **50**, 347-359 (2010).

(59) Dobson, P. S., Weaver, J. M. R., Burt, D. P., Holder, M. N., Wilson, N. R., Unwin P. R. & Macpherson, J. V. Electron beam lithographically-defined scanning electrochemical-atomic force microscopy probes: fabrication method and application to high resolution imaging on heterogeneously active surfaces. *Phys Chem Chem Phys* **8**, 3909-3914 (2006).

(60) Roberts, N. A., Noh, J. H., Lassiter, M. G., Guo, S., Kalinin, S. V. & Rack, P. R. Synthesis and electroplating of high resolution insulated carbon nanotube scanning probes for imaging in liquid solutions. *Nanotechnology* **23** (2012).

(61) Noh, J. H., Nikiforov, M., Kalinin, S. V., Vertegel, A. A. & Rack, P. D. Nanofabrication of insulated scanning probes for electromechanical imaging in liquid solutions. *Nanotechnology* **21** 365302 (2010).

(62) Rodriguez, B. J., Jesse, S., Seal, K., Baddorf, A. P., Kalinin, S. V. and Rack, P. D. Fabrication, dynamics, and electrical properties of insulated scanning probe microscopy probes for electrical and electromechanical imaging in liquids. *Appl Phys Lett* **91**, 093130 (2007).

(63) Pobelov, I. V., Mohos, M., Yoshida, K., Kolivoska, V., Avdic, A., Lugstein, A., Bertagnolli, E., Leonhardt, K., Denuault, G., Gollas, B. & Wandlowski, T. Electrochemical current-sensing atomic force microscopy in conductive solutions. *Nanotechnology* **24**, 115501 (2013).

(64) Ventosa, E. & Schuhmann, W. Scanning electrochemical microscopy of Li-ion batteries. *Phys Chem Chem Phys* **17**, 28441-28450 (2015).

(65) Insun Yoon, Daniel P. Abraham, Brett L. Lucht, Allan F. Bower & Guduru, P. R. In situ measurement of solid electrolyte interphase evolution on silicon anodes using atomic force microscopy. *Adv Energy Mater* **6**, 1600099 (2016).

(66) Hu, X. Y., Chen, C. L., Yan, J. W. & Mao, B. W. Electrochemical and in-situ scanning tunneling microscopy studies of bis(fluorosulfonyl)imide and bis(trifluoromethanesulfonyl)imide based ionic liquids on graphite and gold electrodes and lithium salt influence. *J Power Sources* **293**, 187-195 (2015).

(67) Hui, J. S., Burgess, M., Zhang, J. R. & Rodriguez-Lopez, J. Layer number dependence of Li^+ intercalation on few-layer graphene and electrochemical imaging of its solid-electrolyte interphase evolution. *ACS Nano* **10**, 4248-4257 (2016).

(68) Goncalves, L. M., Batchelor-McAuley, C., Barros, A. A. & Compton, R. G. Electrochemical oxidation of adenine: A mixed adsorption and diffusion response on an edge-plane pyrolytic graphite electrode. *J Phys Chem C* **114**, 14213-14219 (2010).

(69) Davies, T. J., Hyde, M. E. & Compton, R. G. Nanotrench arrays reveal insight into graphite electrochemistry. *Angew Chem Int Edit* **44**, 5121-5126 (2005).

(70) Lai, S. C. S., Macpherson, J. V. & Unwin, P. R. In situ scanning electrochemical probe microscopy for energy applications. *MRS Bull* **37**, 668-674 (2012).

(71) Patel, A. N., Collignon, M. G., O'Connell, M. A., Huang, W. O. Y., McKelvey, K., Macpherson, J. V. & Unwin, P. R. A new view of electrochemistry at highly oriented pyrolytic graphite. *J Am Chem Soc* **134**, 20117-20130 (2012).

(72) Zhang, G., Kirkman, P. M., Patel, A. N., Cuharuc, A. S., McKelvey, K. & Unwin, P. R.. Molecular functionalization of graphite surfaces: basal plane versus step edge electrochemical activity. *J Am Chem Soc* **136**, 11444-11451 (2014).

(73) Patel, A. N., Tan, S. Y. & Unwin, P. R. Epinephrine electro-oxidation highlights fast electrochemistry at the graphite basal surface. *Chem Commun* **49**, 8776-8778 (2013).

(74) Patel, A. N., McKelvey, K. & Unwin, P. R. Nanoscale electrochemical patterning reveals the active sites for catechol oxidation at graphite surfaces. *J Am Chem Soc* **134**, 20246-20249 (2012).

(75) Anne, A., Cambril, E., Chovin, A., Demaille, C. & Goyer, C. Electrochemical atomic force microscopy using a tip-attached redox mediator for topographic and functional imaging of nanosystems. *Acs Nano* **3**, 2927-2940, (2009).

(76) Frederix, P. L. T. M., Bosshart, P. D., Akiyama, T., Chami, M., Gullo, M. R., Blackstock, J. J., Dooleweerdt, K., de Rooij, N. F., Staufer, U. & Engel, A. Conductive supports for combined AFM-SECM on biological membranes. *Nanotechnology* **19**, 384004 (2008).

(77) Williams, C. G., Edwards, M. A., Colley, A. L., Macpherson, J. V. & Unwin, P. R. Scanning micropipet contact method for high-resolution imaging of electrode surface redox activity. *Anal Chem* **81**, 2486-2495 (2009).

(78) Patel, A. N., Tan, S. Y., Miller, T. S., Macpherson, J. V. & Unwin, P. R. Comparison and reappraisal of carbon electrodes for the voltammetric detection of dopamine. *Anal Chem* **85**, 11755-11764 (2013).

(79) Edwards, M. A., Bertoncello, P. & Unwin, P. R. Slow diffusion reveals the intrinsic electrochemical activity of basal plane highly oriented pyrolytic graphite electrodes. *J Phys Chem C* **113**, 9218-9223 (2009).

(80) Guell, A. G., Cuhard, A. S., Kim, Y.-R., Zhang, G., Tan, S.-Y., Ebejer, N. & Unwin, P. R.. Redox-dependent spatially resolved electrochemistry at graphene and graphite step edges. *ACS Nano* **9**, 3558-3571 (2015).

(81) Lai, S. C. S., Patel, A. N., McKelvey, K. & Unwin, P. R. Definitive evidence for fast electron transfer at pristine basal plane graphite from high-resolution electrochemical imaging. *Angew Chem Int Edit* **51**, 5405-5408 (2012).

(82) Banerjee, S., Sardar, M., Gayathri, N., Tyagi, A. K. & Raj, B. Conductivity landscape of highly oriented pyrolytic graphite surfaces containing ribbons and edges. *Phys Rev B* **72**, 075418 (2005).

(83) Stein, S. E. & Brown, R. L. Pi-electron properties of large condensed polyaromatic hydrocarbons. *J Am Chem Soc* **109**, 3721-3729 (1987).

CHAPTER IV

(1) Walter, M. G. *et al.* Solar water splitting cells. *Chem. Rev.* **110,** 6446–6473 (2010).

(2) Sivula, K. & Van de Krol, R. Semiconducting materials for photoelectrochemical energy conversion. *Nat. Rev. Mater.* **1,** 15015 (2016).

(3) Zandi, O. & Hamann, T. W. The potential versus current state of water splitting with hematite. *Phys. Chem. Chem. Phys.* **17,** 22485–22503 (2015).

(4) Sivula, K. Metal oxide photoelectrodes for solar fuel production, surface traps, and catalysis. *J. Phys. Chem. Lett.* **4,** 1624–1633 (2013).

(5) Cowan, A. J. & Durrant, J. R. Long-lived charge separated states in nanostructured semiconductor photoelectrodes for the production of solar fuels. *Chem Soc Rev* **42,** 2281–2293 (2013).

(6) Montoya, J. H. *et al.* Materials for solar fuels and chemicals. *Nat. Mater.* **16,** 70–81 (2017).

(7) Barroso, M. *et al.* Dynamics of photogenerated holes in surface modified α-Fe_2O_3 photoanodes for solar water splitting. *Proc. Natl. Acad. Sci. U. S. A.* **109,** 15640–15645 (2012).

(8) Barroso, M. *et al.* The role of cobalt phosphate in enhancing the photocatalytic activity of α-Fe_2O_3 toward water oxidation. *J. Am. Chem. Soc.* **133,** 14868–14871 (2011).

(9) Klahr, B. M., Gimenez, S., Fabregat-Santiago, F., Bisquert, J. & Hamann, T. W. Photoelectrochemical and impedance spectroscopic investigation of water oxidation with 'Co-Pi'-coated hematite electrodes. *J. Am. Chem. Soc.* **134,** 16693–16700 (2012).

(10) Carroll, G. M., Zhong, D. K. & Gamelin, D. R. Mechanistic insights into solar water oxidation by cobalt-phosphate-modified α-Fe_2O_3 photoanodes. *Energy Environ. Sci.* **8,** 577–584 (2015).

(11) Carroll, G. M. & Gamelin, D. R. Kinetic analysis of photoelectrochemical water oxidation by mesostructured Co-Pi/α-Fe_2O_3 photoanodes. *J. Mater. Chem. A* **4,** 2986–2994 (2016).

(12) Lin, F. & Boettcher, S. W. Adaptive semiconductor/electrocatalyst junctions in water-splitting photoanodes. *Nat. Mater.* **13,** 81–86 (2014).

(13) Nellist, M. R., Laskowski, F. A. L., Lin, F., Mills, T. J. & Boettcher, S. W. Semiconductor-electrocatalyst interfaces: theory, experiment, and applications in photoelectrochemical water splitting. *Acc. Chem. Res.* **49,** 733–740 (2016).

(14) Lin, F., Bachman, B. F. & Boettcher, S. W. Impact of electrocatalyst activity and ion permeability on water-splitting photoanodes. *J. Phys. Chem. Lett.* **6,** 2427–2433 (2015).

(15) Mills, T. J., Lin, F. & Boettcher, S. W. Theory and simulations of electrocatalyst-coated semiconductor electrodes for solar water splitting. *Phys. Rev. Lett.* **112,** 148304 (2014).

(16) Laskowski, F. A. L., Nellist, M. R., Venkatkarthick, R. & Boettcher, S. W. Junction behavior of n-Si photoanodes protected by thin Ni elucidated from dual

working electrode photoelectrochemistry. *Energy Environ. Sci.* **10,** 570–579 (2017).

(17) Qiu, J. *et al.* Direct in situ measurement of charge transfer processes during photoelectrochemical water oxidation on catalyzed hematite. *ACS Cent. Sci.* **3,** 1015–1025 (2017).

(18) Hurth, C., Li, C. & Bard, A. J. Direct probing of electrical double layers by scanning electrochemical potential microscopy. *J. Phys. Chem. C* **111,** 4620–4627 (2007).

(19) Yoon, Y. *et al.* A nanometer potential probe for the measurement of electrochemical potential of solution. *Electrochim. Acta* **52,** 4614–4621 (2007).

(20) Yoon, Y., Woo, D., Shin, T., Chung, T. D. & Kang, H. Real-space investigation of electrical double layers. Potential gradient measurement with a nanometer potential probe. *J. Phys. Chem. C* **115,** 17384–17391 (2011).

(21) Woo, D., Yoo, J., Park, S., Jeon, I. C. & Kang, H. Direct probing into the electrochemical interface using a novel potential probe: Au(111) electrode/$NaBF_4$ solution interface. *Bull. Korean Chem. Soc.* **25,** 577–580 (2004).

(22) Baier, C. & Stimming, U. Imaging single enzyme molecules under in situ conditions. *Angew. Chemie - Int. Ed.* **48,** 5542–5544 (2009).

(23) Hamou, R. F., Biedermann, P. U., Erbe, A. & Rohwerder, M. Numerical analysis of Debye screening effect in electrode surface potential mapping by scanning electrochemical potential microscopy. *Electrochem. Commun.* **12,** 1391–1394 (2010).

(24) Traunsteiner, C., Tu, K. & Kunze-Liebhauser, J. High-resolution imaging of the initial stages of oxidation of Cu(111) with scanning electrochemical potential microscopy. *ChemElectroChem* **2,** 77–84 (2015).

(25) Domanski, A. L. *et al.* Kelvin probe force microscopy in nonpolar liquids. *Langmuir* **28,** 13892–13899 (2012).

(26) Collins, L. *et al.* Probing charge screening dynamics and electrochemical processes at the solid-liquid interface with electrochemical force microscopy. *Nat. Commun.* **5,** 3871 (2014).

(27) Collins, L. *et al.* Kelvin probe force microscopy in liquid using electrochemical force microscopy. *Beilstein J. Nanotechnol.* **6,** 201–214 (2015).

(28) Kobayashi, N., Asakawa, H. & Fukuma, T. Nanoscale potential measurements in liquid by frequency modulation atomic force microscopy. *Rev. Sci. Instrum.* **81,** 123705 (2010).

(29) Kobayashi, N., Asakawa, H. & Fukuma, T. Dual frequency open-loop electric potential microscopy for local potential measurements in electrolyte solution with high ionic strength. *Rev. Sci. Instrum.* **83,** 33709 (2012).

(30) Huang, Z. *et al.* PeakForce scanning electrochemical microscopy with nanoelectrode probes. *Microsc. Today* **24,** 18–25 (2016).

(31) Nellist, M. R. *et al.* Atomic force microscopy with nanoelectrode tips for high resolution electrochemical, nanoadhesion and nanoelectrical imaging. *Nanotechnology* **28,** 95711 (2017).

(32) Kanan, M. W. & Nocera, D. G. In situ formation of an oxygen-evolving catalyst in neutral water containing phosphate and Co^{2+}. *Science* **321,** 1072–1075 (2008).

(33) Lutterman, D. A., Surendranath, Y. & Nocera, D. G. A self-healing oxygen-evolving catalyst. *J. Am. Chem. Soc.* **131,** 3838–3839 (2009).

(34) Costentin, C., Porter, T. R. & Savéant, J.-M. Conduction and reactivity in heterogeneous-molecular catalysis: new insights in water oxidation catalysis by phosphate cobalt oxide films. *J. Am. Chem. Soc.* **138,** 5615–5622 (2016).

(35) Andrieux, C. P., Costentin, C., Giovanni, C. Di, Savéant, J.-M. & Tard, C. Conductive mesoporous catalytic films. Current distortion and performance degradation by dual-phase ohmic drop effects. Analysis and remedies. *J. Phys. Chem. C* **120,** 21263–21271 (2016).

(36) Burke, M. S., Kast, M. G., Trotochaud, L., Smith, A. M. & Boettcher, S. W. Cobalt-iron (oxy)hydroxide oxygen evolution electrocatalysts: the role of structure and composition on activity, stability, and mechanism. *J. Am. Chem. Soc.* **137,** 3638–3648 (2015).

(37) Burke, M. S. *et al.* Revised oxygen evolution reaction activity trends for first-row transition-metal (oxy)hydroxides in alkaline media. *J. Phys. Chem. Lett.* **6,** 3737–3742 (2015).

(38) Klingan, K. *et al.* Water oxidation by amorphous cobalt-based oxides: volume activity and proton transfer to electrolyte bases. *Chem Sus Chem* **7,** 1301–1310 (2014).

(39) Jörissen, L. Bifunctional oxygen/air electrodes. *J. Power Sources* **155,** 23–32 (2006).

(40) Doyle, R. L. & Lyons, M. E. G. An electrochemical impedance study of the oxygen evolution reaction at hydrous iron oxide in base. *Phys. Chem. Chem. Phys.* **15,** 5224–5237 (2013).

(41) Batchellor, A. S. & Boettcher, S. W. Pulse-electrodeposited Ni-Fe (oxy)hydroxide oxygen evolution electrocatalysts with high geometric and intrinsic activities at large mass loadings. *ACS Catal.* **5,** 6680–6689 (2015).

(42) Klahr, B. M., Martinson, A. B. F. & Hamann, T. W. Photoelectrochemical investigation of ultrathin film iron oxide solar cells prepared by atomic layer deposition. *Langmuir* **27,** 461–468 (2011).

(43) Tilley, S. D., Cornuz, M., Sivula, K. & Grätzel, M. Light-induced water splitting

with hematite: improved nanostructure and iridium oxide catalysis. *Angew. Chemie - Int. Ed.* **49,** 6405–6408 (2010).

(44) Kay, A., Cesar, I. & Grätzel, M. New benchmark for water photooxidation by nanostructured α-Fe_2O_3 films. *J. Am. Chem. Soc.* **128,** 15714–15721 (2006).

(45) Ma, Y., Kafizas, A., Pendlebury, S. R., Le Formal, F. & Durrant, J. R. Photoinduced absorption spectroscopy of CoPi on $BiVO_4$: the function of CoPi during water oxidation. *Adv. Funct. Mater.* **26,** 4951–4960 (2016).

(46) Ma, Y., Le Formal, F., Kafizas, A., Pendlebury, S. R. & Durrant, J. R. Efficient suppression of back electron/hole recombination in cobalt phosphate surface-modified undoped bismuth vanadate photoanodes. *J. Mater. Chem. A* **3,** 20649–20657 (2015).

(47) Kennedy, J. H. & Frese, K. W. Photooxidation of water at α-Fe_2O_3 electrodes. *J. Electrochem. Soc.* **125,** 709–714 (1978).

(48) Zandi, O., Schon, A. R., Hajibabaei, H. & Hamann, T. W. Enhanced charge separation and collection in high-performance electrodeposited hematite films. *Chem. Mater.* **28,** 765–771 (2016).

(49) Honbo, K. *et al.* Visualizing nanoscale distribution of corrosion cells by open-loop electric potential microscopy. *ACS Nano* **10,** 2575–2583 (2016).

(50) Klahr, B. M., Gimenez, S., Fabregat-Santiago, F., Hamann, T. W. & Bisquert, J. Water oxidation at hematite photoelectrodes: the role of surface states. *J. Am. Chem. Soc.* **134,** 4294–4302 (2012).

(51) Zandi, O. & Hamann, T. W. Enhanced water splitting efficiency through selective surface state removal. *J. Phys. Chem. Lett.* **5,** 1522–1526 (2014).

(52) Dezelah, C. L., Niinistö, J., Arstila, K., Niinistö, L. & Winter, C. H. Atomic layer deposition of Ga_2O_3 films from a dialkylamido-based precursor. *Chem. Mater.* **18,** 471–475 (2006).

(53) Surendranath, Y., Kanan, M. W. & Nocera, D. G. Mechanistic studies of the oxygen evolution reaction by a cobalt-phosphate catalyst at neutral pH. *J. Am. Chem. Soc.* **132,** 16501–16509 (2010).

(54) Risch, M. *et al.* Cobalt-oxo core of a water-oxidizing catalyst film. *J. Am. Chem. Soc.* **131,** 6936–6937 (2009).

(55) Kanan, M. W. *et al.* Structure and valency of a cobalt-phosphate water oxidation catalyst determined by in situ X-ray spectroscopy. *J. Am. Chem. Soc.* **132,** 13692–13701 (2010).

(56) Surendranath, Y., Dinca, M. & Nocera, D. G. Electrolyte-dependent electrosynthesis and activity of cobalt-based water oxidation catalysts. *J. Am. Chem. Soc.* **131,** 2615–2620 (2009).

CHAPTER V

(1) Park, Y.; McDonald, K. J.; Choi, K.-S. Progress in Bismuth Vanadate Photoanodes for Use in Solar Water Oxidation. *Chem. Soc. Rev.* **2013**, *42* (6), 2321–2337.

(2) Lamm, B.; Trześniewski, B. J.; Döscher, H.; Smith, W. A.; Stefik, M. Emerging Post-Synthetic Improvements of BiVO 4 Photoanodes for Solar Water Splitting. *ACS Energy Lett.* **2017**, *3* (1), 112–124.

(3) Abdi, F. F.; van de Krol, R. Nature and Light Dependence of Bulk Recombination in Co-Pi- Catalyzed $BiVO_4$ Photoanodes. *J. Phys. Chem. C* **2012**, *116*, 9398–9404.

(4) Shinde, A.; Guevarra, D.; Liu, G.; Sharp, I. D.; Toma, F. M.; Gregoire, J. M.; Haber, J. A. Discovery of Fe-Ce Oxide/BiVO4Photoanodes through Combinatorial Exploration of Ni-Fe-Co-Ce Oxide Coatings. *ACS Appl. Mater. Interfaces* **2016**, *8* (36), 23696–23705.

(5) Zhong, D. K.; Choi, S.; Gamelin, D. R. Near-Complete Suppression of Surface Recombination in Solar Photoelectrolysis by " Co-Pi " Catalyst-Modified W:$BiVO_4$. *J. Am. Chem. Soc.* **2011**, *133*, 18370–18377.

(6) Pilli, S. K.; Furtak, T. E.; Brown, L. D.; Deutsch, T. G.; Turner, J. A.; Herring, A. M. Cobalt-Phosphate (Co-Pi) Catalyst Modified Mo-Doped $BiVO_4$ Photoelectrodes for Solar Water Oxidation. *Energy Environ. Sci.* **2011**, *4* (12), 5028.

(7) Jeong, H. W.; Jeon, T. H.; Jang, J. S.; Choi, W.; Park, H. Strategic Modification of $BiVO_4$ for Improving Photoelectrochemical Water Oxidation Performance. *J. Phys. Chem. C* **2013**, *117* (18), 9104–9112.

(8) Abdi, F. F.; Han, L.; Smets, A. H. M.; Zeman, M.; Dam, B.; van de Krol, R. Efficient Solar Water Splitting by Enhanced Charge Separation in a Bismuth Vanadate-Silicon Tandem Photoelectrode. *Nat. Commun.* **2013**, *4*, 1–7.

(9) Abdi, F. F.; Firet, N.; Van de Krol, R. Efficient $BiVO_4$ Thin Film Photoanodes Modified with Cobalt Phosphate Catalyst and W-Doping. *ChemCatChem* **2013**, *5* (2), 490–496.

(10) Choi, S. K.; Choi, W.; Park, H. Solar Water Oxidation Using Nickel-Borate Coupled $BiVO_4$ Photoelectrodes. *Phys. Chem. Chem. Phys.* **2013**, *15* (17), 6499.

(11) McDowell, M. T.; Lichterman, M. F.; Spurgeon, J. M.; Hu, S.; Sharp, I. D.; Brunschwig, B. S.; Lewis, N. S. Improved Stability of Polycrystalline Bismuth Vanadate Photoanodes by Use of Dual-Layer Thin TiO_2/Ni Coatings. *J. Phys. Chem. C* **2014**, *118* (34), 19618–19624.

(12) Seabold, J. A.; Choi, K.-S. Efficient and Stable Photo-Oxidation of Water by a Bismuth Vanadate Photoanode Coupled with an Iron Oxyhydroxide Oxygen

Evolution Catalyst. *J. Am. Chem. Soc.* **2012**, *134* (4), 2186–2192.

(13) Park, Y.; Kang, D.; Choi, K.-S. Marked Enhancement in Electron–hole Separation Achieved in the Low Bias Region Using Electrochemically Prepared Mo-Doped $BiVO_4$ Photoanodes. *Phys. Chem. Chem. Phys.* **2014**, *16* (3), 1238–1246.

(14) Kuang, Y.; Jia, Q.; Nishiyama, H.; Yamada, T.; Kudo, A.; Domen, K. A Front-Illuminated Nanostructured Transparent BiVO4 Photoanode for >2% Efficient Water Splitting. *Adv. Energy Mater.* **2016**, *6* (2), 1510645.

(15) Kim, T. W.; Choi, K.-S. Nanoporous BiVO4 Photoanodes with Dual-Layer Oxygen Evolution Catalysts for Solar Water Splitting. *Science.* **2014**, *343* (6174), 990–994.

(16) Barroso, M.; Mesa, C. a; Pendlebury, S. R.; Cowan, A. J.; Hisatomi, T.; Sivula, K.; Grätzel, M.; Durrant, J. R. Dynamics of Photogenerated Holes in Surface Modified α-Fe_2O_3 Photoanodes for Solar Water Splitting. *Proc. Natl. Acad. Sci. U. S. A.* **2012**, *109*, 15640–15645.

(17) Ma, Y.; Kafizas, A.; Pendlebury, S. R.; Le Formal, F.; Durrant, J. R. Photoinduced Absorption Spectroscopy of CoPi on $BiVO_4$: The Function of CoPi during Water Oxidation. *Adv. Funct. Mater.* **2016**, *26* (27), 4951–4960.

(18) Zachäus, C.; Abdi, F. F.; Peter, L. M.; van de Krol, R. Photocurrent of $BiVO_4$ Is Limited by Surface Recombination, Not Surface Catalysis. *Chem. Sci.* **2017**, *8*, 3712–3719.

(19) Xi, L.; Wang, F.; Schwanke, C.; Abdi, F. F.; Golnak, R.; Fiechter, S.; Ellmer, K.; van de Krol, R.; Lange, K. M. In Situ Structural Study of MnPi Modified BiVO 4 Photoanodes by Soft X-Ray Absorption Spectroscopy. *J. Phys. Chem. C* **2017**, *121*, 19668–19676.

(20) Nellist, M. R.; Chen, Y.; Mark, A.; Gödrich, S.; Stelling, C.; Jiang, J.; Poddar, R.; Li, C.; Kumar, R.; Papastavrou, G.; et al. Atomic Force Microscopy with Nanoelectrode Tips for High Resolution Electrochemical, Nanoadhesion and Nanoelectrical Imaging. *Nanotechnology* **2017**, *28*, 095711.

(21) Huang, Z.; Wolf, P. De; Poddar, R.; Li, C.; Mark, A.; Nellist, M. R.; Chen, Y.; Jiang, J.; Papastavrou, G.; Boettcher, S. W.; et al. PeakForce Scanning Electrochemical Microscopy with Nanoelectrode Probes. *Microsc. Today* **2016**, *24*, 18–25.

(22) Nellist, M. R.; Laskowski, F. A. L.; Qiu, J.; Hajibabaei, H.; Sivula, K.; Hamann, T. W.; Boettcher, S. W. Potential-Sensing Electrochemical Atomic Force Microscopy for in Operando Analysis of Water-Splitting Catalysts and Interfaces. *Nat. Energy* **2018**, No. 3, 46–52.

(23) Toma, F. M.; Cooper, J. K.; Kunzelmann, V.; McDowell, M. T.; Yu, J.; Larson, D.

M.; Borys, N. J.; Abelyan, C.; Beeman, J. W.; Yu, K. M.; et al. Mechanistic Insights into Chemical and Photochemical Transformations of Bismuth Vanadate Photoanodes. *Nat. Commun.* **2016**, *7* (May), 12012.

(24) Qiu, J.; Hajibabaei, H.; Nellist, M. R.; Laskowski, F. A. L.; Oener, S. Z.; Hamann, T. W.; Boettcher, S. W. Catalyst Deposition on Photoanodes: The Roles of Intrinsic Catalytic Activity, Catalyst Electrical Conductivity, and Semiconductor Morphology. *ACS Energy Lett.* **2018**, *3* (4), 961–969.

(25) Burke, M. S.; Zou, S.; Enman, L. J.; Kellon, J. E.; Gabor, C. A.; Pledger, E.; Boettcher, S. W. Revised Oxygen Evolution Reaction Activity Trends for First-Row Transition-Metal (Oxy)Hydroxides in Alkaline Media. *J. Phys. Chem. Lett.* **2015**, *6* (18), 3737–3742.

(26) Burke, M. S.; Kast, M. G.; Trotochaud, L.; Smith, A. M.; Boettcher, S. W. Cobalt-Iron (Oxy)Hydroxide Oxygen Evolution Electrocatalysts: The Role of Structure and Composition on Activity, Stability, and Mechanism. *J. Am. Chem. Soc.* **2015**, *137* (10), 3638–3648.

(27) Ma, Y.; Pendlebury, S. R.; Reynal, A.; Le Formal, F.; Durrant, J. R. Dynamics of Photogenerated Holes in Undoped $BiVO_4$ Photoanodes for Solar Water Oxidation. *Chem. Sci.* **2014**, *5* (8), 2964–2973.

(28) Eisenberg, D.; Ahn, H. S.; Bard, A. J. Enhanced Photoelectrochemical Water Oxidation on Bismuth Vanadate by Electrodeposition of Amorphous Titanium Dioxide. *J. Am. Chem. Soc.* **2014**, *136* (40), 14011–14014.

(29) Byun, S.; Kim, B.; Jeon, S.; Shin, B. Effects of a SnO2hole Blocking Layer in a BiVO4-Based Photoanode on Photoelectrocatalytic Water Oxidation. *J. Mater. Chem. A* **2017**, *5* (15), 6905–6913.

(30) Liang, Y.; Tsubota, T.; Mooij, L. P. A.; van de Krol, R. Highly Improved Quantum Efficiencies for Thin Film $BiVO_4$ Photoanodes. *J. Phys. Chem. C* **2011**, *115* (35), 17594–17598.

(31) Nellist, M. R.; Laskowski, F. A. L.; Lin, F.; Mills, T. J.; Boettcher, S. W. Semiconductor-Electrocatalyst Interfaces: Theory, Experiment, and Applications in Photoelectrochemical Water Splitting. *Acc. Chem. Res.* **2016**, *49*, 733–740.

(32) Laskowski, F. A. L.; Nellist, M. R.; Venkatkarthick, R.; Boettcher, S. W. Junction Behavior of N-Si Photoanodes Protected by Thin Ni Elucidated from Dual Working Electrode Photoelectrochemistry. *Energy Environ. Sci.* **2017**, *10* (2), 570–579.

(33) Lin, F.; Boettcher, S. W. Adaptive Semiconductor/Electrocatalyst Junctions in Water-Splitting Photoanodes. *Nat. Mater.* **2014**, *13*, 81–86.

(34) Qiu, J.; Hajibabaei, H.; Nellist, M. R.; Laskowski, F. A. L.; Hamann, T. W.;

Boettcher, S. W. Direct in Situ Measurement of Charge Transfer Processes during Photoelectrochemical Water Oxidation on Catalyzed Hematite. *ACS Cent. Sci.* **2017**, *3*, 1015–1025.

APPENDIX A

(1) Narita, E., Lawson, F. & Han, K.N., Solubility of oxygen in aqueous electrolyte solutions. *Hydrometallurgy*, **1983**, *10*, 21.

(2) Han, P. & Bartels, D. M., Temperature dependence of oxygen diffusion in H_2O and D_2O. *J. Phys. Chem.* **1996**, *100*, 5597.

(3) Wang, Y., Limon-Petersen, J. G., & Compton, R. G. Measurement of the diffusion coefficients of $[Ru(NH_3)_6]^{3+}$ and $[Ru(NH_3)_6]^{2+}$ in aqueous solution using microelectrode double potential step chronoamperometry. *J. Electroanal. Chem.* **2011**, *652*, 13.

(4) Bard A. J., Fan, F. –R. F. & Mirkin, M. V. Scanning electrochemical microscopy. In "The Handbook of Surface Imaging and Visualization", Hubbard A. T. ed. 1995, CRC Press.

APPENDIX B

(1) Burke, M. S., Kast, M. G., Trotochaud, L., Smith, A. M. & Boettcher, S. W. Cobalt-iron (oxy)hydroxide oxygen evolution electrocatalysts: the role of structure and composition on activity, stability, and mechanism. *J. Am. Chem. Soc.* **137,** 3638–3648 (2015).

APPENDIX C

(1) Toma, F. M.; Cooper, J. K.; Kunzelmann, V.; McDowell, M. T.; Yu, J.; Larson, D. M.; Borys, N. J.; Abelyan, C.; Beeman, J. W.; Yu, K. M.; et al. Mechanistic Insights into Chemical and Photochemical Transformations of Bismuth Vanadate Photoanodes. *Nat. Commun.* **2016**, *7* (May), 12012.

(2) Ma, Y.; Pendlebury, S. R.; Reynal, A.; Le Formal, F.; Durrant, J. R. Dynamics of Photogenerated Holes in Undoped $BiVO_4$ Photoanodes for Solar Water Oxidation. *Chem. Sci.* **2014**, *5* (8), 2964–2973.

(3) Nellist, M. R.; Laskowski, F. A. L.; Qiu, J.; Hajibabaei, H.; Sivula, K.; Hamann, T. W.; Boettcher, S. W. Potential-Sensing Electrochemical Atomic Force Microscopy for in Operando Analysis of Water-Splitting Catalysts and Interfaces. *Nat. Energy* **2018**, No. 3, 46–52.

(4) Qiu, J.; Hajibabaei, H.; Nellist, M. R.; Laskowski, F. A. L.; Hamann, T. W.;

Boettcher, S. W. Direct in Situ Measurement of Charge Transfer Processes during Photoelectrochemical Water Oxidation on Catalyzed Hematite. *ACS Cent. Sci.* **2017**, *3*, 1015–1025.

(5) Qiu, J.; Hajibabaei, H.; Nellist, M. R.; Laskowski, F. A. L.; Oener, S. Z.; Hamann, T. W.; Boettcher, S. W. Catalyst Deposition on Photoanodes: The Roles of Intrinsic Catalytic Activity, Catalyst Electrical Conductivity, and Semiconductor Morphology. *ACS Energy Lett.* **2018**, *3* (4), 961–969.